Thermal Fatigue of Austenitic and Duplex Stainless Steels

IIKKA VIRKKUNEN

Helsinki University of Technology
Department of Mechanical Engineering
Puumiehenkuja 3 A
P.O.Box 4200
FIN-02015 HUT
Finland

Dissertation for the degree of Doctor of Science in Technology to be presented with due permission for public examination and debate in Council room at Helsinki University of Technology (Espoo, Finland) on the 23rd of November, 2001, at 12 o'clock noon.

Espoo 2001

Virkkunen, Iikka. **Thermal fatigue of austenitic and duplex stainless steels**. Acta Polytechnica Scandinavica, Mechanical Engineering Series No. 154, Espoo 2001, 115 pp. Published by the Finnish Academies of Technology

Keywords: thermal fatigue, austenitic stainless steel, duplex stainless steel, residual stress, Barkhausen noise, fatigue crack growth

ABSTRACT

Thermal fatigue behavior of AISI 304L, AISI 316, AISI 321, and AISI 347 austenitic stainless steels as well as 3RE60 and ACX-100 duplex stainless steels was studied. Test samples were subjected to cyclic thermal transients in the temperature range 20 – 600°C. The resulting thermal strains were analyzed with measurements and numerical calculations. The evolution of thermal fatigue damage was monitored with periodic residual stress measurements and replica-assisted microscopy. The elastic strains of the ferrite phase in duplex stainless steels were studied using Barkhausen noise. Finally, destructive analyses including fractographic scanning electron microscopy (SEM) studies and transmission electron microscopy (TEM) analyses were performed.

The surface residual stresses changed markedly during the first load cycles. In the austenitic stainless steels yielding during the rapid cooling resulted in compressive residual stresses from -200 MPa (20 – 300°C temperature cycle) to -600 MPa (20 – 600°C temperature cycle). After 10 cycles the residual stresses stabilized and then started to relax due to crack formation. Cracks were seen to initiate from persistent slip bands (PSBs) and in 3RE60 from MnS inclusions. In duplex stainless steels the phase boundaries retarded crack growth markedly.

In the austenitic stainless steels, the fracture surfaces of thermal fatigue cracks showed extensive striation formation, i.e. they were similar to mechanical fatigue. The dislocation density was lower than expected based on mechanical fatigue data. Dislocation tangles and occasional cell tendency was observed. In duplex stainless steels the plastic deformation concentrated to the austenite phase.

The obtained thermal fatigue data were compared with mechanical fatigue data from literature and with the ASME design curve. The ASME design curve was found to give safe design life, although the remaining safety factor on strain is decreased to 1.5. The total strain (elastic+plastic) caused by thermal loading was solved with linear-elastic FE-analysis. Thermal fatigue crack growth was predicted successively using total strain solution of an uncracked component and a strain-based growth model:

$$\frac{da}{dN} = C_7 \Delta \varepsilon_{tot}^{m_7} a,$$

where C_7=1.6 and
m_7=1.3 for the studied austenitic stainless steels.

The model is applicable to small fatigue cracks (0.05 - 4 mm) growing in varying temperature and strain fields and is temperature-independent in the studied range.

PREFACE

The research work presented in this thesis was mainly accomplished as a part of the research project "Thermal Fatigue Mechanisms" financed by TEKES, Fortum Nuclear Services Ltd., Fortum Oil & Gas Oy, Metso Paper Oy, Outokumpu Poricopper Oy, and Teollisuuden Voima Oy. The steering committee of the project also gave valuable comments and suggestions during my work. The support is gratefully acknowledged. The financial support of Imatran Voiman Säätiö and KAUTE (Laura & Aarne Karjalainen fund) is also acknowledged.

I am deeply grateful to professor Hannu Hänninen for the advice and unlimited expertise he provided for my guidance. Numerous co-workers and friends also offered their help and support. I wish to express my gratitude to Mika Kemppainen for the fruitful collaboration, for Sergiy Smuk, Jaakko Virkkunen, and Ville Virkkunen for their encouragement and perceptive comments on my thesis, to Wade Karlsen for advice on the grammar of the thesis, to Laura Taivalaho for TEM work and help with the grammar of the thesis, to Pertti Nenonen for the exquisite TEM work, and for the workers of the Laboratory of Engineering Materials for creating a fruitful and always enjoyable working atmosphere. I also wish to extend my gratitude to the pre-examiners of this work, Prof. Gary Marquis and Dr. Arttu Laitinen for their very valuable and constructive criticism.

Finally, I wish to express my deepest gratitude to my wife Päivi and to my newborn daughter, who made my life outside my work exceedingly rewarding.

Otaniemi, June 2001

Iikka Virkkunen

CONTENTS

ORIGINAL FEATURES

The experimental data and analyses of this thesis are directed towards modeling and predicting thermal fatigue damage and especially thermal fatigue crack growth in stainless steels. The following features are believed to be original:

1. Detailed study of the strains, residual stresses, dislocation structures and fatigue crack growth caused by cyclic thermal loading was performed.

2. An original method was developed to measure the elastic strains of the ferrite phase in a two-phase ferritic-austenitic duplex stainless steel using Barkhausen noise.

3. Linear-elastic FEM solution was found to give good approximation of the total (elastic + plastic) strains in strain-controlled, thermal load case.

4. The acquired thermal fatigue data was analyzed according to the ASME (1995) pressure vessel code. The code was found to give safe design life; the remaining safety factor on strain is 1.5.

5. It was shown that thermal fatigue crack growth in the crack depth range of 0.1 – 5 mm can be predicted using a total strain based crack growth model:

$$\frac{da}{dN} = C_7 \Delta \varepsilon_{tot}^{m_7} a,$$

where C_7=1.6 and
m_7=1.3 for the studied austenitic stainless steels.

6. It was shown that the model used is independent of test temperature in the studied range.

7. Verified range of the applicability for the crack growth model was extended from mechanical fatigue to thermal fatigue and for cracks growing in varying strain and temperature fields.

NOMENCLATURE

A	Area (m^2)
a	Crack depth
a_0	Initial crack depth
a_{eff}	Effective crack length for the El Haddad model
b	Burgers vector
C_1	Parameter for the Paris law
C_2	Parameter for the Paris equation used with K_ε
C_3	Parameter for the Tomkins model
C_4	Parameter for the Solomon model
C_5	Parameter for the Ahmad-Yates model
C_6	Parameter for the Ahmad-Yates model
C_7	Parameter for the Taira model
C_8	Parameter for the Nisitani model
D	Deformation zone size (μm)
	Plastic zone size (μm)
d	Grain size of the material (μm)
E	Young's modulus (GPa)
F_{en}	Fatigue life correction factor for environmentally assisted fatigue
G	Energy release rate
I_β	Material constant for the Skelton model
J	J integral
J_e	Elastic part of J
J_p	Plastic part of J
K	Stress intensity factor (MPa $m^{0.5}$)
K_I	Stress intensity factor for mode I loading (MPa $m^{0.5}$)
K_{ISCC}	Threshold stress intensity factor for stress corrosion cracking (MPa $m^{0.5}$)
K_ε	Strain intensity factor ($m^{0.5}$)
M	Material constant for the Paris law
m_1	Parameter for the Paris law
m_2	Parameter for the Paris equation used with K_ε
m_4	Parameter for the Solomon model
m_5	Parameter for the Ahmad-Yates model
m_6	Parameter for the Ahmad-Yates model
m_7	Parameter for equation 40
m_8	Parameter for the Taira model
N	Cycle number
O'	Parameter describing the effect of dissolved oxygen on corrosion fatigue
q	Parameter for the Haigh-Skelton model
R	Load ratio ($\varepsilon_{min}/\varepsilon_{max}$)
r	Radius (mm)
r_I	Inner radius (mm)
r_O	Outer radius (mm)

S	Striation spacing (μm)
s_1	Strain hardening exponent
s_2	Work hardening exponent
T	Temperature (°C)
T'	Temperature dependent parameter for estimating F_{en}
T_e	Equivalent temperature (°C)
T_{max}	Maximum temperature during a cycle (°C)
T_{min}	Minimum temperature during a cycle (°C)
T_t	Traction vector for the J integral
t	Parameter for the Gabetta model
u	Displacement (mm)
V_α	Volume fraction of α-phase (%)
V_γ	Volume fraction of γ-phase (%)
W	Strain energy density
w_c	Hysteresis energy per cycle
W_e	Elastic strain energy density
W_f	Energy required for failure
W_p	Plastic strain energy density
Y	Geometry factor for K and K_ε
ΔK_{th}	Threshold stress intensity factor range below which crack growth stops
$\Delta\sigma_1$	Fatigue limit
Γ	Arbitrary path surrounding the crack tip
α	Linear coefficient of thermal expansion (K^{-1})
	Ferrite phase in duplex stainless steels
β	Material constant for the Skelton model
ε	Strain (mm/mm)
$\dot{\varepsilon}$	Strain rate (s^{-1})
$\dot{\varepsilon}'$	Parameter describing the effect of strain rate on corrosion fatigue
ε_a	Axial strain (mm/mm)
ε_e	Elastic strain (mm/mm)
ε_{eb}	Elastic biaxial strain (mm/mm)
ε_{eq}	Equivalent strain for the Haigh-Skelton model (mm/mm)
ε_{eu}	Elastic uniaxial strain (mm/mm)
ε_m	Measured apparent strain (mm/mm)
ε_{max}	Maximum strain, e.g., during a cycle (mm/mm)
ε_{min}	Minimum strain, e.g., during a cycle (mm/mm)
ε_p	Plastic strain (mm/mm)
ε_{pb}	Plastic biaxial strain (mm/mm)
ε_{pu}	Plastic uniaxial strain (mm/mm)
ε_r	Radial strain (mm/mm)
ε_t	Tangential strain (mm/mm)
ε_{tot}	Total (elastic+plastic) strain (mm/mm)
ε_T	Thermal expansion (mm/mm)
ε_σ	Constrained thermal expansion (mm/mm)
γ	Austenite phase in duplex stainless steels
ν	Poisson's ratio
ν_{eff}	Effective Poisson's ratio

σ	Stress (MPa)
σ_{μ}	Microscopic (average) stress (MPa)
σ_{a}	Axial stress (MPa)
σ_{f}	Flow stress (MPa)
σ_{M}	Macroscopic stress (MPa)
σ_{max}	Maximum stress during a cycle (MPa)
σ_{phase}	Total average phase stress (MPa)
σ_{t}	Tangential stress (MPa)
σ_{y}	Yield stress (MPa)
σ_{yc}	Cyclic yield stress (MPa)
$\sigma_{\mu\alpha}$	Microscopic (average) stress in phase α (MPa)
$\sigma_{\mu\gamma}$	Microscopic (average) stress in phase γ (MPa)
σ_{r}	Radial stress (MPa)

1 INTRODUCTION – CURRENT UNDERSTANDING OF THERMAL FATIGUE

Components subjected to alternating heating and cooling have been found to crack and eventually fail. This phenomenon is termed thermal fatigue. The reason for cracking is believed to be twofold. Firstly, temperature change in the material induces thermal expansion (or contraction). If surrounding material or external constraints hinder this expansion, thermal stresses arise. These cyclic thermal stresses cause fatigue similar to that of mechanical stresses. Typical components where this kind of problems arise are, e.g., power and process industry pipings where turbulent mixing of fluids causes quick thermal transients, or rotating components in the paper industry where frictional heating causes rapid temperature cycles (e.g., Dean, 2000; Hänninen & Hakala, 1981).

Secondly, at high temperatures, materials are found to exhibit time dependent deformation, i.e. creep. Failure is generated by a process combining creep and fatigue (e.g., Taira & Fujino, 1979; Zamrik, 1990; Goswami, 1999; Gandossi, 2000). Creep becomes more significant with increasing temperature and prolonged exposure. Typical components, where creep-fatigue interaction is significant include gas turbine blades and soldered joints of electric circuitry.

The motivation for this study of thermal fatigue is to enhance the reliability of affected components. The economical effects of unexpected failures can be very high, e.g., in power, process and paper industries. Failures may threaten property and even life. The existing design methods do not give adequate tools for design against thermal fatigue. In the case of thermal fatigue, the increase of safety by using heavier constructions is not only uneconomical but also often impossible. In some cases a heavy design increases the constraint to thermal expansion and thus has a negative effect on component safety.

This study is focused on the thermal fatigue in power, process and paper industries, where time-dependent effects can be presumed to be negligible (Zauter et al., 1994). The theoretical background on which the current understanding of the phenomenon is based is that of mechanical fatigue (or just fatigue) and thermal stresses.

1.1 Thermal stresses

Change in temperature induces thermal expansion in a material:

$$\varepsilon_T = \alpha \Delta T, \tag{1}$$

where ε_T is the thermal expansion (mm/mm),
α is the linear coefficient of thermal expansion (K^{-1}) and
ΔT is the temperature change causing the expansion (K).

If this expansion is hindered, thermal stresses arise. The magnitude of the arising stresses is such that if applied as an external load they would result in strain equal to the hindered expansion. Thermal stresses can arise because of either external or internal constraints. Internal constraints can be caused by nonuniform temperature distribution or nonuniform material properties. If the thermal stresses arise due to internal constraints, the loading is called pure thermal loading, or just thermal loading. If the stresses are due to external constraints, term thermomechanical loading is used.

The elementary theory of thermal stresses is quite well established, and several textbooks have been written on the subject (e.g., Boley & Weiner, 1960). Analytical solutions to elastic and elastic-perfectly plastic thermal stress problems in various geometries have been presented in literature (e.g., Fritz & Schenectady, 1954). For example, the thermal stresses in an elastic cylinder or tube with radial temperature distribution are given by (Boley & Weiner, 1960):

$$\sigma_r(r) = \frac{\alpha E}{(1-\nu)r^2}\left[\frac{r^2 - r_I^{\,2}}{r_O^{\,2} - r_I^{\,2}} \int_{r_I}^{r_O} Tr dr - \int_{r_I}^{r} Tr dr\right] \tag{2}$$

$$\sigma_t(r) = \frac{\alpha E}{(1-\nu)r^2}\left[\frac{r^2 + r_I^{\,2}}{r_O^{\,2} - r_I^{\,2}} \int_{r_I}^{r_o} Tr dr + \int_{r_I}^{r} Tr dr - Tr^2\right], \tag{3}$$

where σ_r is the radial stress (MPa),
σ_t is the tangential stress (MPa),
α is the linear coefficient of thermal expansion (K^{-1}),
E is Young's modulus (GPa),
ν is Poisson's ratio,
T(r) is temperature (K),
r is the radius (mm),
r_I is the inner radius of the tube (mm) and
r_O is the outer radius of the tube (mm).

If the axial deformation of the cylinder is unconstrained, the axial stress is given by:

$$\sigma_a(r) = \frac{\alpha E}{(1-\nu)}\left[\frac{2}{r_O{}^2 - r_I{}^2}\int_{r_I}^{r_O} Trdr - T\right] = \sigma_r + \sigma_t, \quad (4)$$

where σ_a is the axial stress (MPa) and the other symbols are as in equations 2 and 3.

In addition to full solutions, simplified parameters for the severity of thermal transients have been proposed. Yoshimoto et al. (1999) showed that the maximum thermal stress, which develops during a quench test, can be estimated as follows:

$$\sigma_{max} = 0.705(\alpha E \Delta T) - 43.80, \quad (5)$$

where σ_{max} is the maximum thermal stress during a quench test,
E is Young's modulus (GPa),
ΔT is the temperature difference (K) and
α is the linear coefficient of thermal expansion (K^{-1}).

In a two-phase material, such as duplex stainless steel, where the two phases have different thermal expansion behavior, change in temperature gives rise to strain mismatch and thermal stresses between the two phases. The resulting microscopic thermal stresses, i.e. microstresses, can be very complex. The microstresses have to be superimposed on the macroscopic stresses to give the total phase-specific stresses.

Stevens (1999) studied the effect of thermal treatment simulating welding on the corrosion fatigue life of duplex stainless steels, and found that the applied temperature cycle reduced the corrosion fatigue life of the samples. He attributed this effect to both secondary phase precipitation and residual stresses. Behnken & Hauk (1992a; 1992b) studied the effect of microstresses on fatigue behavior, and concluded rather surprisingly that, since the residual microstresses are typically much smaller than the macroscopic residual stresses, their effect can be neglected. Other sources (Pohl & Bracke, 1997; 1999) however, concluded that thermal cycling up to 900°C causes microscopic thermal strains that result in stresses exceeding the yield strength in every cycle. Because in duplex stainless steels both constituent phases are capable of plastic deformation, pure thermal cycling can accumulate macroscopic strain to the specimens (Pohl & Bracke, 1999; Fischer et al., 1990; Siegmund et al., 1993; 1995). As temperature rises, stresses in the austenite phase are shifted towards compression, and stresses in the ferrite phase towards tension, due to the greater thermal expansion of the austenite phase. During cooling the stresses are reversed. This has been found by both X-ray residual stress measurements (Kamachi et al., 1982) and numerical simulations (Siegmund et al., 1993). The microscopic thermal stresses are highly dependent on the local microstructure, i.e. local phase morphology. In order to model the phenomenon, a set of quantitative parameters are needed to describe the investigated microstructure (Siegmund et al., 1995; Silberschmidt & Werner, 1999).

1.2 Residual stresses

In addition to external loads, thermal or mechanical residual stresses often exist in a component. These stresses result from uneven yielding during, e.g. manufacturing or thermal treatments. Residual stresses are difficult to model or measure, and they often form an unknown factor in fatigue. The residual stresses tend to fade during fatigue loading (Almer et al., 2000). Stabilized residual stresses correlate with fatigue crack initiation and fatigue life.

In a two-phase material, such as duplex stainless steels, microscopic residual stresses in the constituent phases can develop. These microstresses can result from uneven yielding of the phases during plastic deformation (e.g., Inal et al., 1999) or from uneven thermal expansion of the two phases. Irrespective of their origin, the residual stresses have strong impact on load sharing between the phases and on mechanical behavior, especially on the fatigue properties of the material. The residual stresses in a two-phase material affect the apparent thermal expansion behavior (Wang et al., 1999). The uneven yielding also causes a surface relief to develop (Polák et al., 1999).

The uneven yielding during plastic deformation gives rise to residual microstresses. The total stress in a phase is then the sum of the micro- and macrostresses:

$$\sigma_{phase} = \sigma_M + \sigma_\mu, \tag{6}$$

where σ_{phase} is the total (average) stress in a phase,
σ_M is the macroscopic stress and
σ_μ is the microscopic (average) stress in a phase.

In a randomly oriented microstructure the microscopic stresses of the constituent phases are related through the equilibrium condition:

$$V_\alpha \sigma_{\mu\alpha} + V_\gamma \sigma_{\mu\gamma} = 0, \tag{7}$$

where V_α and V_γ are the volume fractions of phases α and γ and
$\sigma_{\mu\alpha}$ and $\sigma_{\mu\gamma}$ are the (average) microstresses in phases α and γ, respectively.

Johanson & Odén (1999; 2000a; 2000b) studied the load sharing between the austenite and ferrite phase in nitrogen containing duplex stainless steels. They concluded that the hardness and the yield strength of the austenite phase are higher than those of the ferrite phase. Despite its greater strength, more plastic deformation occurs in austenite than in ferrite because of the compressive residual stress present in the ferrite phase after cooling (Johanson & Oden, 1999; 2000a; 2000b). A higher load, therefore, is transferred through the ferritic matrix. The ratio of plastic strain in austenite to that in the ferrite increases with decreasing

nitrogen content and increasing total strain amplitude (Degallaix et al., 1995).

Plastic deformation changes the residual microstresses due to uneven yielding in the constituent phases. Moverare (2001) studied the evolution of residual stresses in uniaxial tension. The experiment was repeated in several loading directions on duplex stainless steels. He concluded that the load partitioning between the two phases is dependent on the loading direction: for loading in the rolling direction, both phases deform plastically to the same degree, while more plastic deformation occurs in the austenitic phase during loading in the transverse direction. The difference in load partitioning was attributed to crystallographic texture in the ferritic phase.

1.3 Fatigue

Fatigue is defined as the degradation or failure of a material caused by cyclic loads. The study of fatigue started with the so-called phenomenological models, which ignore the mechanisms by which the fatigue failure takes place, but aim to establish a tool with which the fatigue endurance of a component can be predicted. The Wöhler and Coffin & Manson plots have been the basis for fatigue design for many decades and are still used in many design codes such as the ASME pressure vessel code (1995). During the years, several improvements have been proposed to the plots (e.g., Muralidharan & Manson, 1988; Hatanaka, 1990).

At first the material properties were assumed to remain constant during the fatigue life. Especially in low cycle fatigue, this is often not the case. Cyclic loading hardens or softens the material. The change in material properties starts from the first cycles and continues to final fracture. Consequently, the monotonic material properties do not describe the material adequately, and fatigue life predictions can be improved by considering the cyclic properties (Mughrabi, 1993, 1996; Mughrabi et al., 1997). Several corrections for the Coffin-Manson model have been proposed which take into account the cyclic properties (e.g., Kliman, 1983; Mughrabi, 1996; Shi & Pluvinage, 1994; Hatanaka, 1990). Mughrabi (1996) studied the cyclic stress-strain behavior of f.c.c and b.c.c materials. He compared the cyclic properties of these materials with several life prediction models and concluded that the microstructural interpretations of fatigue behavior are still far from being comprehensive and consistent. The cyclic stress-strain curve is affected by metallurgical factors, such as mobility of screw dislocations, strain-induced martensite and dynamic strain ageing (Hatanaka, 1990). For austenitic stainless steels several constitutive models for predicting cyclic properties have been proposed (Ohno & Kachi, 1986; McDowell, 1987).

The main drawback of the phenomenological approach is that because it lacks a direct relation to the cumulating fatigue damage, it provides inadequate tools to assess the remaining safe life of a cracked component. Also, the effect of various defects from manufacturing etc. is difficult to take into account. In addition, the cyclic stresses or strains in the component may not be uniform throughout the component, which leads to retardation or acceleration of crack growth. This cannot be adequately modeled with the phenomenological approach. Despite their inadequacies, the phenomenological models still remain in many cases the only practical design method for components with small or no initial defects. Chopra & Shack (1999) note that, although the S-N curves are conventionally used to give the number of cycles to produce gross failure for given stress or strain amplitude, they would be better interpreted as specifying the number of cycles required for the formation of an "engineering" crack for example 3 mm deep.

1.4 Dislocation structures produced by cyclic loading

Numerous studies on the dislocation structures generated by mechanical fatigue in austenitic and duplex stainless steels can be found in literature. Gerland et al. (1989; 1997) fatigued AISI 316L isothermally at different temperatures ranging from 20 to 600°C. In the beginning of fatigue at a small plastic strain amplitude ($\varepsilon_p=2x10^{-3}$), dislocation tangles and irregular cells were found. After failure, or with greater strain amplitudes, high dislocation densities and tightly arranged dislocation structures, such as walls-and-channels, cells or corduroy, were observed. Kruml et al. (1997) found ladder-like dislocation structures in AISI 316L fatigue-tested at room temperature. This structure was explained to be responsible for the strain localization. Li & Laird (1994) also found cells and walls-and-channels dislocation structures after room temperature fatigue in an AISI 316L single crystal. Orbtlík et al. (1994) (also for AISI 316L) explained that the different dislocation structures found in austenitic stainless steels are due to their intermediate stacking fault energy (SFE). Hence the dislocation structure depends on the applied strain range. For small strain amplitudes ($<10^{-4}$), the planar dislocation structures typical for low SFE materials prevail, i.e. corduroy, dislocation alignments and planar slip bands. For high strain amplitudes ($>10^{-3}$) walls-and-channels and cells typical for high SFE materials prevail. Xia et al. (1992) studied a manganese-alloyed austenitic stainless steels and found similar dislocation arrangements. Similar dislocation arrangements are also observed in the austenite phase of duplex stainless steels. In the ferrite phase of duplex stainless steels, veins-and-channels and ladder structures are observed (Degallaix et al., 1995). In the ferrite phase, the observed dislocation structures do not change markedly with the strain amplitude.

1.5 Fatigue crack initiation

Traditionally the failure is divided into three phases: crack initiation, crack growth or propagation, and final fracture. During the initiation period, a visible crack or cracks form. The initiated cracks then grow and at some point the growing cracks have weakened the structure so much that the load bearing capacity is exceeded and final fracture occurs.

At very low load amplitudes, near the fatigue threshold, most of the life is spent on the crack initiation phase. As the load amplitudes increase, the proportion of the life spent in the propagation phase increases rapidly. The distinction between the initiation and the propagation phases is somewhat ambiguous. With the development of better methods of detecting cracks, smaller cracks have become detectable and the initiation period has shortened. Also considerable scatter now exists in the definition of initiation: it can mean cracks visible to the naked eye (in the range of 1 – 2 mm) or it can mean smallest cracks visible in the electron microscope (in the range of a few μm). It has been suggested that initiation is absent altogether and that first undetectable cracks initiate during the first load cycle (Miller, 1999). Crack initiation typically takes place at material inhomogenities. These can be for example persistent slip bands caused by cyclic loading, grain boundaries or nonmetallic inclusions. The fatigue strength depends on the "weakest link", e.g., from the largest inclusion present (Murakami & Endo, 1993; Murakami et al., 1994).

1.6 Fatigue crack growth

After crack initiation, the fatigue damage is concentrated to the highly strained area of the crack tip. In small crack lengths the crack growth rate is highly dependent on the local microstructure and coalescence of cracks (Miller 1999). After the crack length is more than about 3 times the grain size, the crack growth can be described by a single mechanical parameter (Kawagoishi et al. 2000).

Ductile metals deform plastically at the highly stressed area around the crack tip. In the area where stresses exceed the yield strength of the material, the monotonic plastic zone is formed. The plastic zone alters the stress and strain distribution at the crack tip. In the cyclic case, unloading reverses the stress direction. The changes in the stresses and strains are given by a solution identical to that of monotonic loading but with yield strain and stress replaced by twice their values (Rice, 1967). Consequently, a much smaller cyclic plastic zone forms inside the monotonic plastic zone (Figure 1). The formation of these plastic zones was also experimentally verified (e.g., Davidson & Lankford, 1976; Williams et al., 1980). Lankford et al. (1984) studied the crack tip deformation of small fatigue cracks and found that the measured crack tip opening (CTOD) and crack tip plastic zones were much larger than those predicted based on long

crack models. They concluded that the large plastic zone compared to the crack depth at least partly explained the anomalous crack growth rate of small cracks.

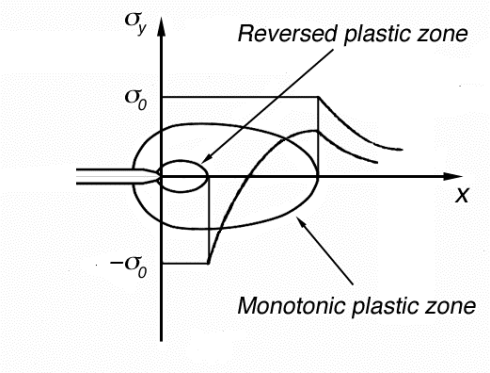

Figure 1. Schematic illustration of monotonic and cyclic plastic zones and stress distributions (after Rice, 1967).

The crack propagation phase is subdivided based on the plane of the crack advance. The crack can grow by two processes and corresponding planes: shear decohesion on one plane directly ahead of the crack tip, or shear decohesion of two mutually perpendicular planes inclined at about 45° to the crack plane (Miller, 1999). The former is termed stage I and the latter stage II crack growth. Stage I crack growth is mainly observed at small applied load ranges, whereas stage II is typical for high loads. Cheng & Laird (1983) suggested that the transition occurs due to work hardening on the primary slip system. The work hardening causes strain to be transferred partly to the secondary slip system. This causes persistent slip band (PSB) formation on the secondary slip system and transition from stage I to stage II crack growth. The orientation of the crystal relative to loading affects the stresses on the secondary slip system and consequently the transition behavior. The higher the stresses on the secondary slip system are, the earlier the transition to stage II crack growth occurs.

Lukáš & Kunz (1984) and Lukáš et al. (1985) studied the dislocation structures ahead of a fatigue crack tip in copper (Figure 2). They found that the high strains directly ahead of the crack tip are extended by the formation of slip bands. The crack was found to follow the path of the highest local deformation. At low amplitude loading, the zone of the cell structure ahead of the crack tip is small and the crack follows PSBs. With higher load amplitudes, the crack tip is surrounded by an extensive zone of dislocation cells which does not contain preferred paths, and the crack propagates non-crystallographically. It was also found that the crack growth rate was proportional to the local crack tip plastic strain (Lukáš et al., 1985).

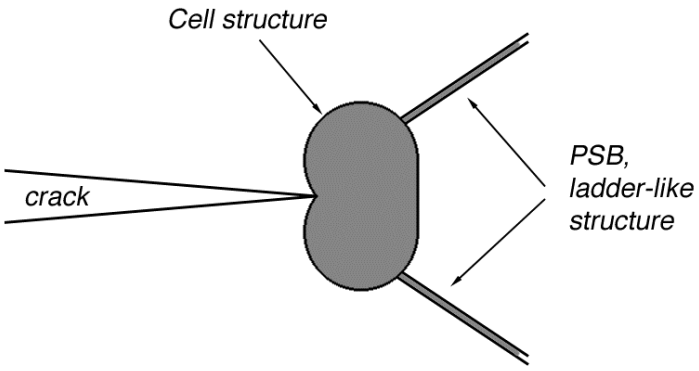

Figure 2. Dislocation structures ahead of fatigue crack tip in copper (after Lukášet al., 1985).

The portions of fatigue life spent in initiation, stage I and stage II of crack growth depend on the environment, material and loading (Socie & Bannantine, 1988). The fracture surface left by a stage I crack appears faceted. The facets form as the crack changes the plane of advance. By contrast, stage II cracks leave ripple-like markings, striations, which describe the crack advance by cycle. Several models have been proposed to explain the formation of striations. The blunting model, proposed by Laird & Smith (1962), is presented in Figure 3. Tomkins (1968) presented an alternative model (Figure 4). His model was criticized by Laird & de la Veaux (1977). The model was further developed in later publications (Tomkins, 1980; 1981; 1983a). The main difference between these two models is that slip is condensed to either one or several sets of PSBs ahead the crack tip. Neumann (1969), Pelloux (1969) and Vehoff & Neumann (1978) developed an alternative model for striation formation (Figure 5). In this model, the crack forms a V-shaped tip and advances by alternating slip on two slip bands. This model was supported by recent fracture surface studies and was developed further by Bichler & Pippan (1999). It should be noted, however that great variation in the appearance of fatigue striations is perceived in different materials, environments and loading conditions. Hence, it may be that a single model for their formation is not conceivable.

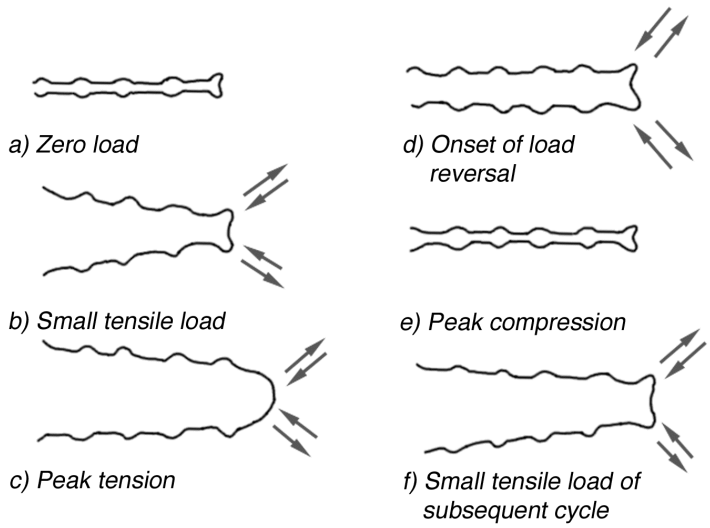

Figure 3. The blunting model of striation formation (after Laird & Smith, 1962).

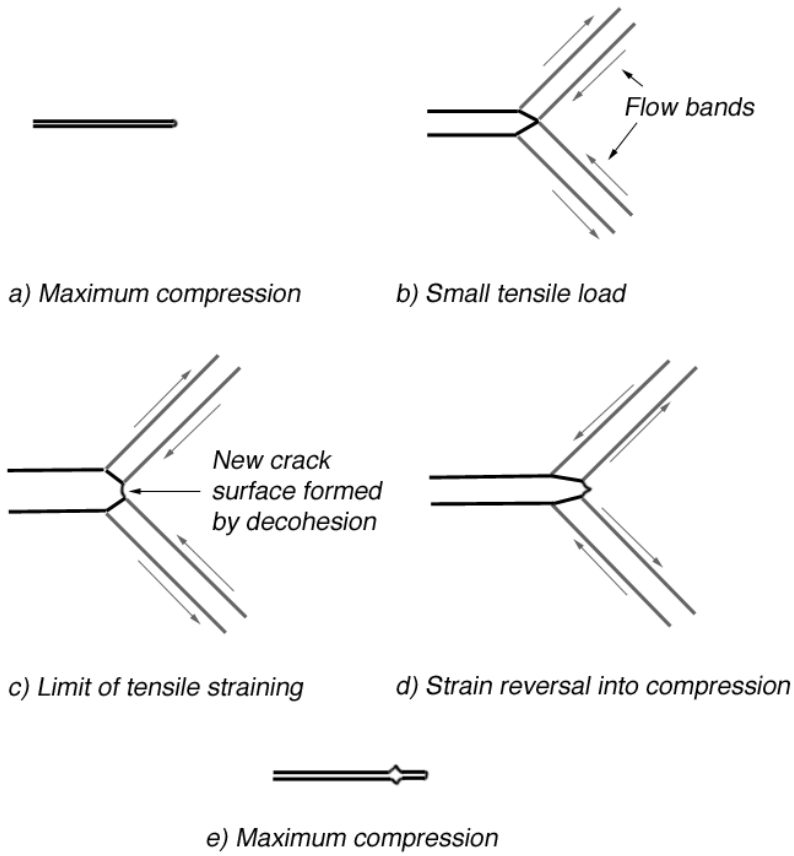

Figure 4. The Tomkins model of striation formation (after Tomkins, 1968).

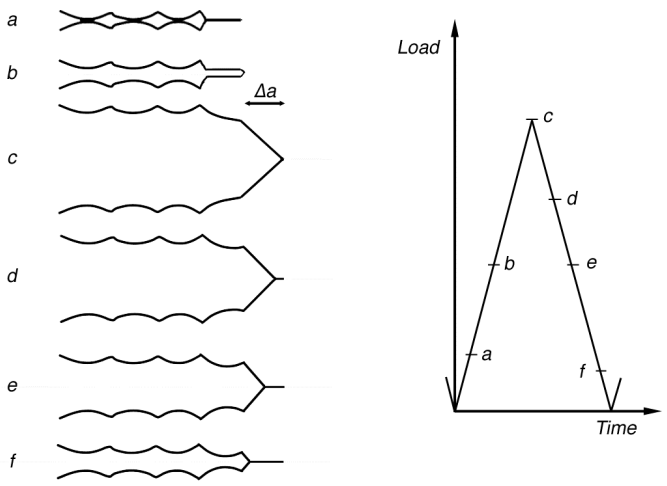

Figure 5. The Neumann-Pelloux-Bichler model of striation formation (after Bichler & Pippan, 1999).

Striation spacing is generally considered to be an indicator of the crack advance per cycle. However, in-situ observations have revealed that, in the near-threshold regime where crack growth rate is low, this is not necessarily true. As the crack growth rate diminishes, more than one cycle is needed to form each striation. Finally, very close to the threshold the striation spacing reaches a minimum of 0.1 – 0.4 μm and is independent of the crack growth rate (Davidson & Lankford, 1992). Recently, Uchida et al. (1999) showed that the stress ratio (R) could also be determined from the fracture surface by studying the height of the striations.

At greater crack growth rates the striations give a direct indication of the crack growth rate. Since fatigue crack growth does not occur continuously, but the advancing crack (at least locally) slows or stops at microstructural barriers (Tanaka, 1989), the growth rate calculated from striation spacing is a conservative estimate. Tanaka et al. (1981) proposed a correlation between the striation spacing and ΔK-level (see sections 1.7 and 1.8):

$$\frac{S}{b} = 10^3 \left(\frac{\Delta K}{10E\sqrt{b}} \right)^2 = 10\frac{\Delta J}{Eb}, \tag{8}$$

where S is the striation spacing,
b is the atomic distance or Burgers vector,
ΔK is the stress intensity factor range (see section 1.7) and
ΔJ is the J integral range (see section 1.7).

1.7 Fracture mechanics

In 1920 Griffith (1920) published his classic paper on the phenomena of rupture and flow of solids. His paper concludes that the strength of brittle glass samples was determined by the size of flaws present. He proposed that the amount of surface energy required by the growing crack

determined the stress needed to break the sample. He then concluded that the strength of a cracked plate was inversely proportional to the square root of the length of the crack present. Later Irwin (1947) generalized this idea to include energy dissipated by plastic flow and named the defined parameter energy release rate, G (Irwin, 1957). With the help of a stress solution of a cracked plate given by Westergaard (1939), it was then shown that the crack tip stresses are proportional to a quantity called the stress intensity factor, given for plane stress by:

$$K = \left(\frac{EG}{\pi} \right)^{\frac{1}{2}}, \tag{9}$$

where K is the stress intensity factor (MPa $m^{0.5}$) and
G is the energy release rate (J mm^{-2}).

In a force-controlled load case the solution of G usually gives the $\sqrt{a}$ dependence noticed by Griffith (1920). In a displacement-controlled load case, the dependence of K on the crack length a can be quite different or even nonexistent, as for example in the case of displacement-controlled loading of a very long crack in an infinite plate.

The linear elastic fracture mechanics (LEFM) parameter K has been a very successful tool in describing many failure mechanisms that feature crack growth. However, with high stresses or small crack lengths the small scale yielding condition of K is violated, and K loses its validity. Rice & Rosengren (1968), Rice (1968) and Hutchinson (1968) proposed that the crack tip could be characterized by a line integral (J-integral or J) around the crack tip even in the case of plasticity exceeding the small scale yielding condition of K:

$$J = \int_{\Gamma} \left(W dy - T_t \cdot \frac{du}{dx} ds \right), \tag{10}$$

where W is the strain energy density,
T_t is the traction vector and
Γ is a path surrounding the crack tip.

The elastic-plastic fracture mechanics (EPFM) parameter J is directly related to K in the case of small scale yielding (Rice & Rosengren, 1968):

$$J = \frac{\left(1 - \nu^2\right) K_I^2}{E}. \tag{11}$$

J is extensively used for crack tip characterization in inelastic load cases. In the case of thermal gradients, the conventional definition of J loses its path independence. Wilson & Yu (1979) showed that J can be calculated also in thermal stress crack problems, but the solution involves a computationally difficult area integral:

$$J = \frac{E\alpha}{1-2\nu}\int_{A_0}\left(T\frac{\partial}{\partial x_1}(\varepsilon_{ii}) - \frac{1}{2}\frac{\partial}{\partial x_1}(T\varepsilon_{ii})\right)dA, \tag{12}$$

where T is temperature.

Following the analysis of Wilson and Yu (1979) the J equation for an arbitrary eigenstrain distribution can be solved and used to solve J in a residual stress field, which again involves an area integral.

1.8 Crack growth models for fatigue design

Paris et al. (1961) and Paris & Erdogan (1963) showed that the fatigue crack growth rate could be characterized with the LEFM-based parameter, ΔK:

$$\frac{da}{dN} = \frac{(\Delta K)^4}{M}, \tag{13}$$

where M is a material constant and
ΔK is the stress intensity range.

The empirical Paris-Erdogan equation is now by far the most used crack growth model (see Tomkins (1984) for a review of classical crack growth based fatigue analysis). Usually the exponent is also considered as a material constant or a fitting parameter and the equation is presented in the following, more general form:

$$\frac{da}{dN} = C_1\Delta K^{m_1}, \tag{14}$$

where C_1 and m_1 are material constants.

With very high loading the small scale yielding condition of LEFM is no longer valid and ductile tearing fracture and other fracture mechanisms take part in the process. Hence the applicability of Paris-Erdogan law is limited at high ΔK-values. With low ΔK-values the crack growth rate is observed to deviate from the Paris law (equation 14) and to decrease rapidly. This point is termed the threshold stress intensity range, ΔK_{th}. Consequently, the fatigue crack growth is divided into three regimes. A schematic crack growth plot is shown in Figure 6.

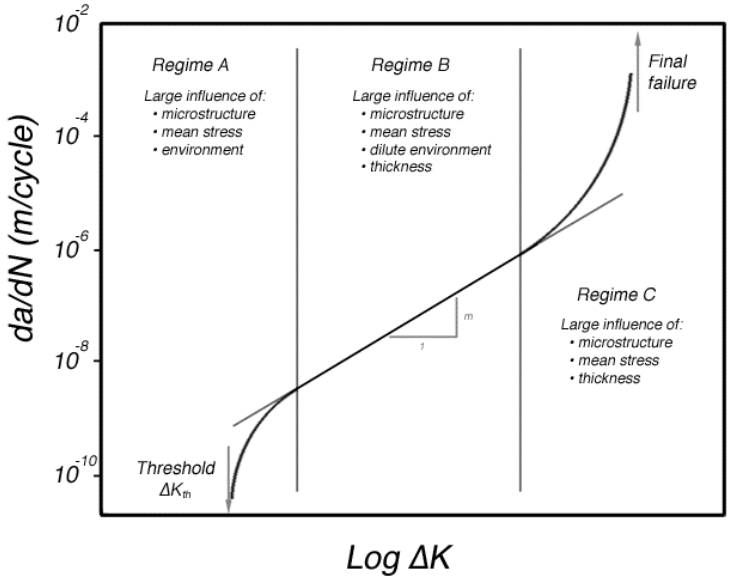

Figure 6. Schematic crack growth plot with Paris parameters (after Tanaka, 1989).

At small crack lengths, the applied stress to produce a certain K-value is very high. With high stresses the plastic zone of the crack is large compared to the length of the crack and the small scale yielding condition of K is violated. Consequently, the observed crack growth rates are higher than predicted by the Paris law. Because the fatigue life spent during the early crack growth is very long, the inability of the Paris law to correctly predict the small crack growth is a serious handicap.

The limits of the linear elastic fracture mechanics were extended by the introduction of elastic-plastic fracture mechanics (see Paragraph 1.7). Similarly the limitations of the Paris law that are caused by the limitations of linear elastic fracture mechanics could be extended by the use of EPFM parameters such as J. Dowling & Begley (1976) and Dowling (1976; 1977) were among the first to test the applicability of the elastic-plastic J parameter to fatigue crack growth characterization. They concluded that for ductile materials and long cracks J characterized the crack growth for high load state and ligament plasticity. Hoshide et al. (1985) tried to correlate small crack growth with ΔJ and found that with crack lengths greater than three times the grain size of the material correlation could be found. For smaller crack lengths, the coalescence of cracks caused a higher than predicted crack growth rate.

Observed fatigue crack growth depends on numerous other factors in addition to ΔK or ΔJ. For example, the load ratio R, environment, microstructure, temperature, overloads, and short cracks change the crack growth rate. Elber (1970) proposed that these effects could be explained by premature crack closure, which reduces the effective ΔK. The concept has

been used widely since then. Dowling & Begley (1976) and Dowling (1976) corrected their ΔJ values for crack closure, which appeared at nonzero (compressive) load in their analysis. Chen et al. (1997) concluded that both ΔJ and closure-corrected ΔJ_{eff} were successful in predicting high temperature crack growth in AISI 304 steel. Sadananda & Vasudevan (1995) showed that crack closure is often overestimated and is not sufficient to explain the observed anomalies in crack growth. They proposed instead that fatigue crack growth is dependent upon two parameters: K_{max} and ΔK (or the equivalent J_{max} and ΔJ) (Vasudevan et al., 1992; 1993; Vasudevan & Sadananda, 1993; 1995a; 1995b; Sadananda & Vasudevan, 1995; 1997a; 1997b).

The main disadvantage of the K- and J-based models is the problem with predicting small crack growth and crack growth from notches (Pippan et al., 1986). In addition, the calculations required for the assessment of loading at the crack tip are often very difficult. Many analytical solutions for K are available (e.g., Murakami, 1987). For J the solutions are not that readily available. Dowling (1977) presented the following approximate J solution for small half-circular surface cracks:

$$J = J_e + J_p = 3.2 W_e a + 5.0 W_p a = 3.2 \frac{\sigma^2}{2E} + 5.0 \frac{\sigma \varepsilon_p}{s_1 + 1}, \qquad (15)$$

where J_e is the elastic part of J,
J_p is the plastic part of J,
W_e and W_p are the elastic and plastic strain density and
s_1 is the strain hardening exponent and
a is the crack depth.

Nowadays J-based design is usually based on J calculated from finite element (FE) analysis. The calculations are rather demanding due to the elastic-plastic modeling required. If the temperature is not uniform throughout the specimen, additional difficulties arise due to the area integrals present.

Several extensions and modifications have been proposed to the above mentioned crack growth laws (e.g., review by Hussain, 1997). Many of them are developed to extend the applicability of the traditional LEFM and J approaches to small crack growth and crack growth from notches. El Haddad et al. (1980) proposed that an effective crack length a_{eff} should be added to the crack length a when calculating ΔK of ΔJ to account for the fatigue limit. The effective crack length a_{eff} can be obtained if the threshold stress intensity range and fatigue limit of the material are known:

$$a_{eff} = \left(\frac{\Delta K_{th}}{\Delta \sigma_e} \right)^2 \frac{1}{\pi}, \qquad (16)$$

where $\Delta\sigma_e$ is the fatigue limit.

Lantaigne & Baïlon (1981) suggested an improved model for near-threshold crack growth. In their model fatigue damage was modeled to cumulate in a certain damage zone ahead of the crack tip. Lal (1994) proposed that the applicability of the Paris approach could be extended to small and near-unstable crack growth by dividing the crack growth into three regimes. The crack growth in each regime was described by a Paris type equation (equation 14) with different material constants C_2 and m_2.

Crack growth from notches has also been successfully predicted by replacing the stress intensity factor K with a strain intensity factor K_ε (Leis, 1985; Hatanaka et al., 1989):

$$K_\varepsilon = \frac{K}{E} = \varepsilon\sqrt{\pi a}Y, \tag{17}$$

where Y is a geometry factor.

When the Paris law (equation 14) is used together with the strain intensity factor, the corresponding material parameters C and m have the following relationships:

$$m_1 = m_2 \tag{18}$$

$$C_1 = \frac{C_2}{E^{m_2}}, \tag{19}$$

where the subscripts 1 and 2 denote parameters to be used with stress and strain intensity factors, respectively.

Liu & Kobayashi (1980) proposed the following relation based on the unzipping model for crack growth:

$$\frac{da}{dN} = 0.02\left(1-\nu^2\right)\frac{(\Delta K)^2}{E\sigma_{yc}} = 0.02\frac{\Delta J}{\sigma_{yc}}, \tag{20}$$

where σ_{yc} is the cyclic yield stress.

Tomkins (1968) proposed a crack growth model based on the micromechanism of fatigue crack growth (see section 1.4). The basic assumption in the model is that the crack growth rate can be calculated from the size of the crack tip deformation zone:

$$\Delta a = \varepsilon_p D, \tag{21}$$

where Δa is the crack advance,
ε_p is the applied plastic strain and
D is the deformation zone size.

To calculate D, Tomkins (1968) used the following solution:

$$\frac{D}{a} \approx \sec\left(\frac{\pi}{2}\right). \tag{22}$$

This gives the following cyclic crack growth law (Tomkins 1968):

$$\frac{da}{dN} = C_3 \Delta\varepsilon_p a, \tag{23}$$

where C_3 is a material constant.

In later publications, the equation was modified to (Tomkins 1980; 1981; 1983a):

$$\frac{da}{dN} = C_3 \Delta\varepsilon_p a \frac{\sigma_t^2}{\sigma_f^2}, \tag{24}$$

where σ_t is the stress amplitude and
σ_f is the material flow stress.

Solomon (1972) proposed the following, more generalized crack growth law for high strain fatigue:

$$\frac{da}{dN} = C_4 \Delta\varepsilon_p^{m_4} a, \tag{25}$$

where C_4 and m_4 are material constants and
$\Delta\varepsilon_p$ is the bulk plastic strain range.

Equation 25 cannot be used for high cycle fatigue, where $\varepsilon_p << \varepsilon_e$. To bridge the gap between high strain fatigue and the Paris law, Haigh & Skelton (1978) and Skelton (1982) proposed an equivalent strain range:

$$\varepsilon_{eq} = \varepsilon_p + q\varepsilon_e, \tag{26}$$

where ε_{eq} is the equivalent strain,
ε_p is the plastic strain,
ε_e is the elastic strain and
q is a parameter describing the part of the cycle that the crack stays open; a value of 0.5 was chosen based on crack closure measurements by electric conduction across the crack faces. With q=0.5 the ε_{eq} is equal to arithmetic mean of total and plastic strain.

High strain fatigue and linear elastic crack growth can then be unified by defining the strain intensity factor in terms of equivalent strain. This parameter is roughly equal to ΔJ (Starkey & Skelton, 1982):

$$\Delta K_\varepsilon = \left(\Delta\varepsilon_p + q\varepsilon_e\right)(\pi a)^{\frac{1}{2}}. \tag{27}$$

Ahmad & Yates (1994) also proposed a fatigue crack growth model based on the Tomkins model. In their model, the Tomkins term was combined with a term for long crack growth to obtain a unified model for cracks growing from notches:

$$\frac{da}{dN} = C_5 \Delta K^{m_5} - T + C_6 a \Delta \varepsilon_p^{(1+2m_6)}, \tag{28}$$

where T is a threshold value for crack growth and
C_5, C_6, m_5 and m_6 are material constants.

More recently Skelton et al. (1998) proposed a model for correlating tested low cycle fatigue (LCF) properties to LEFM fatigue crack growth via an energy-based parameter. In this model the crack growth rate is calculated from the energy required to fail the specimen and the hysteresis energy per cycle, i.e.:

$$\frac{da}{dN} = \frac{w_c}{W_f} = \frac{1}{1+\beta}\left(\frac{\Delta J}{I_\beta W_f}\right) f(\beta), \tag{29}$$

where w_c is the hysteresis energy per cycle,
W_f is the energy required for failure,
β is a material constant,
I_β is a constant depending on the value of β and
$f(\beta)$ is 1 for plane stress.

Taira et al. (1976) studied isothermal high temperature low cycle fatigue of 0.16% carbon steel and AISI 304 austenitic stainless steel. They proposed the following crack growth law:

$$\frac{da}{dN} = C_7 \Delta \varepsilon^{m_7} a, \tag{30}$$

where C_7 and m_7 are fitting parameters depending on the material and test setup.

Equation 30 was found to hold for both plastic and total strain range. The exponent m_7 was seen to be almost constant over a wide temperature range (Figure 7).

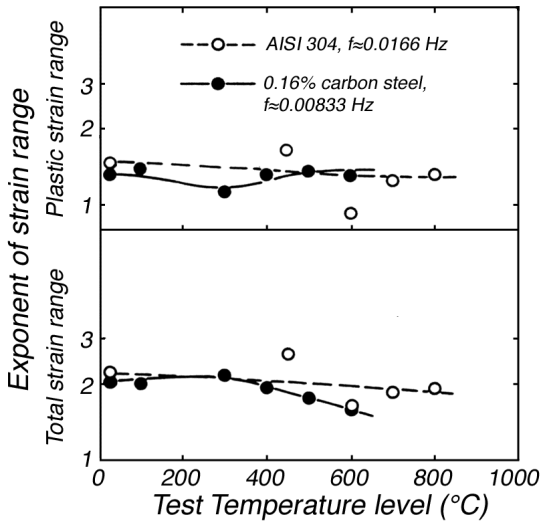

Figure 7. The temperature dependence of exponent α in equation 30 (after Taira et al., 1976).

Nisitani et al. (1992) proposed the following small crack growth model for stress ranges below the yield stress:

$$\frac{da}{dN} = C_8 \Delta\sigma^{m_8} a, \tag{31}$$

where C_8 and m_8 are material parameters.

According to Nisitani et al. (1992) the apparent contradiction between equation 31 and the Paris law (equation 14) can be explained by their different range of applicability. With long cracks and small stresses the crack tip cyclic plastic zone size is proportional to ΔK^{m_1} and the Paris law describes crack growth. With small cracks and large stresses the small scale yielding condition of LEFM is violated. In this regime, the crack tip plastic zone is given by equation 32 and crack growth rate can be predicted with equation 31.

$$\frac{D}{a} \propto \left(\frac{\sigma}{\sigma_y} \right)^{m_8}, \tag{32}$$

where D is the plastic zone size.

Nisitani et al. (1992) noted that equation 31 is not suitable for comparing different materials due to differences in the values of the parameters C_8 and m_8. To overcome this, he proposed the following equation in which the material properties are partly included:

$$\frac{da}{dN} = C_9 \left(\frac{\Delta\sigma}{\sigma_y} \right)^{m_9} a, \tag{33}$$

where C_9 and m_9 are again material parameters.

Kawagoishi et al. (2000) recently studied the range of applicability of this equation with 0.42% carbon steel. It was shown that the lower limit of applicability of equation 31 is around a crack length of 3 times the grain size of the material (d). Below this value, the strong influence of the microstructure prohibits the use of a mechanical parameter. Microstructural influence continues to be significant until about 8d, but below this value the mean crack growth can be estimated with a mechanical parameter. When cracks grow long enough to satisfy the small scale yielding condition of LEFM, the crack growth becomes ΔK-controlled, and equation 31 is no longer valid. With higher stress amplitudes, equation 31 is applicable to greater crack lengths. Kawagoishi et al. (2000) described these different regimes of crack growth with the following map (Figure 8).

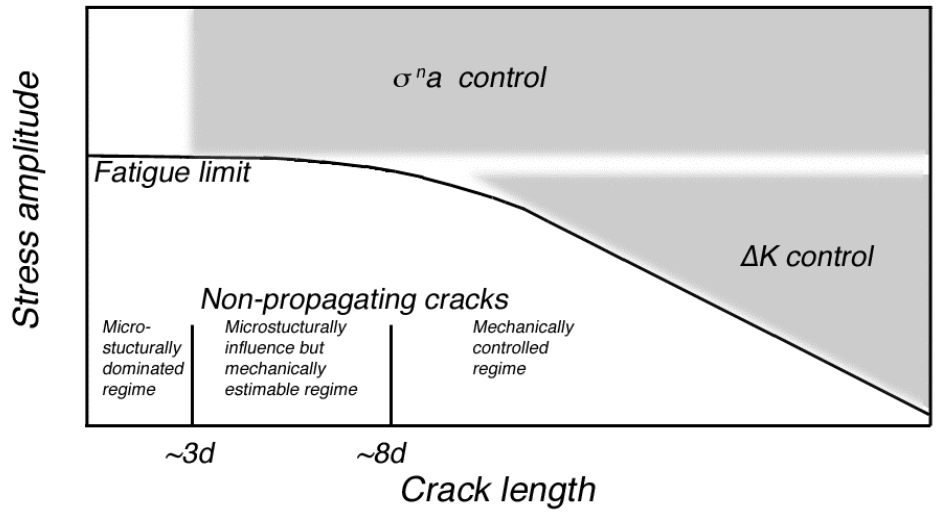

Figure 8. The applicability of the Paris law (equation 14) and equation 31 as a function of crack length and stress amplitude (after Kawagoishi et al., 2000).

It should be noted that equations 30 and 31 are linearly dependent in the linear-elastic region studied by Nisitani et al. (1992) and Kawagoishi et al. (2000). The equations are equal if:

$$m_7 = m_8 \text{ and} \tag{34}$$

$$C_7 = \frac{C_8}{E^{m_8}}, \tag{35}$$

where E is the Young's modulus.

1.9 Fatigue properties of austenitic and duplex stainless steels

The fatigue properties of different stainless steels have been studied widely at different temperatures and environments. Both S-N plots and crack

growth data are widely available in various environments. In Figure 9, the S-N plots for AISI 304 and AISI 316NG stainless steels in air and water are presented. In Figure 10 the crack growth rates of various austenitic stainless steels in different environments are presented. From the presented crack growth data, the material constants C_1 and m_1 of the Paris law (equation 14) can be extracted. The extracted values are presented in Table 1. Figure 11 shows the crack growth rate for a duplex stainless steel in air.

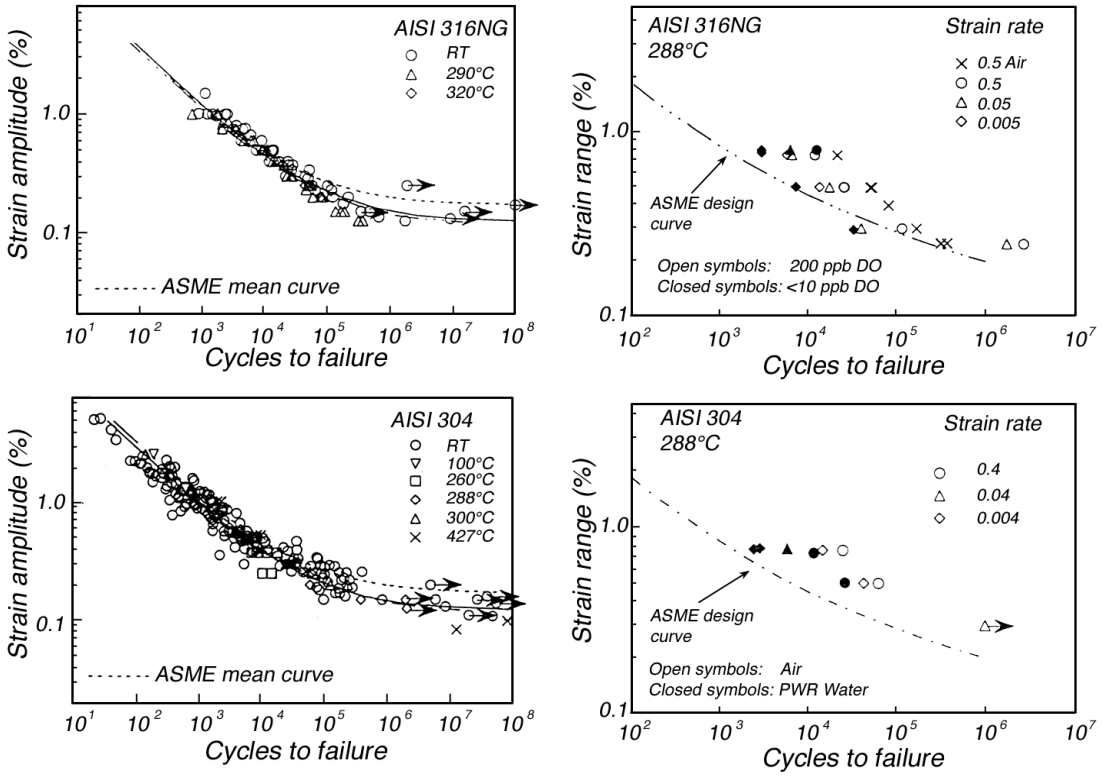

Figure 9. S-N plots for AISI 304 and AISI 316NG austenitic stainless steels in air and water (after Chopra & Gavenda, 1998).

Table 1. The material constants C_1 and m_1 of the Paris law from Figures 10 and 11.

Material	C	m
AISI 304, 316, 321, 348 at 25°C	4.6×10^{-9}	3.1
AISI 304 at 593°C	4.7×10^{-8}	2.8
AISI 316 at 593°C	7.3×10^{-7}	2.1
AISI 321 at 593°C	1.2×10^{-7}	2.6
AISI 348 at 593°c	1.2×10^{-8}	3.1
20 Cr, 5.5Ni Duplex at RT	4.6×10^{-11}	3.1

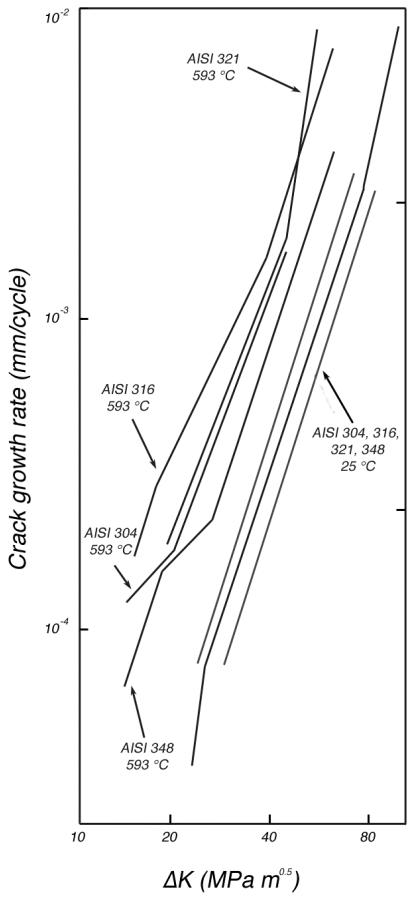

Figure 10. Crack growth data for austenitic stainless steels (after Boyer, 1986).

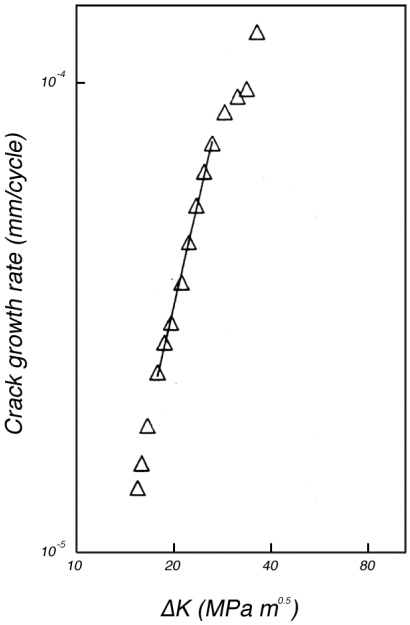

Figure 11. Crack growth data for A790-grade duplex stainless steels fatigued in air at RT (after Rajanna et al., 1997).

1.10 Multiaxial fatigue

Multiaxial loading shortens expected fatigue life as compared to uniaxial loading. The fatigue life in biaxial loading can be reduced by more than a factor of 2 as compared to uniaxial loading (Itoh et al., 1995; 2000). Numerous models have been proposed to predict the effect of various proportional or nonproportional load paths (e.g., Brown & Miller, 1982; You & Lee, 1996; Socie & Marquis, 2000). The proposed multiaxial fatigue models can be broadly classified into the following approaches (Socie & Marquis, 2000): stress-based models, strain-based models, energy-based models, critical plane models and fracture mechanics models. Stress and strain based models aim to extend the use of the known phenomenological Wöhler or Coffin-Manson models by providing an equivalent damage parameter to be used for multiaxial loading. In energy-based models, the fatigue life is related to the plastic strain energy dissipated during loading. In critical plane models, it is noted that fatigue crack growth can occur predominantly along planes of maximum shear or tensile strain and no single damage model can be expected to be successful for both modes (e.g., Socie, 1987; Socie & Bannantine, 1988). The fracture mechanics models aim to extend crack growth models, such as the Paris law (Equation 14), for mixed mode loading.

Marsh (1981) used the following formulas to convert equi-biaxial thermal fatigue loading to equivalent uniaxial loading:

$$\varepsilon_{pb} = \frac{1}{2}\varepsilon_{pu}, \tag{36}$$

$$\varepsilon_{eb} = \varepsilon_{eu}(1-\nu), \tag{37}$$

where subscripts e and p refer to elastic and plastic, and b and u refer to biaxial and uniaxial loading, respectively. These simple formulas assume, that biaxial loading can be correlated with uniaxial loading by subtracting strain caused by the Poisson effect of the transverse loading ($\nu\varepsilon_{eu}$ for elastic and $\nu_{eff}\varepsilon_{pu}$ for the plastic case).

1.11 Environmental effects

Fatigue crack growth tends to accelerate in aggressive environments. Even fatigue tests conducted in air show significantly higher crack growth rates than tests conducted in vacuum (Wadsworth & Hutchings, 1958). In more aggressive environments, time dependent stress corrosion cracking (SCC) accelerates the crack growth rate. According to McEvily & Wei (1971) and Gabetta et al. (1990) the environmental effects on fatigue crack growth can be divided into true corrosion fatigue (TCF) and stress corrosion fatigue (SCF) (Figure 12).

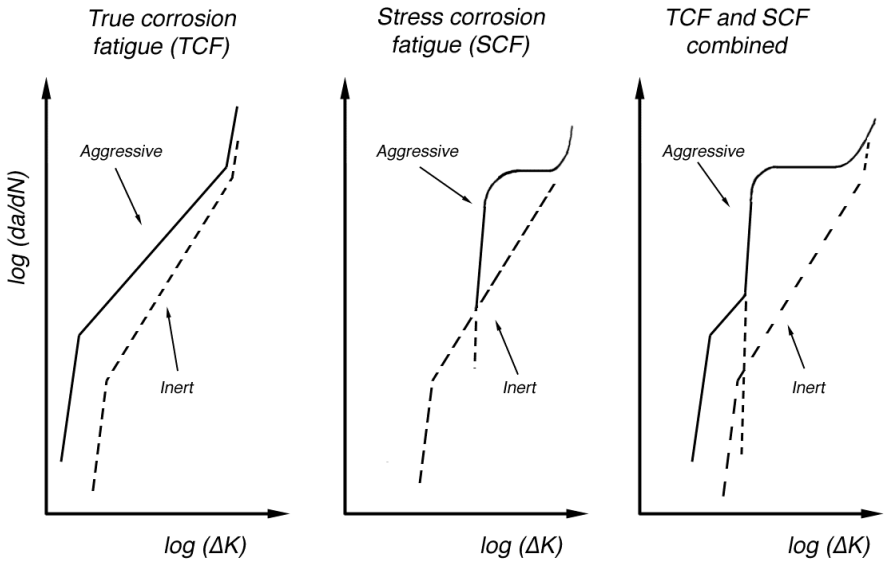

Figure 12. Separation of corrosion fatigue to true corrosion fatigue and stress corrosion fatigue (after McEvily & Wei, 1971; Gabetta et al., 1990).

In true corrosion fatigue, the crack growth rate follows the conventional Paris law (equation 14), and the environment merely has an effect on changing the material constants C_1 and m_1 to reflect the accelerated crack growth rate. The fracture surfaces show ductile features, such as ductile striations, similar to the fracture surfaces produced, e.g., in air.

In stress corrosion fatigue, a time-dependent crack growth component accelerates the crack growth. The fracture surfaces typically show brittle striations or intergranular fracture. The effect of test frequency is decisive. The stress corrosion fatigue crack growth can be correlated to the stress corrosion crack growth under similar environmental and loading conditions.

The maximum expected combined crack growth rate can be expressed as a combination of the crack growth rates caused by true corrosion fatigue and stress corrosion (Gabetta et al., 1990):

$$\left[\frac{da}{dN}\right]=\left[\frac{da}{dN}\right]_{TCF}+t\left[\frac{da}{dN}\right]_{SCC}, \tag{38}$$

where the true corrosion fatigue crack growth (subscript TCF) follows the Paris law (equation 14), and stress corrosion crack growth (subscript SCC) is almost constant and can be estimated from slow strain rate test (SSRT) results (Gabetta et al., 1990). The stress corrosion component is present only during the time when the applied ΔK is large enough to exceed the limiting K_{ISCC}. This time is a function of the test frequency and is represented by the term t in the equation.

Two mechanisms have been suggested to account for the environmental effects on fatigue crack growth: slip oxidation/dissolution (Ford, 1993) and hydrogen-induced cracking (Hänninen et al., 1986). In the former mechanism the crack growth rate is related to the oxidation rate at the strained crack tip and periodicity of oxide rupture at the crack tip. In the latter mechanism crack growth is related to localized hydrogen induced cracking resulting from hydrogen generation due to the corrosion reaction. In stainless steels the fact that fatigue life is longer in water containing low dissolved oxygen than in high dissolved oxygen water suggests that the contribution of slip oxidation/dissolution mechanism is limited (Chopra & Muscara, 2000). Studies on crack initiation in water environments reveal that the observed decrease in fatigue life is caused primarily by the effects of environment on the growth of small cracks less than 500 μm deep (Chopra & Muscara, 2000). The environmental effects depend on strain, dissolved oxygen (DO), strain rate and temperature. The main effects and threshold values of the parameters are summarized in Table 2.

Table 2. The effect of various factors on the decrease of the fatigue life of austenitic stainless steels in aqueous environment (Chopra & Muscara, 2000).

Factor	Effect
Dissolved oxygen (DO)	The environmental effects are more pronounced in low-DO (<0.01 ppm) than in high-DO water. In high-DO water the environmental effects are moderate when coductivity is low and electrochemical potential (ECP) has reached a stable value. In low-DO water conductivity or additions of lithium and boron have no effect on the fatigue life.
Applied strain	A minimum threshold strain is required for the environmental decrease of fatigue life. During each cycle, the environmental effects are limited to the part of the cycle where the applied strain is above this threshold.
Strain rate	In high-DO water with low conductivity and stable ECP, fatigue life is insensitive to strain rate. In low-DO water fatigue life decreases logarithmically with decreasing strain rate below about 0.004 s^{-1}.
Temperature	High temperature increases the effect of environment. Environmental effects are minimal below 200°C and become significant above 250°C. Fatigue life is insensitive to changes in temperature in the range of 250 – 330°C.

Higuchi & Iida (1991) have suggested that the effect of environment for austenitic stainless steels can be expressed in terms of fatigue life

correction factor F_{en}, which is defined as the ratio of life in air at room temperature to that in water at service temperature. For stainless steels, F_{en} can be estimated as follows (Chopra & Muscara, 2000):

$$F_{en} = e^{0.935 - T'\dot{\varepsilon}'O'}, \tag{39}$$

where T'=0 for T<180°C,
T'=(T-180)/40 for 180<T<220°C,
T'=1 for T>220°C,
$\dot{\varepsilon}'$=0 for $\dot{\varepsilon}$>0.004 s^{-1},
$\dot{\varepsilon}'$=ln($\dot{\varepsilon}$/0.004) for 0.000004<$\dot{\varepsilon}$<0.004 s^{-1},
$\dot{\varepsilon}'$=ln(0.000004/0.004) for $\dot{\varepsilon}$<0.000004 s^{-1},
O'=0.260 for DO<0.05 ppm and
O'=0 for DO>0.05ppm.

Corrosion fatigue crack growth in austenitic stainless steels in aqueous environments has been studied extensively (e.g., Kawakubo et al., 1980; Endo et al., 1983; Hishida et al., 1986). Kawakubo et al. (1980) measured crack growth rates of AISI 304 type stainless steel in oxygenated water at 290°C in the solution treated and sensitized conditions (Figure 13).

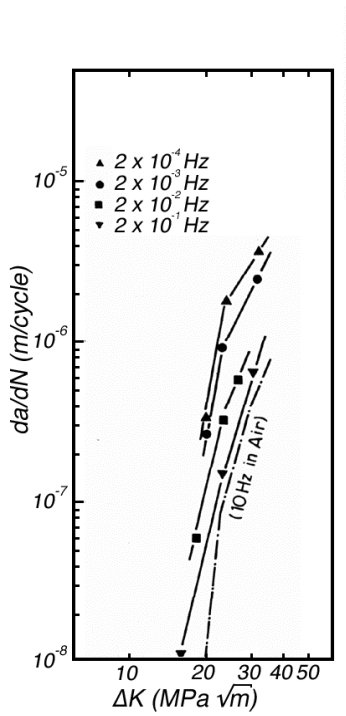

Figure 13. Crack growth rates of AISI 304 stainless steel in oxygenated water at 290°C (sinusoidal wave loading, frequency 10Hz, stress ratio 0.1, O_2 concentration 8 ppm, electrical conductivity <10^{-4} S/m) (after Kawakubo et al., 1980).

1.12 Dynamic strain ageing

In certain ranges of temperatures and strain rates, many solid solutions exhibit serrated yielding behavior (Portevin–Le Chatelier effect). The phenomenon is explained by interaction between moving dislocations and diffusing solute atoms, i.e. dynamic strain ageing (DSA). According to the model proposed by McCormick (1972), the movement of dislocations during plastic deformation is discontinuous. Dislocations are temporarily arrested at obstacles. They break free and advance with high velocity until they are arrested again at the next obstacle. The average dislocation velocity is determined mainly by the average arrest time spent at the obstacles.

If the arrest time of the dislocation at an obstacle is sufficiently long, the dislocation may be locked by solute atoms, and stress increase is needed for the dislocations to be released from the locking atmosphere formed by the solute atoms. The ageing time required to form the locking atmosphere depends on the diffusion rate of the solute atoms. During plastic deformation, the ageing time decreases due to vacancy production. Dislocation multiplication caused by straining increases the waiting time. At some critical strain the waiting time becomes equal to the required ageing time, and serrated yielding begins (McCormick, 1972).

The strength of the material is increased by dynamic strain ageing. The fracture toughness, ductility and low cycle fatigue resistance are reduced (e.g., Srinivasan et al. 1997). For a given alloy, DSA occurs typically for very limited temperature and strain rate regimes. Dynamic strain ageing is observed in different austenitic stainless steels at temperatures 200–600°C (Srinivasan et al., 1997; Nilsson & Thorvaldsson, 1985; Jenkins & Smith, 1969; Zauter et al., 1993). Due to the limited temperature range of occurence, DSA can cause inverse dependence of strength on temperature, i.e. strength increases with increasing temperature.

Dynamic strain ageing is related to interstitial atoms or interstitial atom-vacancy pairs at temperatures below 500°C and to substititional atoms at higher temperatures. It can be associated with pipe diffusion below 600°C and also with bulk diffusion above 800°C (Ilola, 1999).

1.13 Thermal fatigue

Cyclic thermal loads cause fatigue damage and crack growth. If the fatigue loading originates from cyclic pure thermal loads, i.e. thermal loads resulting from internal constraints, then loading is termed thermal fatigue loading. If the loads arise due to external constraints or forces, then the term thermomechanical fatigue is used. The loading is said to be in-phase when the highest temperature coincides with the highest stress and out-of-

phase when the highest temperature coincides with lowest stress (Figure 14).

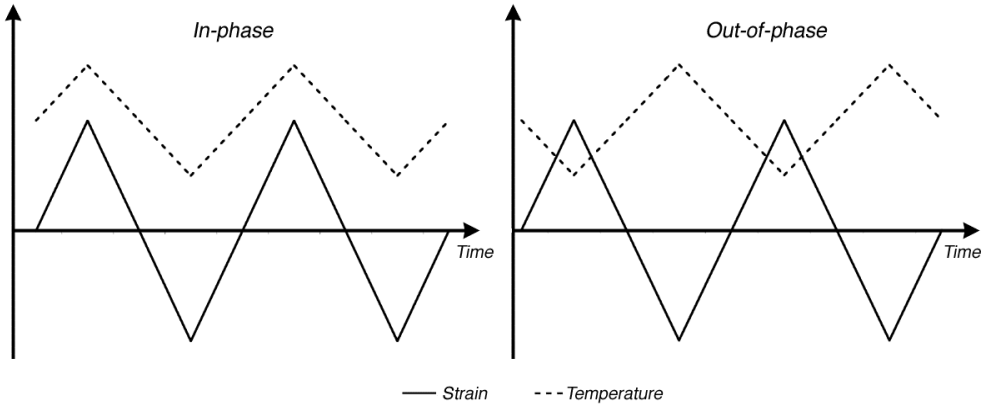

Figure 14. Schematic illustration of in-phase and out-of-phase loading.

Typically cyclic thermal loads arise from rapid heating or cooling of a component surface, e.g., due to turbulent mixing of fluids of different temperatures. It is characteristic to thermal loads that they are highest at the surface and attenuate towards the inside of the component. The loading is strain-controlled. Because the stresses are self-equilibrating, there exists a surface of zero stress in the component at any given time. This causes the characteristic $\Delta\varepsilon$ distribution, described schematically in Figure 15, to develop.

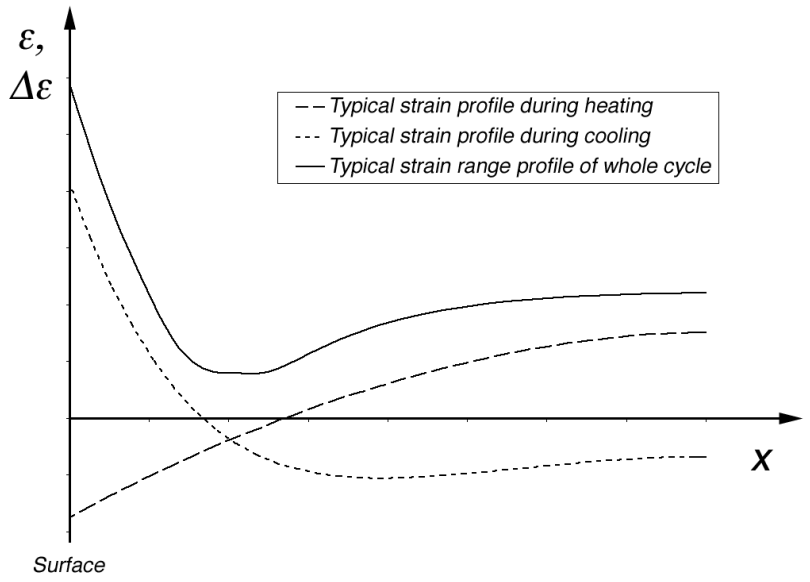

Figure 15. Typical distribution of $\Delta\varepsilon_\sigma$ as a function of depth (x) caused by thermal fatigue loading. At any given time the strain distribution shows a point of zero strain (the dashed lines). The corresponding $\Delta\varepsilon_\sigma$ distribution over the whole cycle shows a minimum at a certain distance (the solid line).

The strain range at the surface is often high and exceeds the yield strength of the material. Due to the equilibrating nature of the stresses, residual stresses arise as soon as plastic deformation takes place. Typically, the loading is applied to a surface equally in all directions, and the thermal strains are biaxial.

The characteristics of thermal fatigue loading are reflected in the characteristics of thermal fatigue cracking. The high strains at the surface give rise to rapid crack initiation on a multitude of initiation sites. Because of the biaxiality, cracks initiate and grow equally in all directions and soon form a mosaic-like network. The cracks relax the stresses perpendicular to the crack plane in their vicinity. Hence new cracks turn to meet older cracks at 90° angles. A typical thermal fatigue crack pattern is shown in Figure 16.

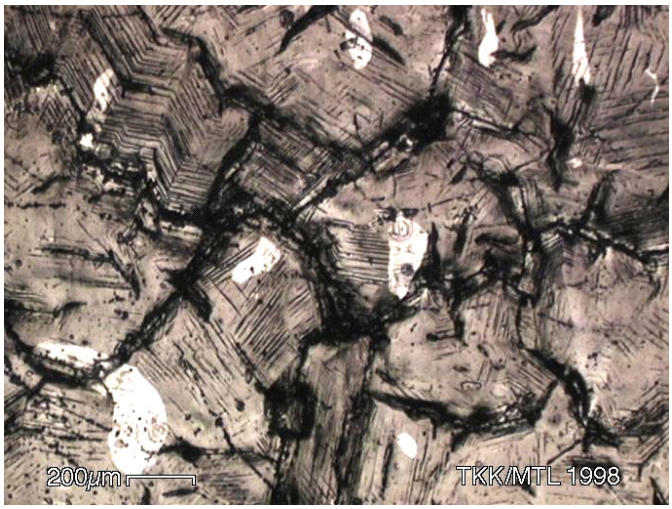

Figure 16. Typical mosaic-like crack pattern formed by thermal fatigue.

Due to the rapidly decaying $\Delta\varepsilon$ seen by a small surface crack, crack growth slows down after the initial rapid growth. Cracks typically slow down at some depth close to the minimum in $\Delta\varepsilon$. A smaller number of cracks extend over this minimum and continue to grow with an increasing rate.

Thermomechanical fatigue is closely related to thermal fatigue, although the characteristic features of the load pattern are lost in the case of external constraints or loads. More studies are available on thermomechanical fatigue than pure thermal fatigue probably due to easier comparison and integration to mechanical fatigue testing.

Thermal fatigue studies started, as did mechanical fatigue studies, with empirical tests aimed at providing a simulative verification of a design problem at hand (e.g., Coffin et al., 1954; Coffin & Schenectady, 1954; Tidball & Shrut, 1954). These kinds of studies have continued and S-N curves for different materials and environments have been measured (Hirano et al., 1994; Hayashi 1994; 1998a; 1998b; Hayashi et al., 1998).

Petersen & Rubiolo (1991) compared isothermal, thermal and thermo-mechanical fatigue data from different sources (Figure 17). The biaxial thermal fatigue data fits well with the uniaxial isothermal fatigue data, which lead Peterson & Rubiolo (1991) to conclude that the effect of biaxial stress condition on fatigue life is negligible. Also studies on multi-material components, such as coated composite tubes, have been made (e.g., Keiser et al., 1996; 1997; Revel et al., 2000; Saarinen et al., 2000), and thermal fatigue caused by a traveling temperature distribution has been investigated (Ogawa et al., 1991; Igari et al., 2000).

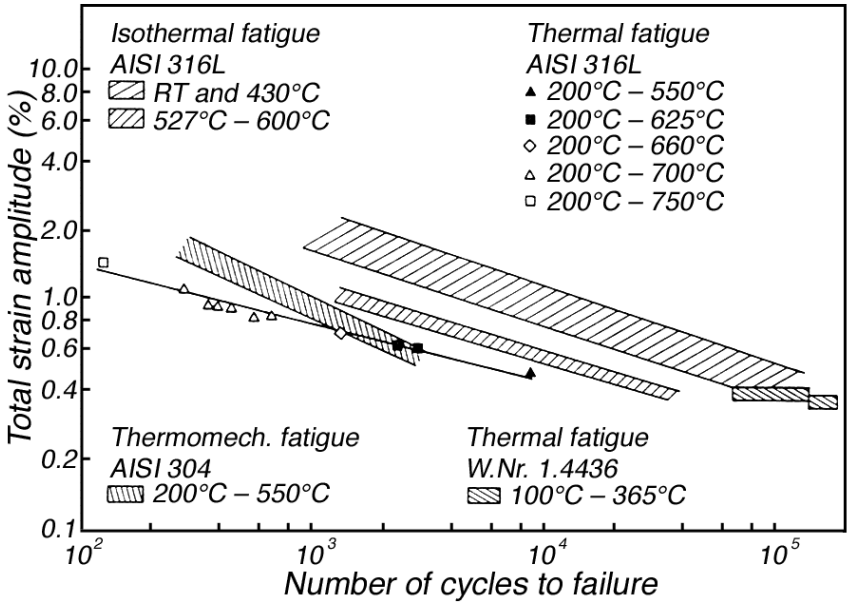

Figure 17. Fatigue data for isothermal, thermal and thermo-mechanical fatigue in air at different temperatures (after Petersen & Rubiolo, 1991)

The established design methods for mechanical fatigue were soon applied to thermal fatigue. Wareing et al. (1973) studied the effects of temperature and strain rate on the fatigue behavior of two austenitic stainless steels and concluded that the difference in fatigue behavior was explained by the effect of temperature and strain rate on cyclic behavior. Models have been proposed to predict the cyclic stress-strain curves in the case of thermomechanical loading based on isothermal data (Shi & Pluvinage, 1994; Maier & Christ, 1996; 1997). The stress-strain behavior in thermomechanical fatigue saturates after fewer cycles than in mechanical fatigue (Spindler, 1998).

Zauter et al. (1994) were among the first to study dislocation arrangements caused by the thermomechanical fatigue of AISI 304L. They found cell structures at lower temperatures (below 625°C), where creep was not significant. Above 625°C transition into directional sub-grain structure was observed. This transition was attributed to creep. Maier & Christ (1997) found that under thermomechanical fatigue conditions cell structures form. Armas et al. (1992) studied AISI 316 type steel with

thermal expansion fully restricted by external constraints. Walls-channels and cell structures were observed similar to those seen in isothermal loading.

Studies on dislocation structures caused by pure thermal fatigue are rare to find. Recently Keiser et al. (1996; 1997) observed low dislocation density and dislocation tangles when studying possible thermal fatigue of recovery boiler tubes. Recent studies by Saarinen et al. (2000) on thermal fatigue of recovery boiler tubes confirm these results.

Taira (1973) studied the difference between thermal fatigue and high temperature isothermal fatigue. He proposed that a Coffin-Manson curve for thermal fatigue could be determined by simpler isothermal tests if the temperature for the test was chosen correctly. He found that at low temperatures (below 400°C for the 0.16% carbon steel he studied) this equivalent temperature (T_e) was equal to the arithmetic mean of the T_{max} and T_{min}. In this temperature regime the diffusion-controlled effects are negligible and thermal and mechanical fatigue are expected to be similar (Taira, 1973). At higher temperatures, the damage accumulated close to the maximum temperature dominates and $T_e \approx T_{max}$. Crack growth studies on thermal and thermomechanical fatigue are rare. Notable exceptions are the measurements by Shi et al. (1996) presented in Figure 18, and Marsh (1981), presented in Figure 19.

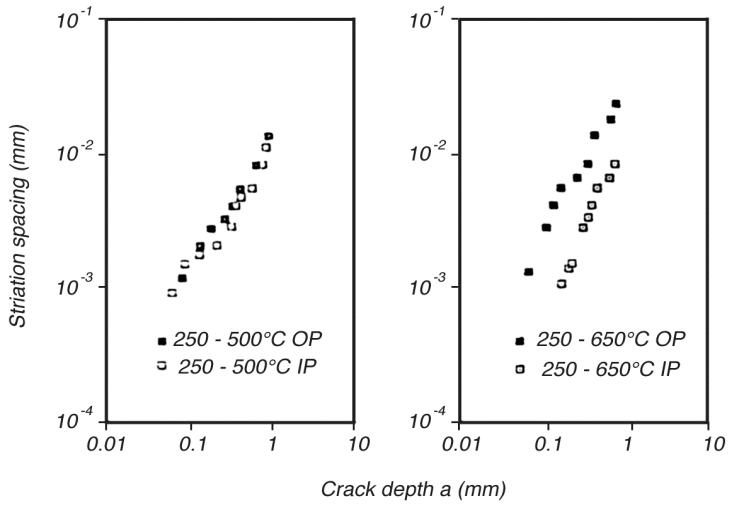

Figure 18. Striation spacing measured from thermomechanical fatigue fracture surface of AISI 316L austenitic stainless steel with in-phase (IP) and out-of-phase (OP) loading of two different temperature regimes with total strain range of 1.6% (after Shi et al., 1996).

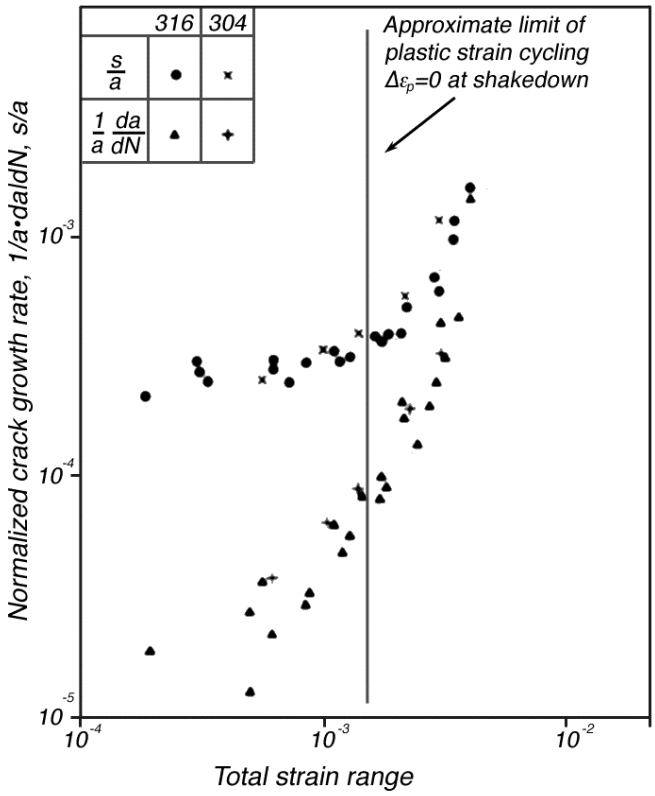

Figure 19. Crack growth rate of AISI 304 and 316 austenitic stainless steels subjected to thermal fatigue loading of effective ΔT of 208 – 288°C. Loading was applied with cyclic resistance heating and water quenching. (After Marsh, 1981)

The design codes developed for mechanical fatigue, such as the ASME Boiler and Pressure Vessel code (1995), are currently used to design against thermal fatigue although experimental verification of their applicability is limited (Merola, 1995; Fissolo et al., 1996; Kerezsi et al., 2000). The K- or J-solutions for cracks growing in thermal or residual stress fields have been studied, e.g., by Hirano et al., (1979); Zhang & Burger (1986); Kuo & John, (1992); John et al. (1992); Jin & Noda (1994); Fischer et al. (1996) and Tanigawa & Komatsubara (1997). The K-solutions are limited to small ΔT due to the small scale yielding condition of LEFM. The crack growth models for mechanical fatigue have been applied to thermal fatigue in several studies. The used models include the Paris law (dell'Erba & Aliabadi, 2000; Marsh et al., 1986; Green et al., 1987; Bressers et al., 1994), strain-based models (Tomkins, 1983b; Green & Munz, 1996) or both (Marsh, 1981). In many cases, the complexity of the thermal fatigue loading imposed serious restrictions or approximations on the analysis. The Haigh-Skelton model (equation 27) was recently applied to thermal fatigue crack growth analysis by Green & Munz (1996). The results were promising, although the thermal stress analysis was limited and the actual crack growth rates could not be measured or compared to calculations.

Marsh (1981) studied the thermal fatigue behavior of AISI 304 and 316 steels. He concluded that the thermal fatigue initiation life correlated with the initiation life observed in uniaxial isothermal fatigue if the biaxial thermal fatigue data was converted to an equivalent uniaxial load case with equations 36 and 37 (Figure 20).

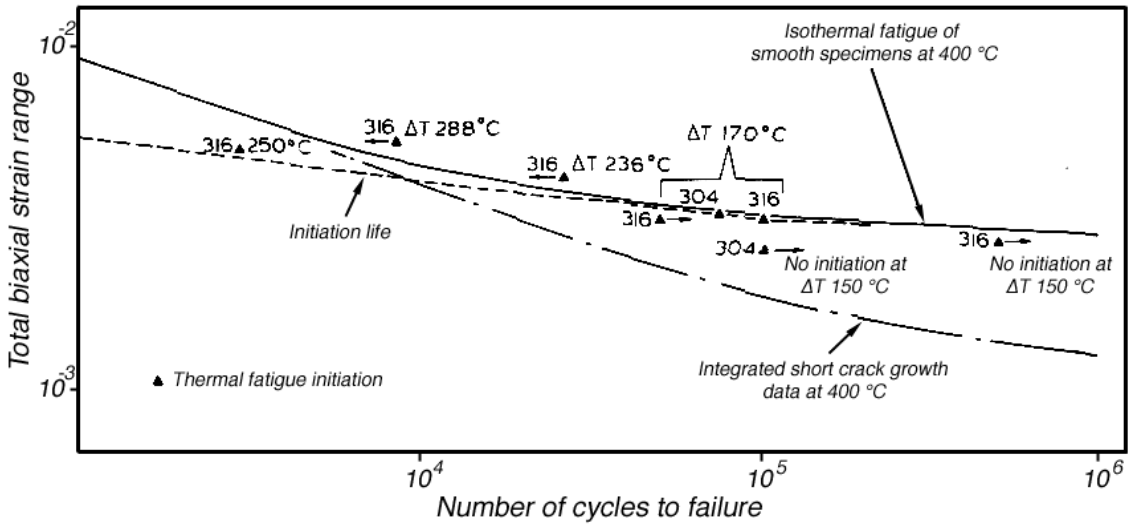

Figure 20. Comparison of initiation life of thermal and isothermal fatigue (after Marsh, 1981).

Marsh (1981) obtained good correlation between the thermal and isothermal fatigue crack growth rates by describing the crack growth in the highly strained near surface area with a strain-based model (equation 40) and the crack growth in the elastic bulk with the conventional Paris law (equation 14):

$$\frac{da}{dN} = a\left(\frac{\pi^2}{8}\left(\frac{\sigma}{2\sigma_f}\right)^2 \frac{\Delta\varepsilon_p}{1+2s_2}\right), \tag{40}$$

where σ is the maximum tensile stress in the cycle,

σ_f is the flow stress,

s_2 is the work hardening exponent and

$\Delta\varepsilon_p$ is the plastic strain range.

2 AIMS OF THE CURRENT WORK

The tools for fatigue design offered in the present open literature can be divided into three categories: phenomenological models (1), crack growth models based on fracture mechanics (2), and crack growth models not based on fracture mechanics (3). In thermal fatigue, the loading typically causes a varying strain and temperature field in the affected component, as presented in Figure 15. This makes the application of the phenomenological models to the thermal fatigue load case difficult, since a single representative load parameter is not readily available.

The application of LEFM-based crack growth models is limited by the small scale yielding condition. This prohibits the use of LEFM-based models for small cracks and high loads. The EPFM parameters are valid for greater amounts of plastic deformation, but are difficult to determine for a crack advancing in a varying strain and temperature field. Consequently, the usefulness of EPFM-based models is limited by the reliability and feasibility of the stress analysis required.

For the crack growth models not based on the fracture mechanics, such as the strain-based models, the main problem is that their range of applicability is unknown. Numerous crack growth parameters have been proposed in the open literature, but for each parameter the applicability is demonstrated for a rather limited range of materials and load cases. Applicability of these models to cracks growing in varying strain and temperature fields caused by cyclic thermal loads is unclear.

The existing tools for fatigue design are, thus, seen to be inadequate for predicting fatigue damage and crack growth in the thermal fatigue load cases. The aim of the present work is to study the micromechanisms of thermal fatigue crack growth in austenitic and duplex stainless steels, to study the loads and residual stresses caused by cyclic temperature changes, and finally, to find a crack growth model applicable to small thermal fatigue cracks.

3 EXPERIMENTAL PROCEDURE

Thermal fatigue test samples were subjected to controlled thermal loads. The thermal loads used were selected to be similar to those found in actual industry applications. Applied thermal loads were characterized by thermal load measurements and numerical calculations. The evolution of thermal fatigue damage in the samples was monitored by periodic residual stress measurements and replica-assisted microscopy. To aid the numerical calculations and to compare thermal fatigue and high temperature mechanical fatigue, cyclic stress-strain curve measurements were conducted on some of the materials. Finally, a destructive analysis including fractographic scanning electron microscopy (SEM) studies and transmission electron microscopy (TEM) analyses was performed on the fatigued samples.

3.1 Materials

Altogether 9 different materials or thermal treatments were studied. Three test materials common in nuclear power plants were chosen for testing: AISI 304L, 316 and 321. AISI 321 and AISI 347 were studied in solution annealed and stabilized conditions, as used in the oil refinery industry. (Stabilization heat treatment is used in the oil refinery industry to prevent sensitization at the high working temperature. The used materials were held at 920 °C for 2 h and then cooled in air.) Two duplex stainless steels used in pulp & paper industry were chosen: ACX-100 – a cast duplex stainless steel made by Kubota and 3RE60 – a wrought duplex stainless steel manufactured by Avesta. The chemical compositions and the material codes (used hereafter to identify the materials) of test materials are shown in Table 3. Available mechanical properties of the test materials are shown in Table 4. The test materials were characterized by standard metallographic analyses.

Table 3. Chemical compositions of the materials studied.

Material code	Type	Cr	Ni	Mo	Mn	Si	Other
A	AISI 304L	17.4	10.2		1.6	0.8	
B	AISI 316	17.9	12.7	2.7	1.33	0.3	
C	AISI 321	17.8	10.7	0.4	1.6	0.3	0.1 Cu, 0.5 Ti, 0.2 Co
D	AISI 321	19.6	10.0		0.9	0.7	0.4 Ti
E	AISI 321	"	"	"	"	"	"
F	AISI 347	17.3	9.2	0.4	1.5	0.4	0.4 Cu, 0.5 Cb, 0.1 Co
G	AISI 347	"	"	"	"	"	"
H	3RE60	18.5	4.9	2.9	1.5	1.5	0.1 N
I	ACX-100	23.4	5.3	2.2	0.6	0.6	0.2 N

Table 4. Room temperature mechanical and physical properties of the materials studied. (Properties reported based on manufacturers information or minimum required standard values for similar grades (Wegst, 1995)).

Material code	Type	$R_{P0.2}$ MPa	R_m MPa	E GPa	k W/mK	α $x10^{-6}$ K^{-1}	
A	AISI 304L	180	460	200	15	16,0	Solution annealed
B	AISI 316	205	510	200	15	16,5	Solution annealed
C	AISI 321	180	460	205	15	16,0	Solution annealed
D	AISI 321	205	500	200	15	16,0	Solution annealed
E	AISI 321	205	500	200	15	16,0	Stabilized
F	AISI 347	205	510	200	15	16,0	Solution annealed
G	AISI 347	205	510	200	15	16,0	Stabilized
H	3RE60	450	730	200	15	14	42% ferrite
I	ACX-100	460	660	200	15	13	56% ferrite

The microstructures of the studied materials were examined in three different orientations. In Figures 21 – 24 the microstructures of the studied materials are shown.

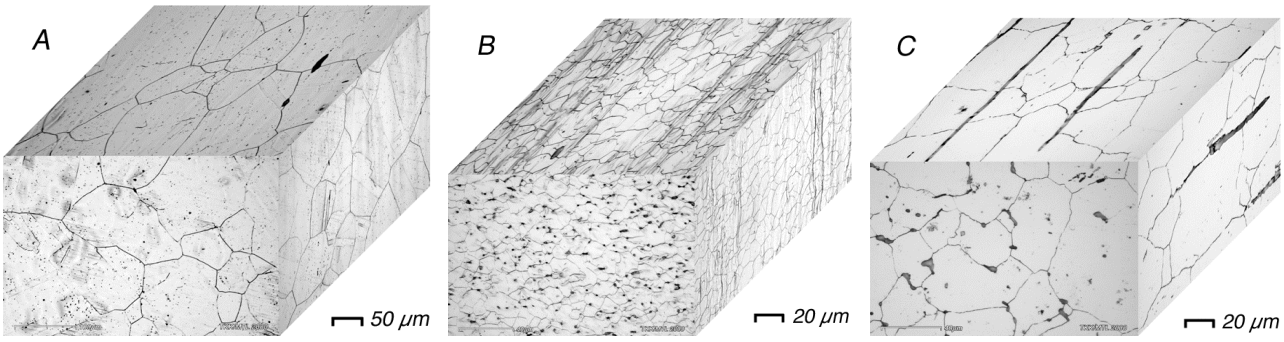

Figure 21. Microstructures of studied A, B and C materials.

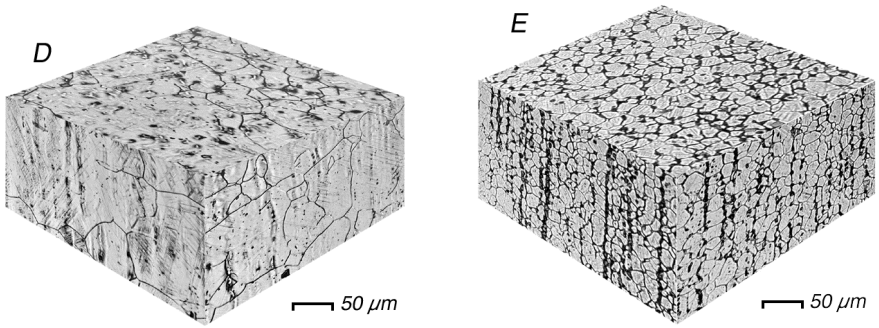

Figure 22. Microstructures of studied D and E materials. The stabilization treatment has refined the grain size considerably and caused an increase in the ferrite content (material E).

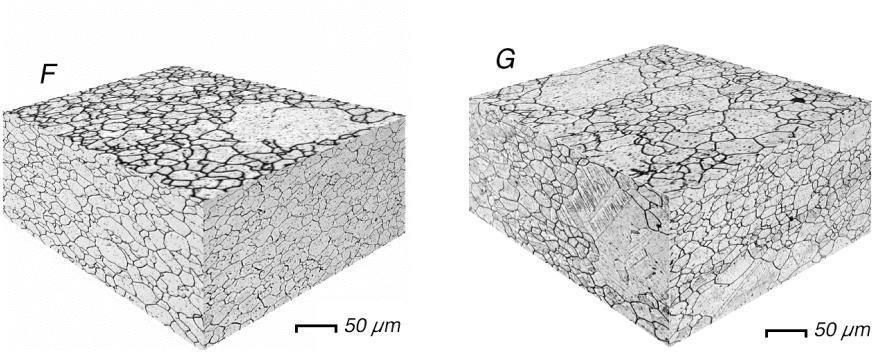

Figure 23. Microstructure of studied F and G materials. The stabilization treatment has left the microstructure virtually unchanged (material G).

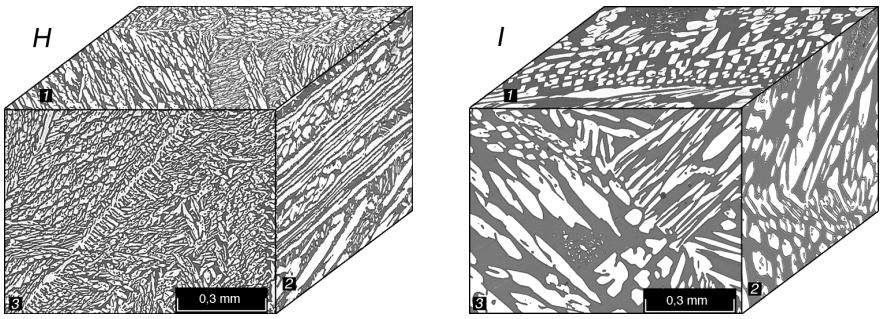

Figure 24. Microstructure of studied H and I materials. The H material shows anisotropic phase structure due to rolling. The cast I material has considerably coarser, but isotropic, phase structure. Samples were manufactured so that the axial direction of the sample is perpendicular to face 3.

3.2 Thermal fatigue tests

Thermal loads were applied using a prototype thermal fatigue testing machine built in the Laboratory of Engineering Materials (Kemppainen, 1997). Two kinds of test specimens were used (Figure 25).

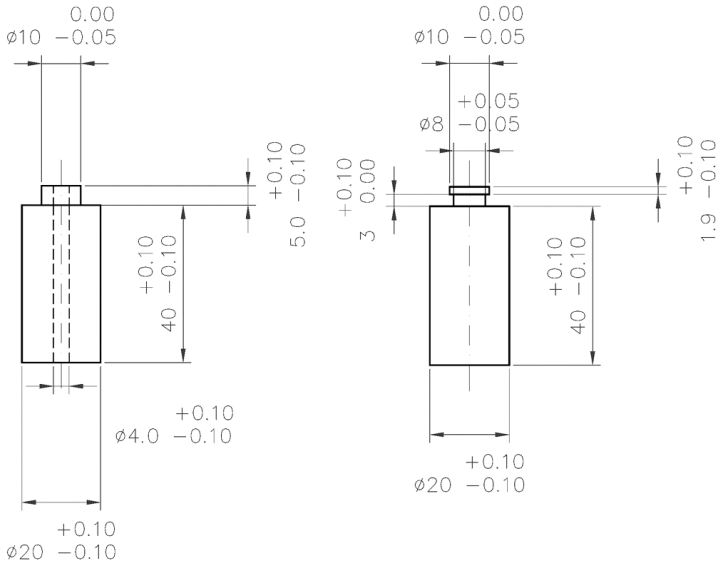

Figure 25. Specimen geometries used. (Dimensions in mm.)

Specimens were heated rapidly by 156 kHz high frequency induction and cooled by water spray. The test apparatus (Figure 26) consisted of an induction heating unit, a cooling ring and a pneumatic positioning system that moved the specimen between heating and cooling. Specimens were rotated to achieve uniform heating and cooling.

Figure 26. Thermal fatigue test apparatus.

Rapid heating and cooling caused a steep, cyclic temperature gradient in the specimen. Uneven temperature distribution in the radial direction constrained the thermal expansion of the sample and gave rise to thermal loads. A more detailed description and verification of the test apparatus is given by Kemppainen (1997).

The thermal cycles were chosen to simulate the thermal loads expected in actual industrial components. For the nuclear industry materials (codes A, B and C) the maximum expected temperature in use was about 300°C. A temperature cycle of 20 – 300°C was chosen. For the oil refinery industry materials (codes D, E, F and G) a higher temperature cycle of 20 – 600°C was utilized. For the pulp & paper industry materials (codes H and I) a temperature cycle of 20 – 280°C was chosen. The temperature cycles used, as measured at the sample surface, are presented in Figure 27. (The mentioned temperature ranges are used hereafter to identify the cycles, although some deviation is present in the actual cycles, as can be seen from Figure 27.)

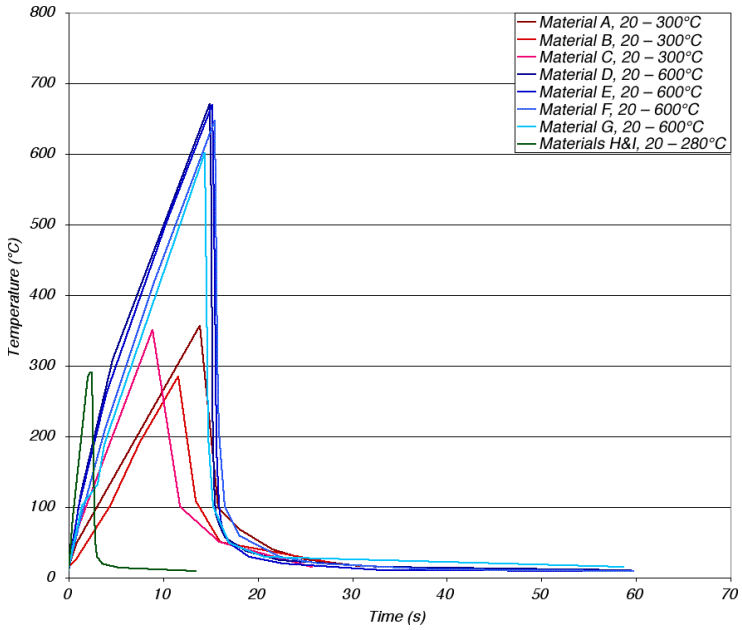

Figure 27. The temperature cycles used. Temperature cycles were measured at the sample surface using a thermocouple.

Thermal cycling was stopped at predefined intervals, and the residual stresses on the sample surface were measured with X-ray diffraction. Measurements were conducted with a Stresstech X3000 commercially available residual stress measurement unit using Cr-Kα radiation. Residual stresses were calculated using the $\sin^2\Psi$ -method (Cullity, 1978). The surface of the sample was replicated with cellulose acetate. With successive replicas taken from the sample surface, it was possible to monitor the initiation and growth of individual thermal fatigue cracks.

Finally, a destructive examination was conducted on the samples. The samples were cut and studied with optical and SE-microscopy to reveal the

radial crack growth. When possible, one of the cracks in the sample was opened in liquid nitrogen and the fracture surface was studied with SEM. A TEM study of the fatigued material was also conducted. TEM samples were taken from a depth of about 2 mm. At this depth the calculated $\Delta\varepsilon$ was much lower than at the surface (see Figures 39 and 40).

3.3 Thermal load determination

Thermal loads resulting from the applied thermal loading were determined at the sample surface. For the determination, a sample was instrumented with an air-cooled high temperature strain gage and thermocouples. The instrumented sample was then subjected to thermal cycling in the temperature range of interest. During the thermal cycling, the axial thermal expansion and the temperature of the specimen surface were measured. When the temperature of the sample is known, the expected thermal expansion can be calculated from equation 1. By comparing the expected thermal expansion to the actual measured thermal expansion, the constrained expansion can be calculated taking into account that at the surface the radial stresses are zero and the axial and tangential strains are equal (equation 41, see Appendix 2 for derivation).

$$\varepsilon_\sigma = \frac{\varepsilon_m - \varepsilon_T}{1-\nu}, \tag{41}$$

where ε_σ is the constrained strain that causes stresses,
ε_T is the calculated thermal expansion and
ε_m is the strain measured from the sample surface.

In the linear elastic region, the resultant thermal stresses can be calculated from the Hooke's law (Boley & Weiner, 1960):

$$\sigma_a = \frac{E\nu(\varepsilon_a + \varepsilon_t + \varepsilon_r)}{(1+\nu)(1-2\nu)} + \frac{E\varepsilon_a}{1+\nu}, \tag{42}$$

where the subscripts a, t and r denote axial, tangential and radial stresses, respectively.

3.4 Residual stress profile measurements by contour method

To find out the residual stresses inside the sample, the destructive contour method was used. This method was recently introduced by Prime & Gonzales (2000) and it is not a standardized method for residual stress measurements. The method is based on measuring displacement caused by relaxation of residual stresses on a cut surface. As with all relaxation techniques for residual stress measurement, the method assumes, that the relaxation of residual stresses occurs elastically and that the cutting does not induce stresses. In addition, because the displacements are measured directly from the cut surface, in the contour method it is assumed, that the cut occurs along a plane that was flat when the cutting started. This

assumption requires, that the sample is constrained from both sides, when the cut is made. The main error sources for this method are inadequate constraint during cutting and the stresses caused by the cutting (Prime, 2001).

For a small cylindrical sample, conventional methods such as the hole drilling or the crack compliance methods are not usable. The neutron diffraction method has a spatial resolution of about 1 mm, which is not sufficient to capture the residual stress profile resulting from thermal loads. Hence, the contour method is the only feasible way of measuring the residual stresses inside the samples. For the measurement, a sample was subjected to 10 thermal cycles of interest. 10 cycles were chosen to ensure that a stabilized residual stress configuration was reached, but without crack formation altering the residual stresses.

Samples were cut in two by electric discharge machining (EDM), and the shape of the cut surface was measured with an inductive surface finish and form measurement unit (Taylor Hobson Form Talysurf Series 2). Deviations from planeness develop due to relaxation of residual stresses perpendicular to the cut surface. The measured deviations were then inserted into a linear-elastic FE-model, and the pre-cut residual stresses were solved as proposed by Prime & Gonzales (2000) and Prime (2001). The FE-analysis was conducted with a commercially available ANSYS FE-code (ANSYS, release 5.5.1, 1998). An axisymmetric model was used.

3.5 Cyclic stress-strain tests

In order to study the cyclic behavior of the test materials as well as to obtain needed material data for the numerical simulations, cyclic stress-strain measurements were conducted on F, G, H and I materials. Measurements were conducted in strain-control with repeating load blocks containing varying amplitudes (Figure 28). The specimen geometry is presented in Figure 29. Cyclic stress-strain curves were determined at room temperature (materials F, G, H and I) and at 100, 200, 300, 400, 500 and 600°C (materials F and G).

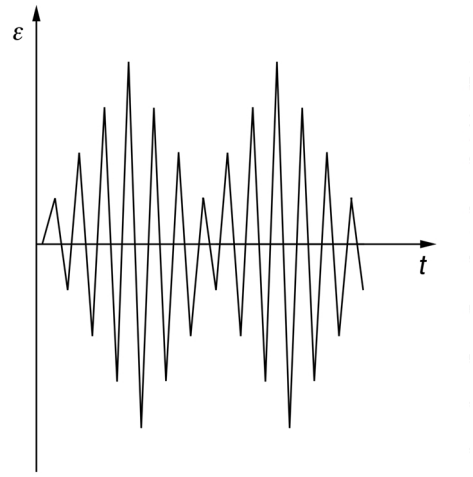

Figure 28. Schematic image of the loading pattern used in the cyclic stress-strain curve measurements for materials F and G. For materials H and I the load pattern is similar but with ε_{min}=0.

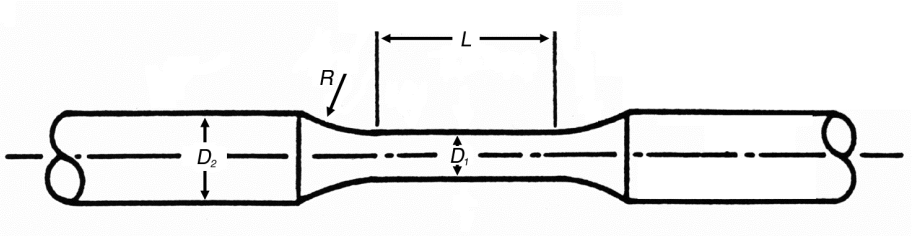

Figure 29. The specimen geometry used for cyclic stress-strain measurements. The dimensions are as follows: L=30 mm, D_1=7.5 mm, D_2=15 mm, R=75 mm.

In the tests made with duplex stainless steels (materials H and I) at room temperature, Barkhausen noise was measured. The Barkhausen noise signal originates from the turning of the magnetic domains in ferromagnetic materials. Consequently, in duplex stainless steels the signal comes from the ferrite phase alone. Using the Barkhausen noise data, it was possible to measure the load carried by the ferrite phase. However, the local phase stresses depend on the microstucture, i.e. phase morphology, and the austenite phase stresses cannot be resolved.

Previously the load sharing between austenite and ferrite phases has been measured using in-situ X-ray diffraction measurements during tensile testing (Johanson & Odén, 2000a; 2000b; Inal et al., 1999). This is very laborious and time consuming: a single X-ray measurement can take hours to complete. Measurement of repeated cycles is therefore not practical.

The Barkhausen noise signal is very sensitive to the magnetic properties of the material, i.e., to the ferrite content of a duplex stainless steel. As the ferrite content varies markedly even within a single sample, each time the Barkhausen sensor was attached to a specimen, a new calibration had to be made. In practice this meant that, before each test the sensor was firmly attached to the sample, and the small, elastic cycles in

the beginning of the test were then used for calibration. It was assumed that no microscopic residual stresses exist at the beginning of the test. The Barkhausen noise signal is primarily dependent upon the elastic strain (Stefanita et al., 2000). However, the measurement is also sensitive to hardness, microstructure and prior plastic deformation (Lindgren & Lepistö, 2000a; 2000b).

3.6 Numerical simulations

The test sample (Figure 25) was modeled with an axisymmetric, infinite height model (see Appendix 3 for description of the used models). An uncoupled analysis was conducted with 8 node rectangular elements. In thermal analysis, the temperature cycles measured in the thermal load measurements were used as loading. The outer surface of the model was forced to follow the measured temperature cycle. The temperature cycle was divided to about 30 steps, and linear temperature solution was used to solve each step.

Solved temperature distributions were then read to the mechanical solution as load steps. A non-linear structural analysis was conducted for the F material for which the cyclic stress-strain curves had been measured. A hybrid multilinear isotropic-kinematic material model was used, and the resulting cycle stabilized within 3 cycles. In addition, all materials and used cycles were analyzed with a linear elastic structural analysis.

In the strain-controlled thermal loading, the linear-elastic and elastic-plastic total strain solutions give very similar results. In fact, in many geometries, such as the infinite axisymmetric model considered here, the total strain solution of pure thermal loading is independent of the value of E. Consequently, in the uniaxial case the strain field is not affected by plastic deformation, and a linear model can correctly solve the total strain. In a multiaxial case, the resulting strain field depends also on the effective Poisson's ratio ν_{eff}, which changes from elastic value of ν to the plastic value of 0.5 with increasing amount of plastic deformation. This induces some error in the solved strain field in the multiaxial case. If the thermal strains change the residual stresses of the material, the initial strain field is changed for the next load cycle. For cyclic loading the developing residual stresses cause additional error. This affects mainly the mean strain during a cycle and not so much the total strain range solved.

Consequently the total strain ranges solved from the elastic and elastic-plastic analyses are very similar, even in the 20 – 600°C temperature cycle where high plastic strains were calculated (Figure 30). The elastic-plastic analysis gives additional information about the stresses and the amount of plastic strain, which cannot be modeled by the elastic analysis. The elastic-plastic solution also gives predictions about the residual stresses caused by

the cycle. The FE-analysis was conducted with a commercially available ANSYS 5.5 FE-code (ANSYS Release 5.5.1, 1998).

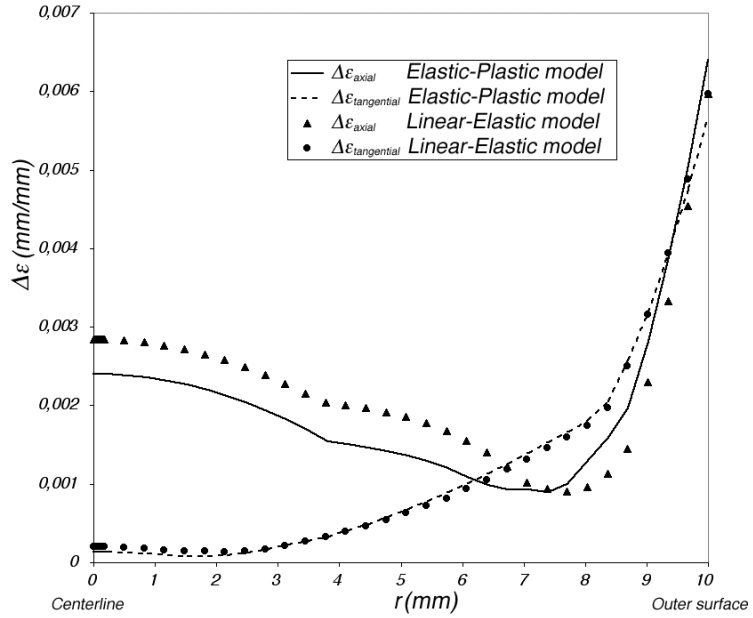

Figure 30. Comparison of the Δε distributions solved from elastic-plastic (solid and dashed lines) and linear elastic (dots) models. Dimensions in (mm).

4 RESULTS

The yield behavior of the studied materials was examined with cyclic stress-strain measurements (materials F and G) and Barkhausen noise measurements (materials H and I). The strains caused by the applied thermal load cycles were characterized with strain measurements on the surface and with numerical modeling. The damage caused by the thermal cycling was studied using replica-assisted microscopy, fracture surface studies (SEM) and dislocation structure analysis (TEM).

4.1 Cyclic stress-strain curves

Cyclic stress-strain curves were measured for the solution annealed material F and stabilized material G. Material F showed higher strength than material G during the first load block. Subsequent 10 load blocks caused cyclic softening in material F. Material G showed slight cyclic hardening during the first load blocks and subsequent small cyclic softening. The difference in the cyclic stress-strain behavior decreases the difference of strength between the different heat treatments. The behavior during the 10 first load blocks at room temperature is shown in Figure 31. The stabilized curves at different temperatures are shown in Figure 32.

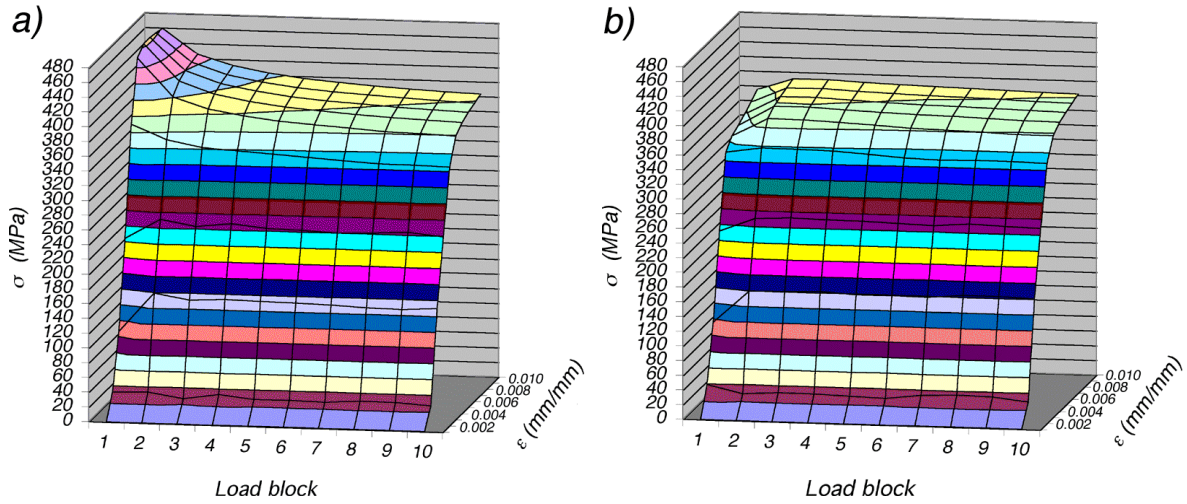

Figure 31. Measured stresses during the first 10 load blocks measured at room temperature for materials F (a) and G (b). Material F shows cyclic softening after the first load block. Material G shows initial cyclic hardening followed by cyclic softening.

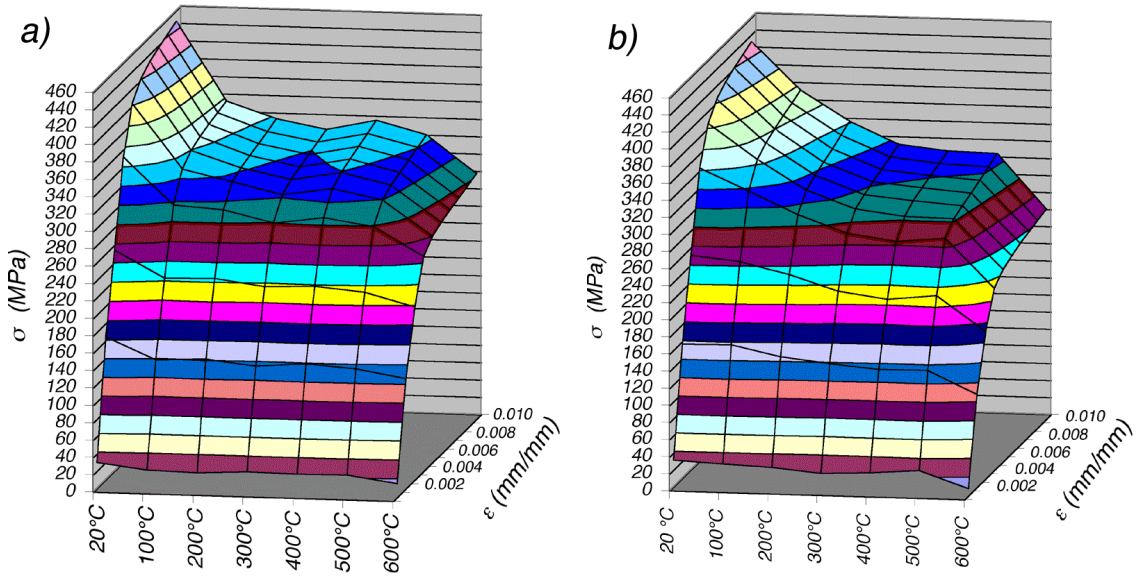

Figure 32. Stabilized stress-strain curves measured for materials F and G at different temperatures. Stabilized curves were taken after about 80 load blocks. For material F the cyclic stress-strain curve at 400°C indicates higher strength than at 200°C and 300°C. This hardening can be attributed to dynamic strain ageing.

The strength of the materials decreases with increasing temperature. However, for the solution annealed material F the strength at 400°C is higher than at 200°C or 300°C. This effect was not observed in the stabilized material G. The strengthening can be attributed to dynamic strain ageing (DSA). DSA is observed in austenitic stainless steels in the temperature range of 250 – 600°C, depending upon the strain rate (Ilola, 1999; Zauter et al., 1993). Evidently the stabilization heat treatment has decreased the amount of free interstitial solute atoms. Consequently DSA is not observed in material G.

The measured isothermal stress-strain curves can be considered representative or conservative as compared to thermomechanical curves (Spindler, 1998; Mallet et al., 1995; Skelton & Webster, 1996).

4.2 Barkhausen noise measurements

With Barkhausen noise measurements it was possible to measure the elastic strains of the ferrite phase and the load sharing between the austenite and ferrite phases in duplex stainless steel (materials H and I) during cyclic loading. At small strain amplitudes the load in ferrite is linearly proportional to the macroscopic elastic strain. With increasing load uneven plastic deformation gives rise to interphase residual stresses. The residual stresses form during the first several load-blocks and then stabilize. The effect of residual stresses is that the load sharing between the phases is equalized.

The greater yielding in tension in the austenite phase results in tensile residual stress in the ferrite phase, as expected. In material I the microstructure is anisotropic and the phases impose little constraint on each other. At small load amplitudes, both phases deform elastically. However, when the load amplitude increases, the austenite phase starts to yield. This causes the load raise in ferrite to slow down, and tensile residual stress to develop in ferrite. As the load amplitude increases, austenite hardens, and greater residual stresses develop (Figure 33). After about 5 load blocks a saturated state is achieved (Figure 34).

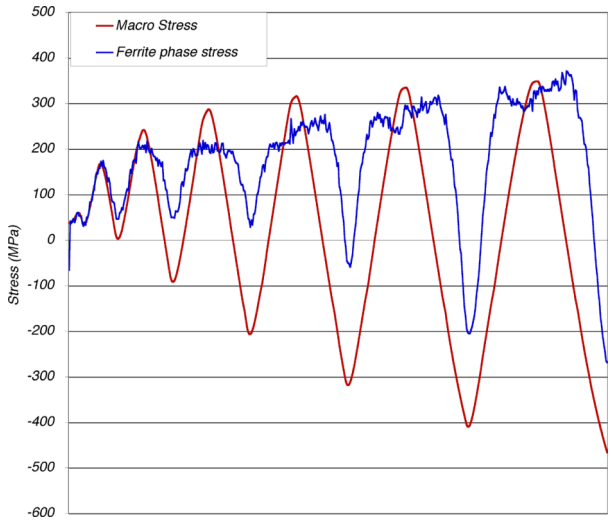

Figure 33. The macroscopic stress and phase stresses during first load cycles in material I. Sample was strained as shown in Figure 28 at room temperature.

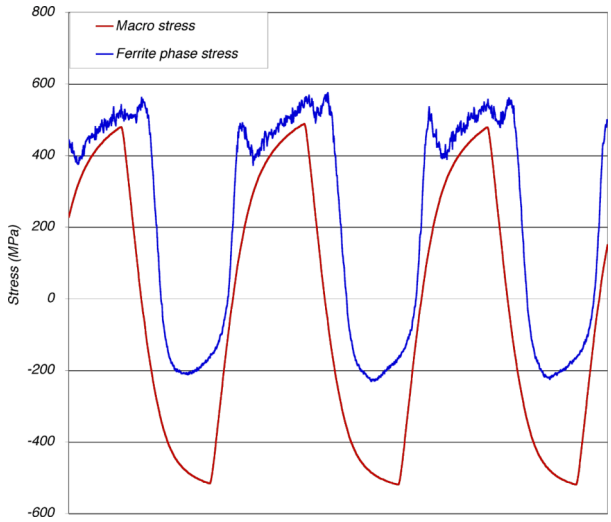

Figure 34. After about 5 load blocks a saturated state is achieved. The macroscopic stress and phase stresses of a few cycles from a stabilized load block are presented for material I. Sample strained at room temperature.

In material H the elongated microstructure imposed greater constraint to the phase deformation. During the first load block the behavior is

similar to that of material I (Figures 33 and 34). However, with larger stress amplitude the phase stresses cannot develop freely, and the stress in the ferrite increases even though the austenite deforms plastically. The resulting stress cycle is presented in Figure 35.

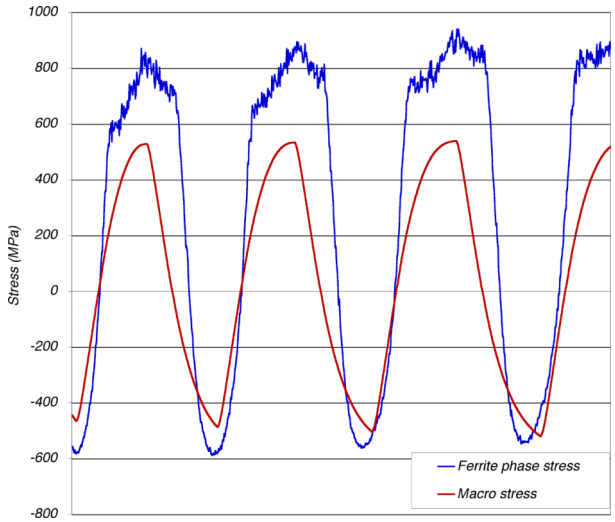

Figure 35. After about 5 load blocks a saturated load block is achieved. The macroscopic stress and phase stresses of a few cycles from a stabilized load block are presented for material H. Sample strained at room temperature

4.3 Cyclic strain caused by thermal loading

The axial strains applied to the sample surface could be determined from the measurement. The numerical analysis gave information about the strains inside the specimen. In the austenitic materials (materials A – G) the largest strains were observed in the beginning of the cooling phase, where the temperature change is very quick. In the duplex materials (H and I), where greater heating power was used, the temperature change and, thus, the thermal strains were highest during the heating phase.

The applied axial strains were determined at the sample surface. Figure 36 shows a strain plot where the temperature range was increased after each cycle in the austenitic material G. The largest compressive strain depends mainly on the heating power, which was kept constant during the cycles. The largest tensile strain depends mainly on the cooling power, i.e. the temperature difference between the sample and the cooling medium. Hence, the increase in the temperature range increases the largest tensile strain. The strains determined from all the samples are presented in Table 5.

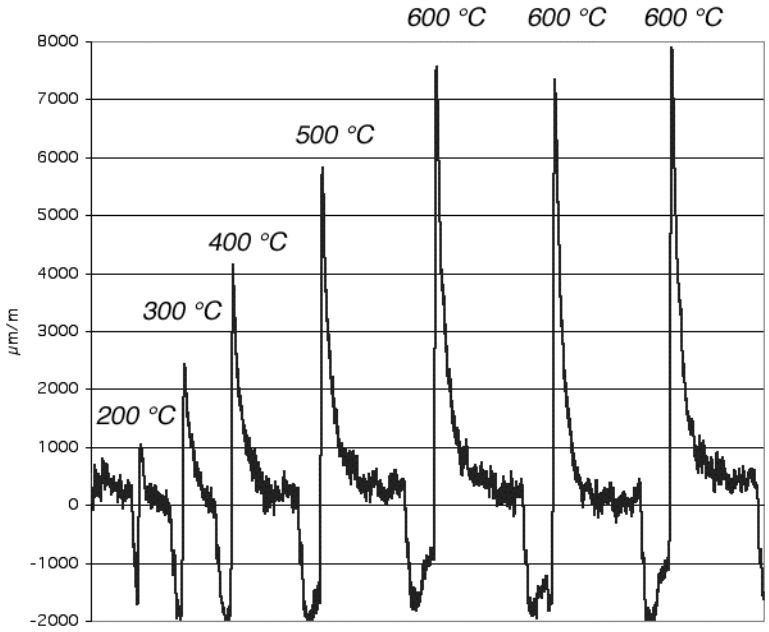

Figure 36. Constrained thermal strain plot from material G. During the first 5 cycles the temperature range was increased by 100°C after each cycle by increasing the heating time. Temperature cycles of 20 – 200°C, 20 – 300°C, 20 – 400°C, 20 – 500°C and 20 – 600°C were applied. The temperature cycling was then continued at 20 – 600°C.

Table 5. Thermal strain measurements. The applied strains were calculated from the measured temperature and strain using equation 41.

Material	Thermal cycle (approximate)	Minimum thermal strain (µm/m)	Maximum thermal strain (µm/m)	Thermal strain amplitude (µm/m)
A	20 – 300°C	-2000	4400	3200
B	20 – 300°C	-2000	800	1400
C	20 – 300°C	-2000	2000	2000
D	20 – 600°C	-1300	6800	4050
E	20 – 600°C	-1000	7500	4250
F	20 – 600°C	-1700	6700	4200
G	20 – 600°C	-1600	6700	4150
H	20 – 280°C	-2460	850	1660
I	20 – 280°C	-2340	1050	1700

The monotonic yield strain of the studied austenitic stainless steels (materials A – G) is about 1000 µm/m. The determined strain amplitudes exceed the yield strain, and the cycles give rise to plastic deformation both in tension and compression during each cycle. The duplex stainless steels are considerably harder: their yield strain is about 2000 µm/m. The yield

strain is exceeded in compression but not cyclically, during every cycle, as the strain amplitude is below this value.

Thermal strains were calculated with the finite element method (FEM) from the temperature curves measured on the sample surface. A typical time-varying temperature solution is presented in Figure 37. The corresponding strain solution is presented in Figure 38. The $\Delta\varepsilon$ distributions calculated from the linear elastic FE-analysis are shown in Figures 39 and 40. The axial strain distribution shows a minimum at about 2.5 mm for all temperature cycles. For the tangential strain solution the minimum is deeper - at about 5 mm. Consequently, the loading is equi-biaxial at the surface, but the tangential strains dominate at a depth of about 2.5 mm. Axial strains then increases again, and finally at depths greater than about 4 mm the axial strains dominate.

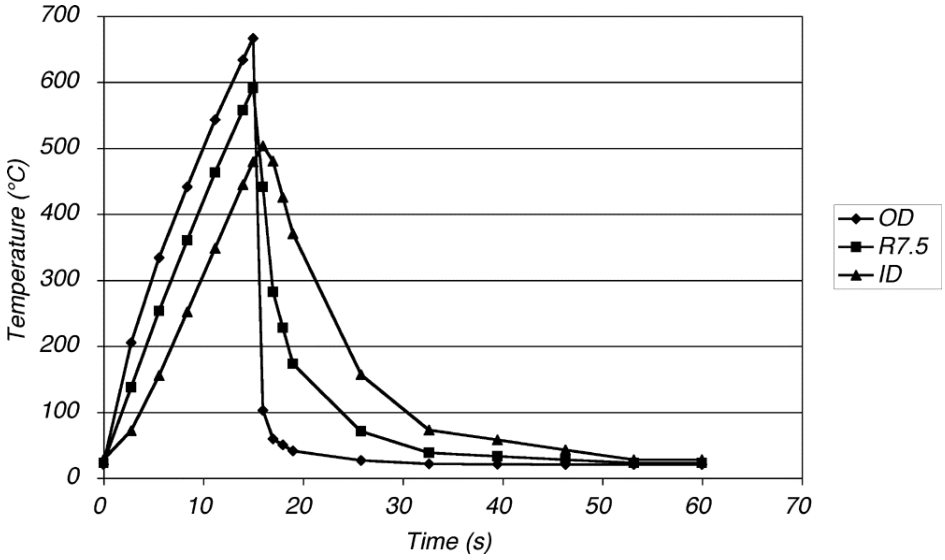

Figure 37. A typical temperature solution obtained from FEM-calculations. The outer surface of the sample (OD) is forced to follow the measured temperature curve. The calculated temperature response from inner surface (ID) and from about r=7.5 mm (R7.5) are presented. Note, that during the long cooling phase the temperature of the inner surface decreases to room temperature.

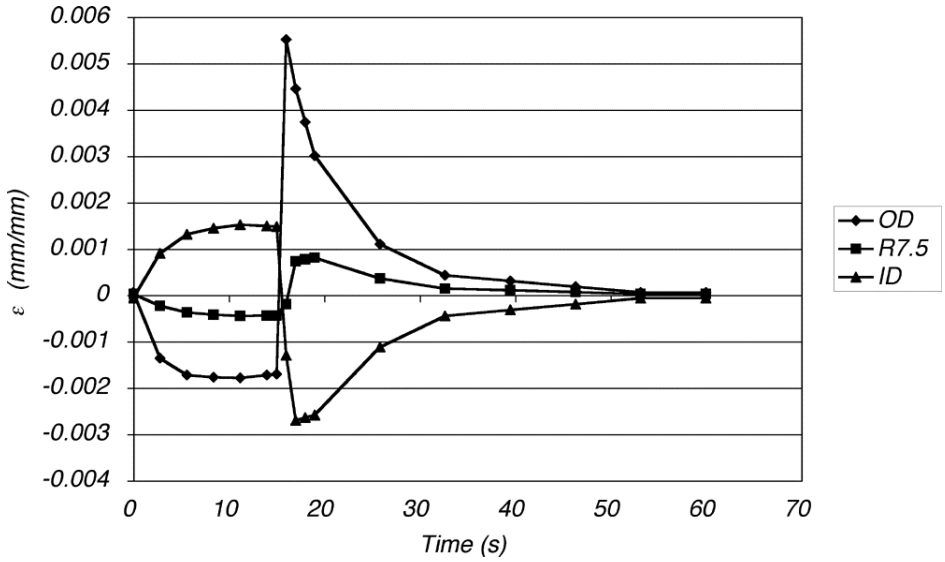

Figure 38. Axial strain solution corresponding to Figure 37. The $\Delta\varepsilon$ over the whole cycle is greatest at the outer surface (OD) and smallest at about r=7.5 mm.

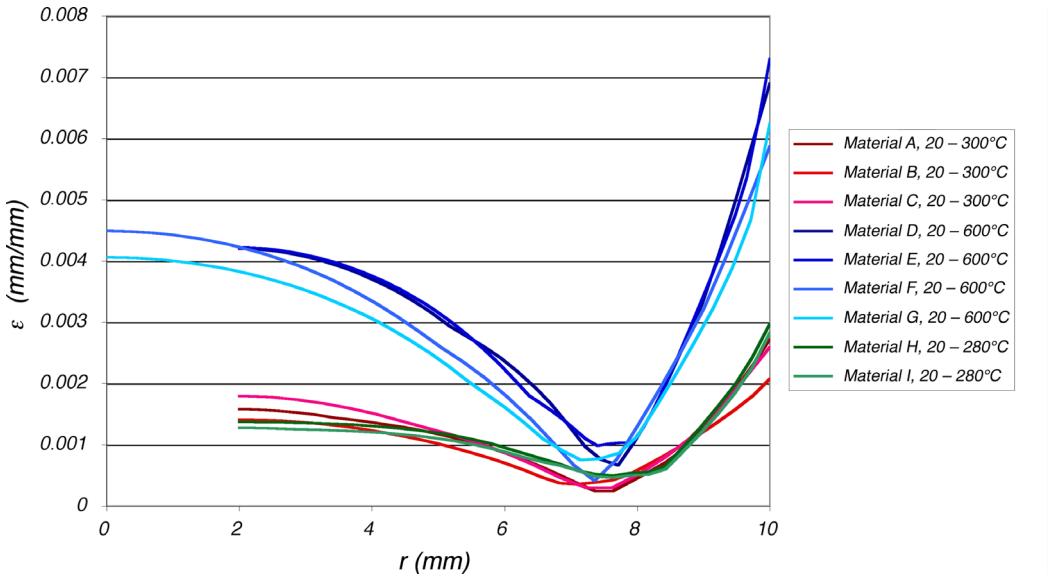

Figure 39. Axial $\Delta\varepsilon$ distributions calculated by FEM for different cycles. Sample surface is at r=10 mm. See Appendix 4 for more detailed presentation of this data.

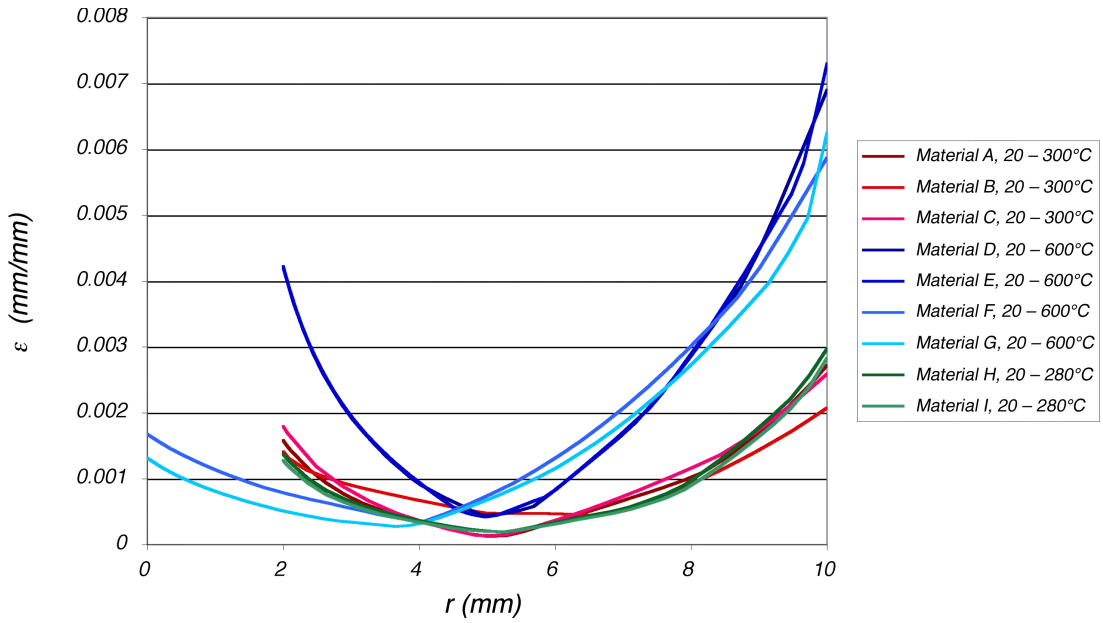

Figure 40. Tangential Δε distributions calculated by FEM for different cycles. Sample surface is at r=10 mm. See Appendix 4 for more detailed presentation of this data.

4.4 X-ray measurements

Residual stresses were measured before the fatigue testing and during the inspections. The tests were stopped for inspection after the cooling phase. Consequently, the residual stresses were measured after the high tensile strains caused by the cooling. After surface yielding in tension, compressive residual stresses are expected. The residual stresses measured are shown in Figures 41 – 45. In materials H and I the measured phase stresses (Figure 45) were converted to macroscopic stresses and microscopic stresses (Figure 47). In all the studied cycles the first large temperature cycles had the largest effect on residual stresses. Then cycles saturated, and, finally, as cracks formed in the sample, the surface residual stresses were relaxed.

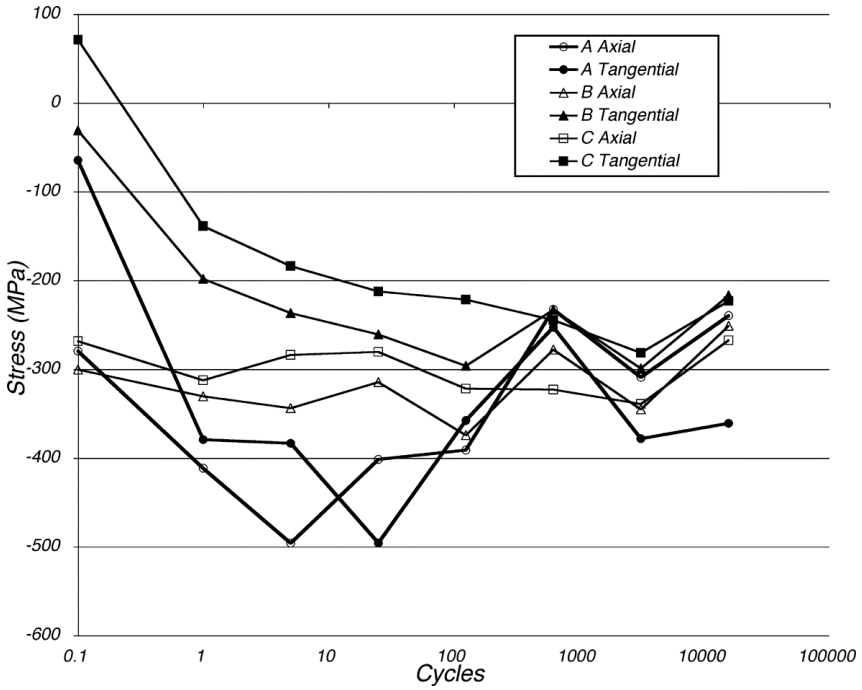

Figure 41. Residual stresses measured in materials A, B and C. Samples were loaded with the 20 – 300°C thermal cycle. Yielding caused by the large tensile strain at the beginning of the cooling phase causes compressive residual stresses at the surface. The residual stresses saturate after about 10 cycles. Some fluctuation is present in the measured residual stresses due to measurement uncertainty.

For the 20 – 300°C cycle (materials A, B and C) compressive residual stresses were measured. Before loading, each sample had a different residual stress state due to the thermal and manufacturing history of the particular sample. For the tangential direction, where the initial residual stresses were low (Figure 41), thermal cycling shifts residual stresses towards compression. After about 10 cycles the residual stresses saturate, and changes caused by subsequent thermal cycling are modest.

For materials F – G (Figures 42 and 43) the cycling started with lower temperature amplitude cycles and the first cycle shifts residual stresses towards tension. With increasing temperature amplitude the tensile strain applied increases and the measured residual stresses shift towards compression. A saturated residual stress state is reached after about 10 cycles, where measured residual stresses correspond to the cyclic flow stress of the material. After about 1000 cycles the measured residual stresses decrease due to crack formation.

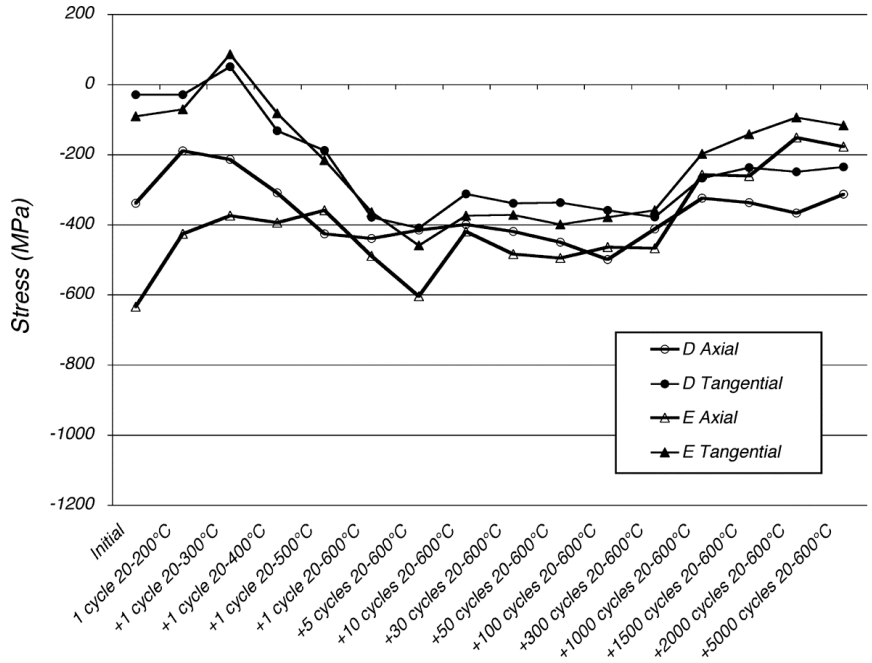

Figure 42. Residual stresses measured in materials D and E. Yielding during the large tensile strain at the beginning of the cooling phase induces compressive residual stresses to the surface. The residual stresses saturate after about 10 cycles. With high number of cycles, crack growth shifts stresses towards tension again.

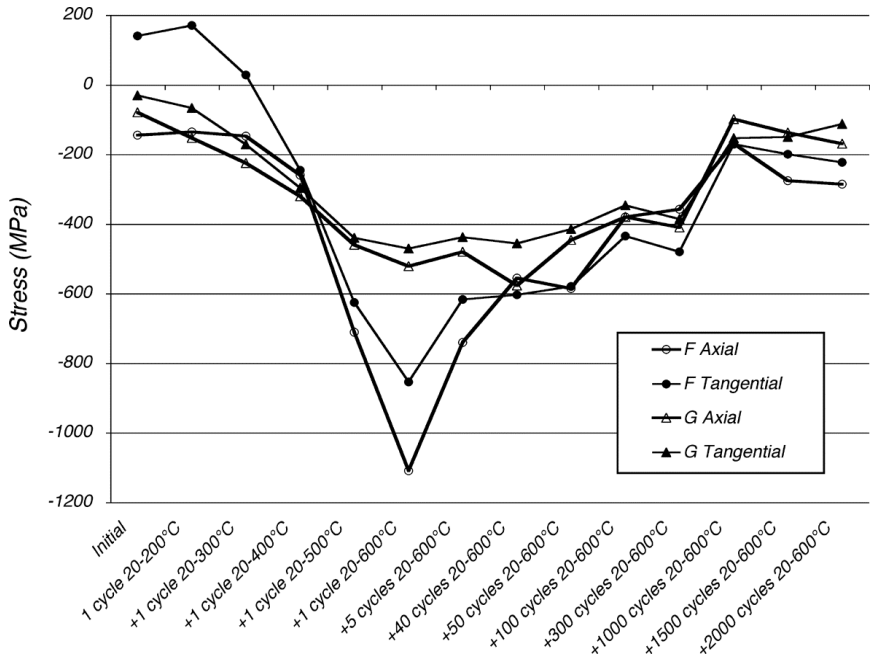

Figure 43. Residual stresses measured from materials F and G. Yielding during the large tensile strain at the beginning of the cooling phase induces compressive residual stresses to the surface. The residual stresses saturate after about 10 cycles. With high number of cycles, crack growth shifts stresses towards tension again. Some fluctuation is present in the measured residual stresses due to measurement uncertainty.

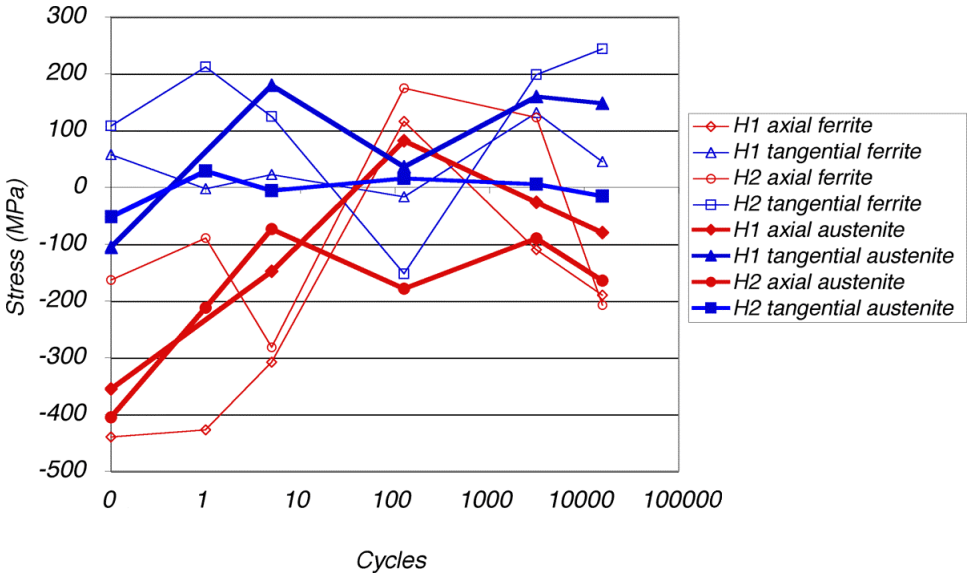

Figure 44. Residual stresses measured from material H. Numbers refer to the sample orientation. Sample was loaded with the 20 – 280°C temperature cycle.

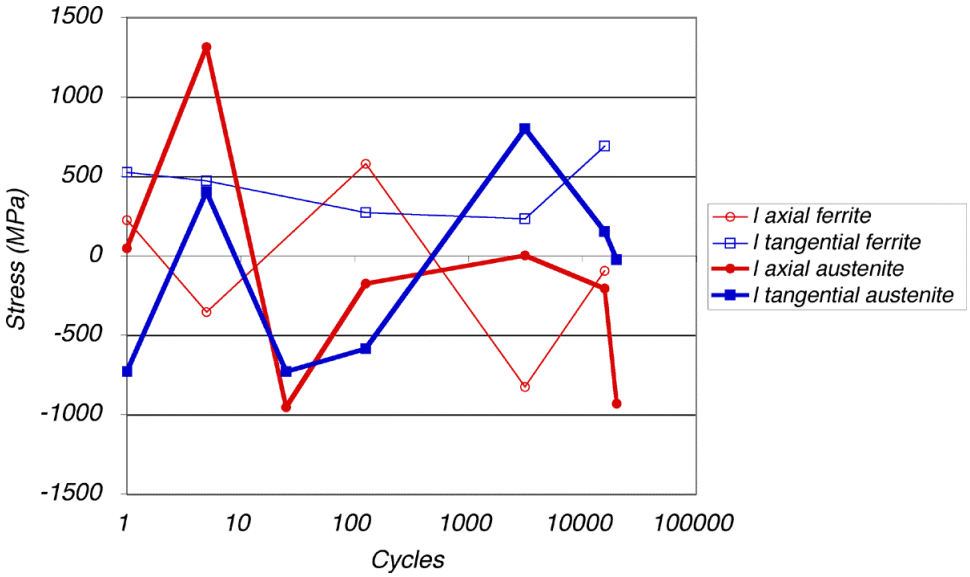

Figure 45. Residual stresses measured from material I. Sample was loaded with the 20 – 280°C temperature cycle.

Measuring residual stresses from the duplex stainless steels proved to be demanding due to the two-phase structure. The varying microstresses between the phases cause fluctuation in the test results. Microstresses also increase the uncertainty of the used $\sin^2\Psi$ method due to a strain gradient normal to the measured surface. The large grain size of the cast material I significantly weakened the reliability of the measurements. In Figures 44 and 45, the measured stresses are presented. Large fluctuations are evident in measurements from both materials. The calculated micro- and macrostresses are presented in Figures 46 and 47. For the cast material I the fluctuations are still very high and evidently reflects the large measurement uncertainties. For the material H the axial macrostress is

shifted towards tension, which is consistent with the calculated strain cycle. Large fluctuations still exist in the calculated microstresses. These fluctuations are due to differences in the phase morphology, which results in different microstresses in different grains.

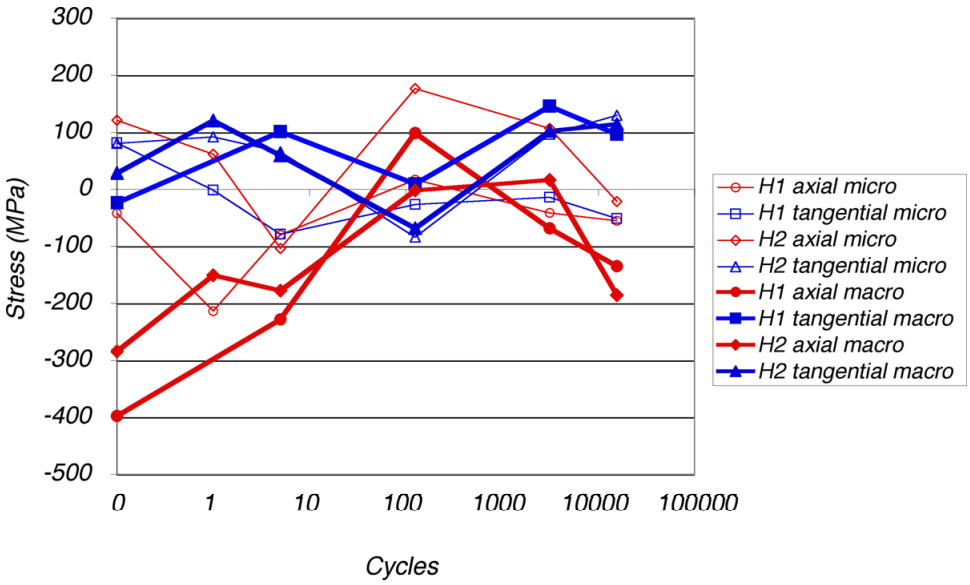

Figure 46. Residual stresses measured from material H (Figure 44) converted to macro- and microstresses. The axial macrostress is initially highly compressive in material H. The compressive stress during thermal cycling causes yielding in compression and shifts stresses towards tension.

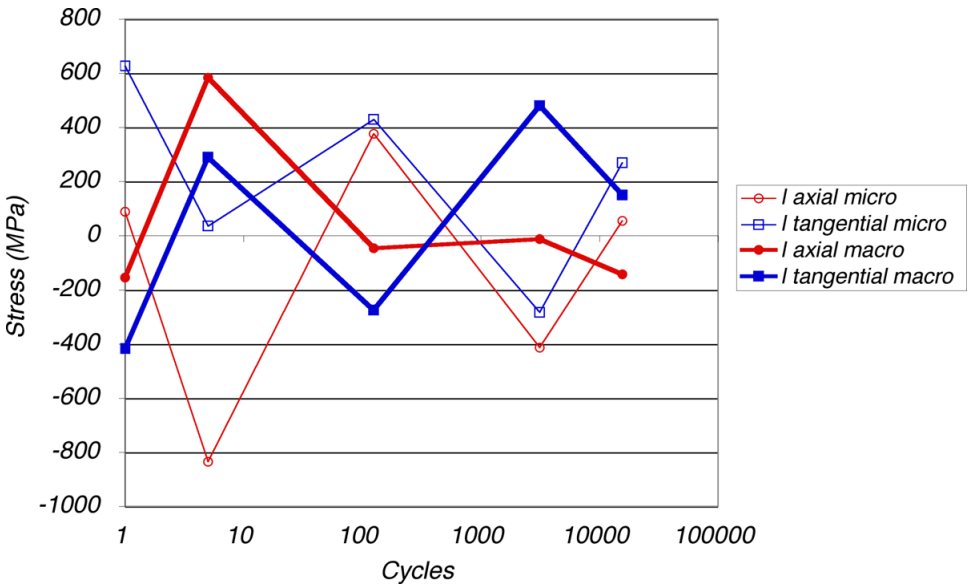

Figure 47. Residual stresses measured from material I (Figure 45) converted to macro- and microstresses.

The width of the X-ray diffraction peak was also monitored. In Figures 48 – 52 the measured peak's full width half maximum (FWHM) values are presented. Initially samples showed FWHM values varying from about 1.5 to 2.5 degrees. This variance is caused by the different manufacturing

histories of the samples. Thermal fatigue loading decreased the FWHM values in the samples with high initial values and increased FWHM in the samples with low initial values. The FWHM values of the samples stabilize to a value of about 2 in all of the materials and temperature cycles.

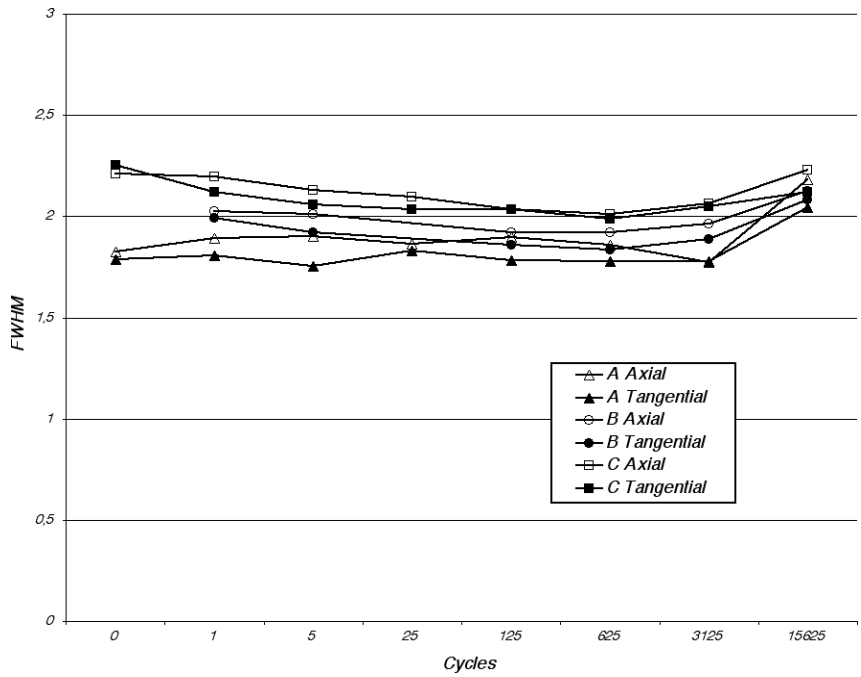

Figure 48. FWHM values measured from materials A, B and C. Samples were loaded with the 20 – 300°C temperature cycle. Changes in the FWHM values are modest. Slight decrease in the initially higher FWHM value of material C is observed and stabilization to a level of about 2 occurs.

For materials A, B and C the observed changes of FWHM due to thermal cycling are modest. The initial FWHM values around 2 are not altered by thermal cycling. Samples D, E and F were machined after heat treatment. Deformation during manufacturing has evidently increased the dislocation density in the sample, resulting in high initial FWHM values. Thermal cycling is observed to reduce the FWHM values. Sample G was stabilization heat treated after machining. Consequently the dislocation density is expected to be low. Also, the FWHM values measured in the sample before the cycling were very low. In this material, thermal cycling increased the FWHM values. After 2000 cycles the FWHM values reached a value of about 1.8.

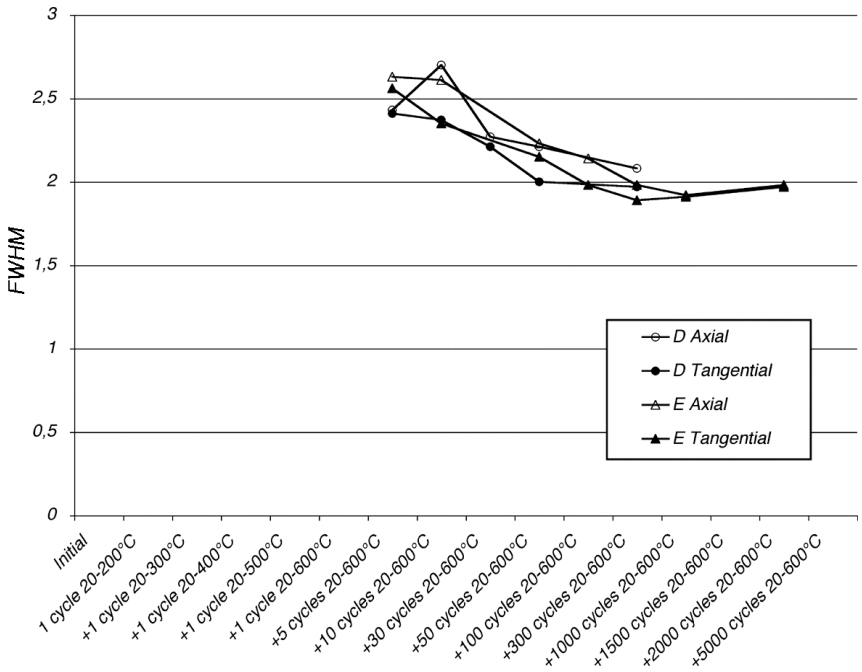

Figure 49. FWHM values measured in materials D and E. After deformation caused by machining the dislocation density of the sample surfaces can be assumed to be quite high. Consequently also the FWHM value measured is quite high. Thermal cycling decreases FWHM until it stabilizes to about 2.

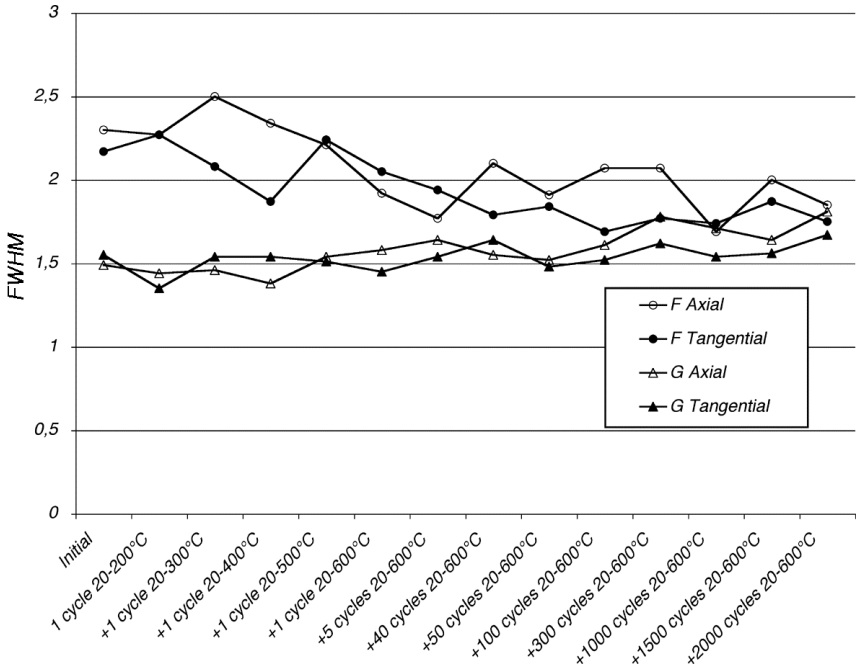

Figure 50. FWHM values measured in the materials F and G. In material F the initial dislocation density after machining is high and a decrease of FWHM similar to that of materials D and E is observed (Figure 49). The material G samples were solution heat treated after machining. Consequently the initial FWHM value (and dislocation density) is low and thermal cycling increased the FWHM value. FWHM values of both materials stabilize to about 2.

For materials H and I, large fluctuations are observed in the FWHM values. In the duplex stainless steels this is due to the scatter in microstresses between grains. The fluctuations in ferrite phase are smaller than in the austenite phase. This can be attributed to the microstructure; ferrite forms a continuous matrix, in which separate austenite grains are embedded.

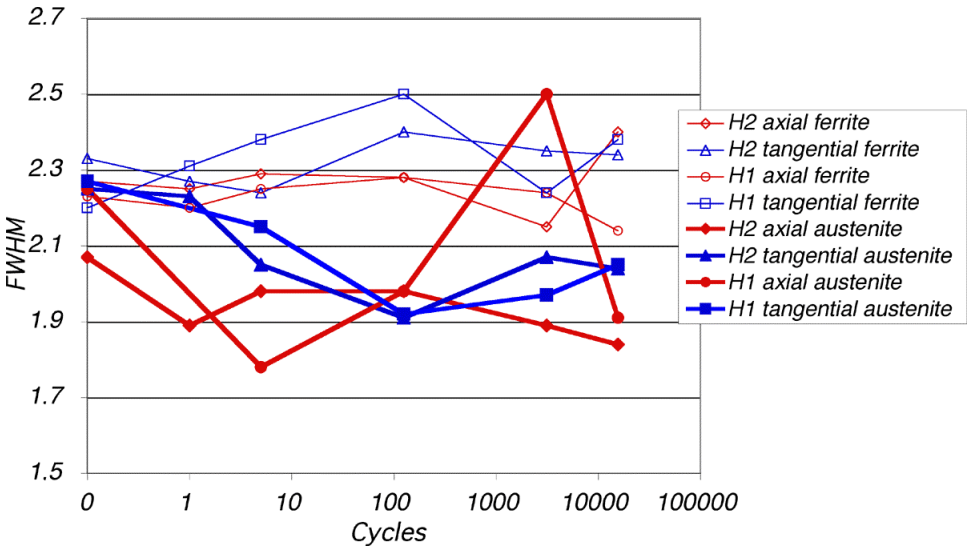

Figure 51. FWHM values measured in material H. Sample was loaded with the 20 – 280°C temperature cycle. In the austenite phase a stabilization of FWHM values to about 2 is seen. The FWHM values of the ferrite phase are unaffected by the thermal cycling.

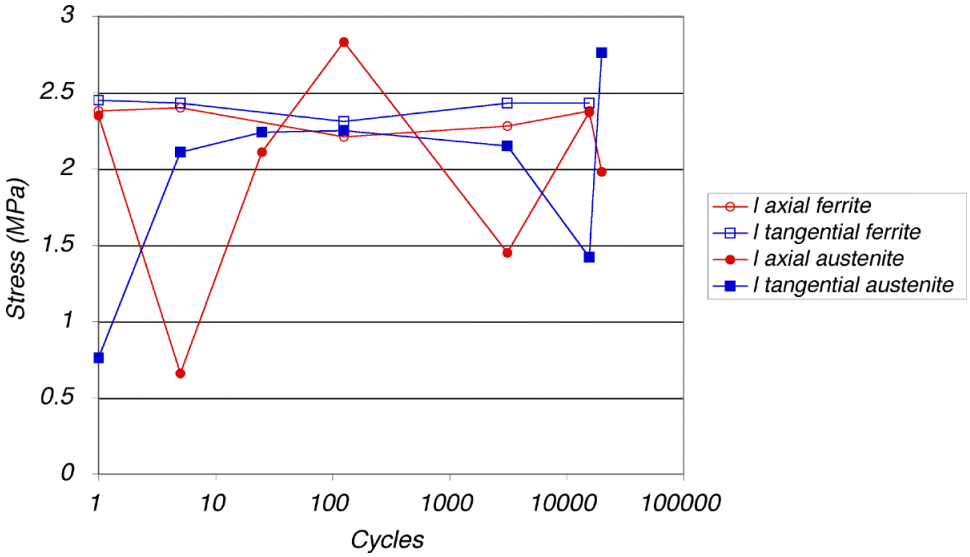

Figure 52. FWHM values measured in material I. Sample was loaded with the 20 – 280°C temperature cycle. The FWHM values of the ferrite phase are unaffected by the thermal cycling.

4.5 Contour method

The residual stress profiles of 8 samples of materials B to I loaded with 10 thermal cycles were measured with the contour method (Prime & Gonzales, 2000; Prime, 2001). The measurements presented here are not directly comparable to residual stress measurements presented in paragraph 4.4 due to possible stress relaxation before the residual stress measurements. The residual stress profiles measured are presented in Figure 53 together with FEM calculations and X-ray data.

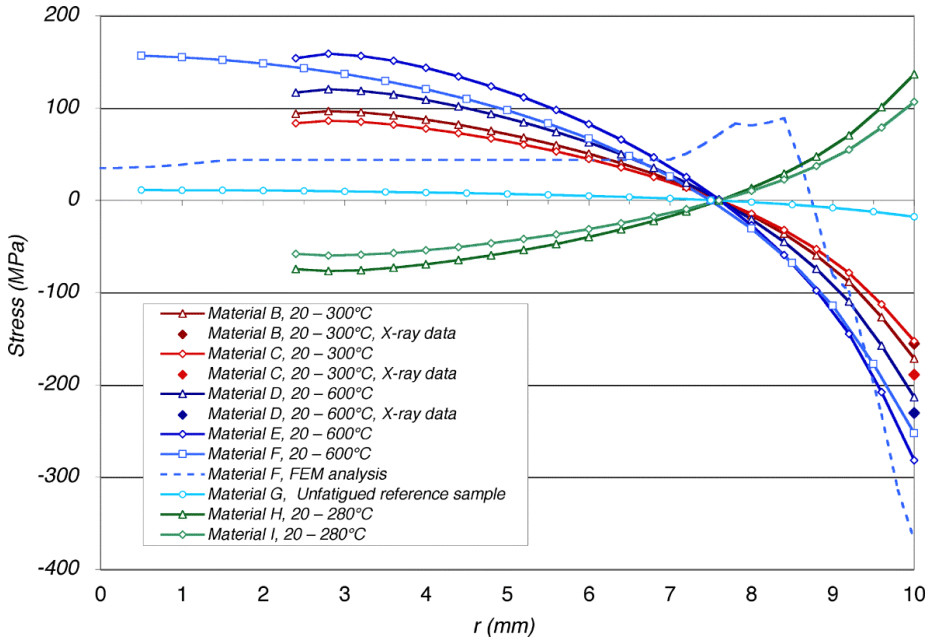

Figure 53. Residual stresses measured in the axial direction with the contour method presented with the FEM results and X-ray data.

The residual stress profiles measured show a point of zero stress at a depth of about 2.5 mm. The strain range solution from the FE analysis also showed a minimum at a depth of about 2.5 mm (Figure 53). However, the elastic-plastic FE analysis predicts plastic deformation only at the very surface of the sample thus deviating considerably from the measured profiles.

The austenitic samples (materials B – G) show compressive residual stress on the surface due to yielding in tension during the cooling phase. In the duplex samples (materials H – I) stresses were highest during the heating phase and yielding in the surface occurred in compression. Consequently, tensile residual stresses were measured.

4.6 Build-up of surface damage

In the austenitic materials (A – G), fatigue damage started with the formation of persistent slip bands (PSBs). As the fatigue continued, more PSBs formed and existing PSBs grew to form microcracks. Microcracks

formed in all directions and no preferred orientation was seen. This indicates an equi-biaxial stress state. Soon, the cracks formed a mosaic-like network typical for thermal fatigue. In such a network, the length and growth of individual cracks could not be monitored from the surface. In Figures 54 and 55 the crack growth of different materials as seen in the replicas is presented. Cracks with surface length of 100 µm or more were observed after about 500 – 1500 cycles.

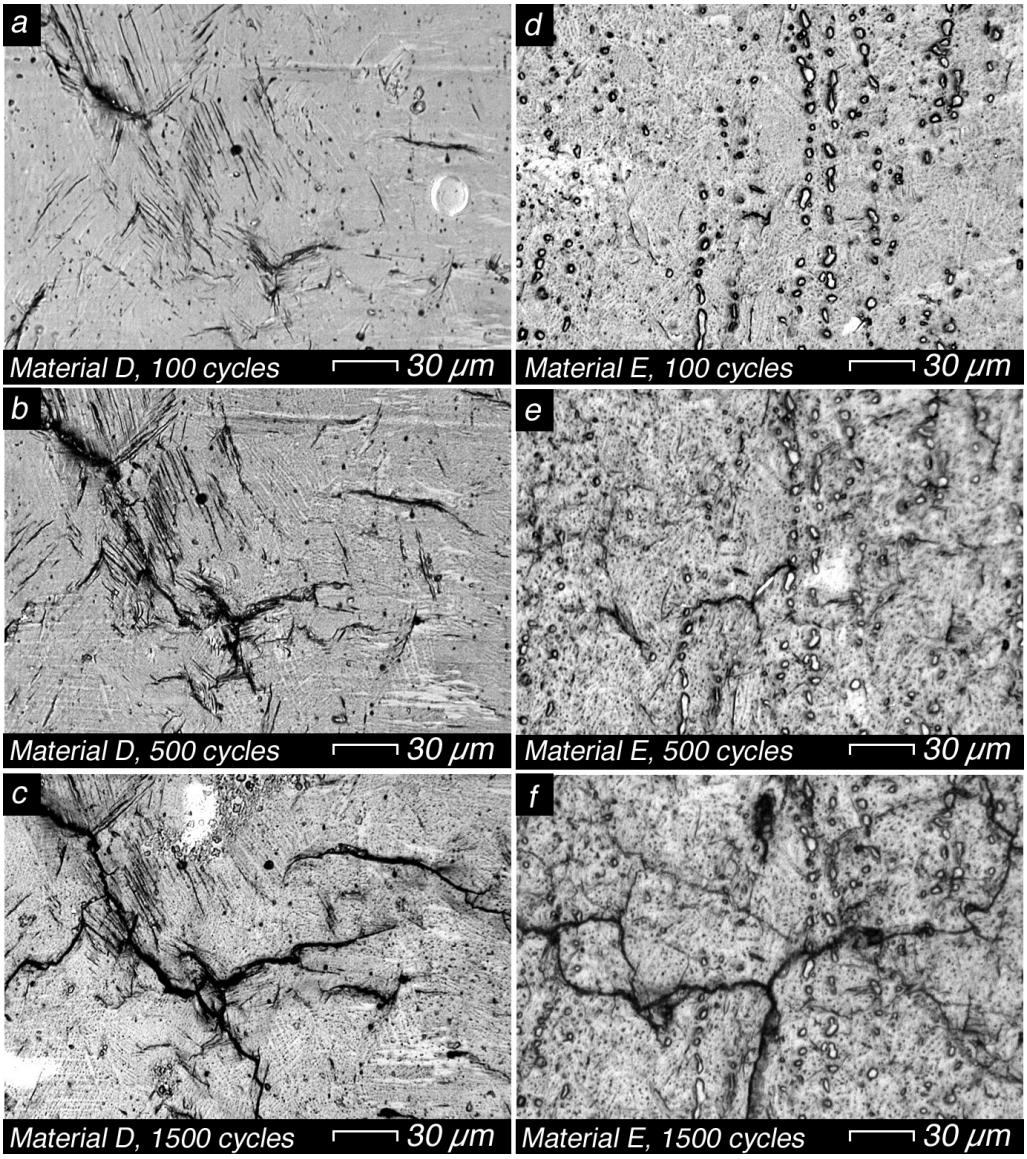

Figure 54. Crack growth as seen in the replicas. On the left material D is shown after 100 (a), 500 (b) and 1500 (c) cycles of 20 – 600°C. On the right material E is shown after 100 (d), 500 (e) and 1500 (f) cycles of 20 – 600°C.

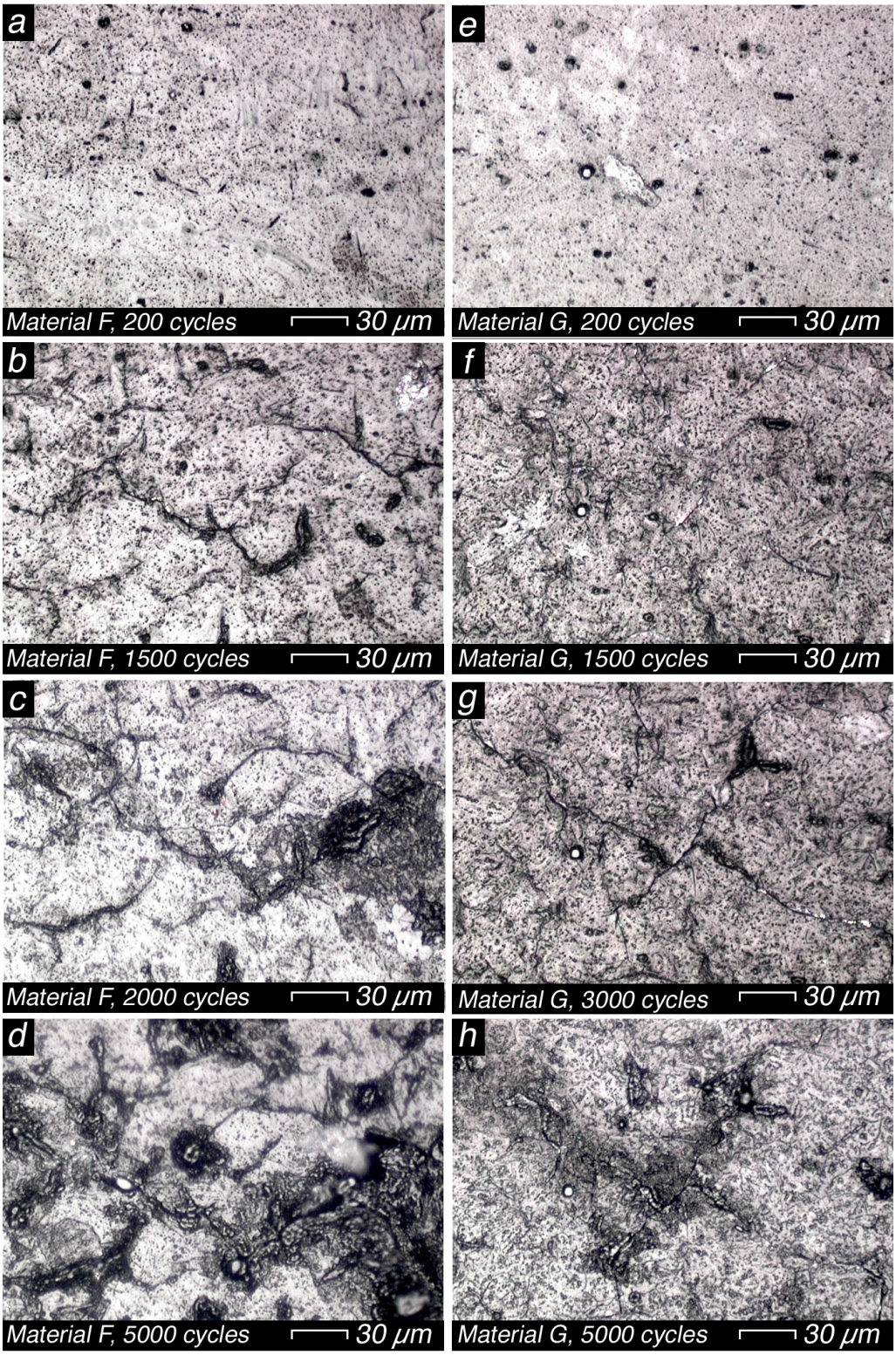

Figure 55. Crack growth as seen in the replicas. On the left material F is shown after 200 (a), 1500 (b), 2000 (c) and 5000 (d) cycles of 20 – 600°C. On the right material G is shown after 200 (e), 1500 (f), 3000 (g) and 5000 (h) cycles of 20 – 600°C.

In the duplex stainless steel samples (H and I) cracks were seen to initiate from PSBs in austenite grains and from MnS inclusions. The primary initiation site depended upon the size of the inclusions; if the inclusions were bigger than the available austenite grains, then dominating

cracks initiated from the inclusions. This behavior resulted in a significant anisotropy in the fatigue properties of the wrought material H. In material H, where the nitrogen content in the austenite is lower, PSBs often occurred in multiple directions. In the material I with the higher austenite nitrogen content, PSBs formed predominantly in a single direction within the grains.

Phase boundaries were seen to retard the crack growth significantly. Often microcracks initiated in two adjacent austenite grains, and the phase boundary was overcome only when the ferrite ligament between them finally broke. In the duplex stainless steels, the growth of individual cracks could be measured in the replicas. The measured crack growth data for materials H and I and temperature cycle 20 – 280°C are presented in Figure 56.

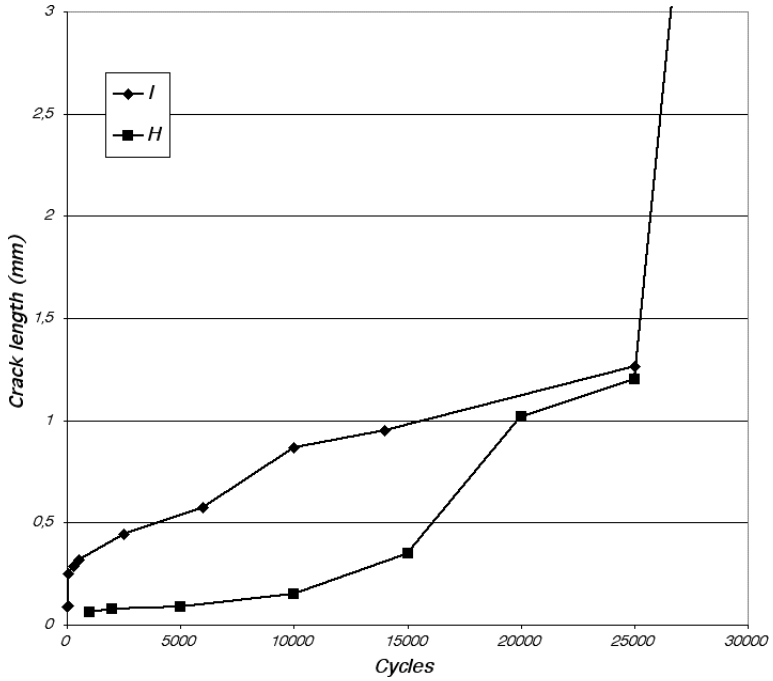

Figure 56. Crack growth in materials H and I, temperature cycle 20 – 280°C. Material H showed significant anisotropy in crack growth. Crack growth in orientation 1 (see Figure 24 for the definition of orientations) was so small that it could not be measured.

4.7 Fractography

In all samples, where possible, an axial crack was opened for fractographic examination. In the austenitic materials (A, D, E, F and G) the fracture surfaces showed extensive striation formation (Figure 57). The striation spacing was measured at several locations on the fracture surface. The measured striation spacings are shown in Figure 58.

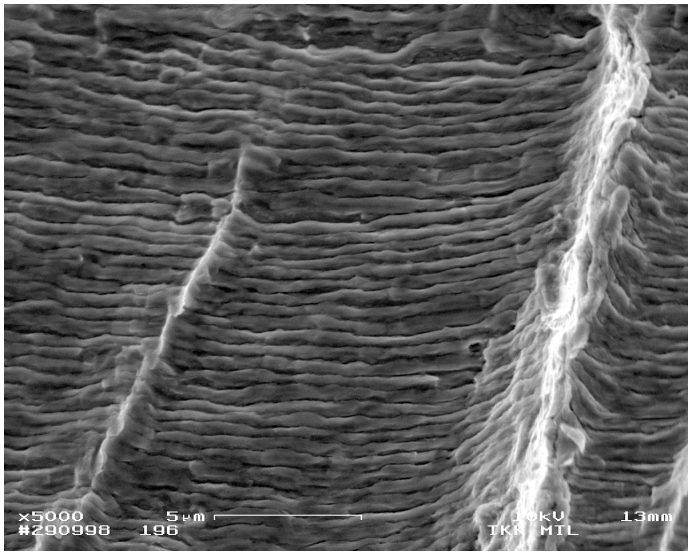

Figure 57. Typical fracture surface of austenitic materials showed extensive striation formation. Image from material A after 15625 cycles of 20 – 300°C.

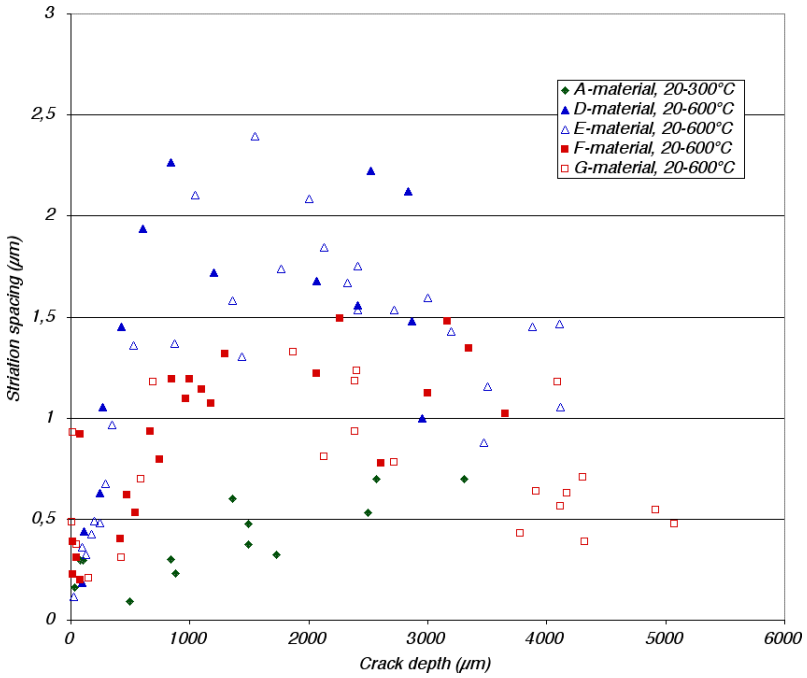

Figure 58. Striation spacings measured from materials C, D, E, F and G.

In the measured range the striation spacing can be considered as an indication of the crack advance per cycle. The scatter in local crack growth rate increased with increasing crack length. The observed decrease in the macroscopic crack growth rate scatter is due to averaging of local crack growth rates in the crack front. By taking the striation spacing as a direct indication of the instantaneous crack growth rate and assuming that the crack growth rate changes linearly between the measured points, the crack growth as a function of cycle number could be calculated. The obtained growth curves are presented in Figure 59.

At small crack depths the striation spacing is small. With increasing crack depth the striation spacing increases sharply although the nominal $\Delta\varepsilon$ at the crack tip location diminishes. After the crack depth reaches about 1.5 mm, the effect of decreasing strain amplitude surpasses the effect of increasing crack depth and the crack growth slows down.

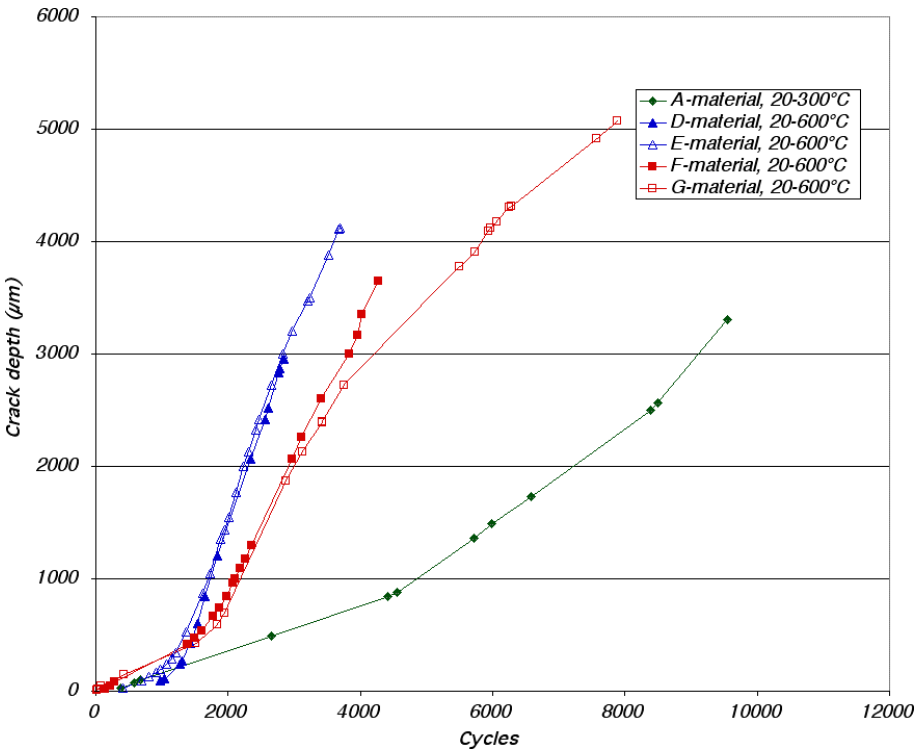

Figure 59. Crack growth calculated from the measured striation spacings.

In the duplex stainless steels, the two-phase microstructure significantly affected the crack growth. Fracture surfaces showed signs of many different crack growth mechanisms. Occasionally in the austenite phase, ductile striations similar to those in austenitic materials were seen (Figure 60). In addition, crack growth by alternating fracture plane (Figure 61) and in ferrite, in one location, brittle striations were observed (Figure 62).

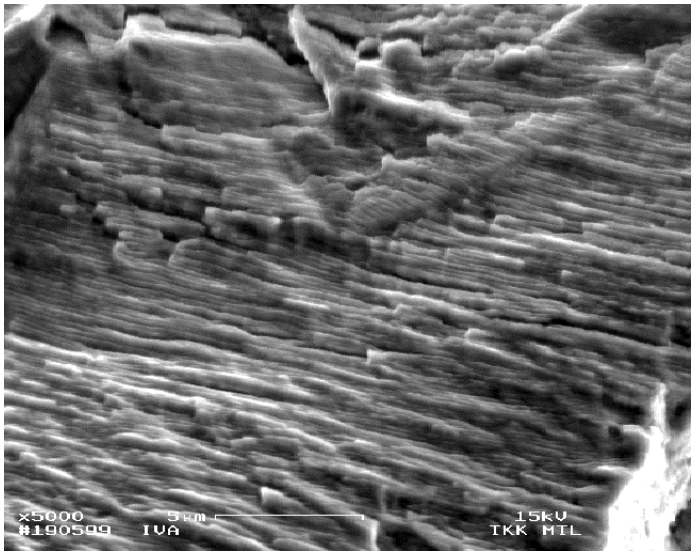

Figure 60. Ductile striations similar to those in austenitic materials in the austenite phase of material I after 20000 cycles of 20 – 280°C.

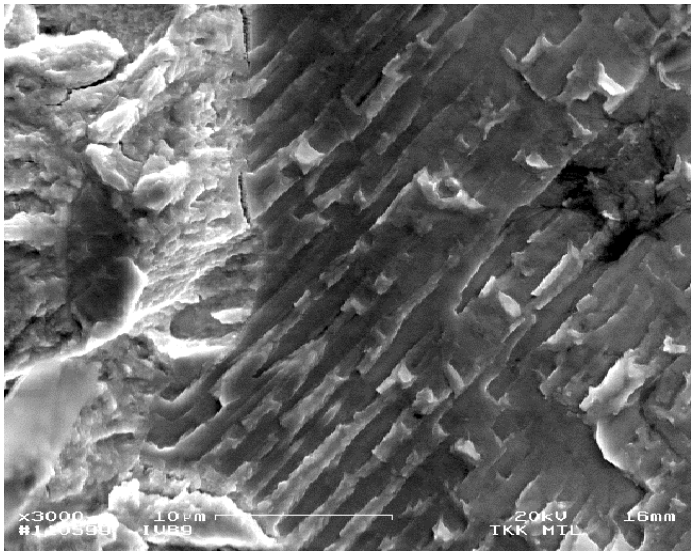

Figure 61. Crack growth by alternating fracture plane. Austenite phase of material H after 20000 cycles of 20 – 280°C.

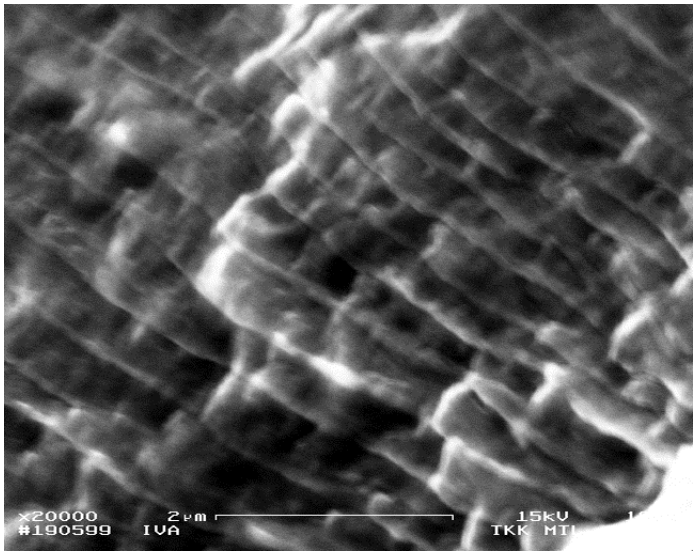

Figure 62. Brittle striations in the ferrite phase of material I after 20000 cycles of 20 – 280°C.

The edge of the fracture surface and the sample surface was studied to reveal the crack initiation and growth in the two-phase materials. Figure 63 shows that the crack growth mechanism is different in the austenite and ferrite phases. In austenite a pattern typical for stage I fatigue crack growth is seen, while in ferrite no deformation outside the crack wake is visible. Also, secondary cracks in PSBs are observed in stage II fatigue crack growth (Figure 64). Crack initiation was seen to be caused by extrusions and intrusions in the austenite grains (Figure 65).

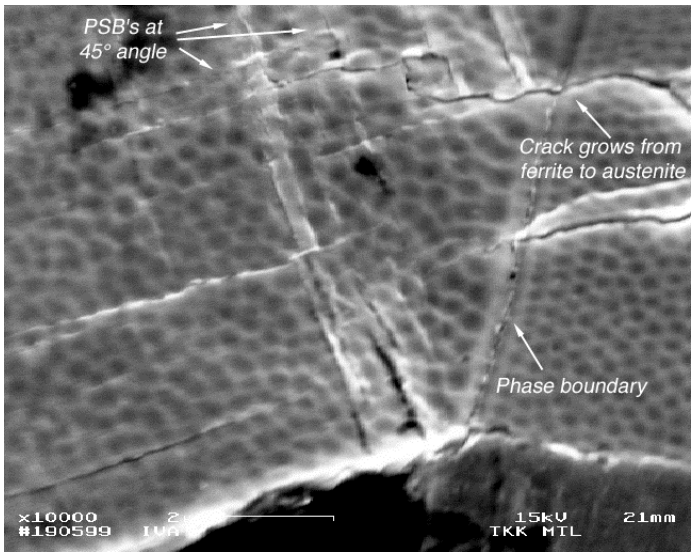

Figure 63. Crack grows from ferrite (right) to austenite (left) in material I. See text for details.

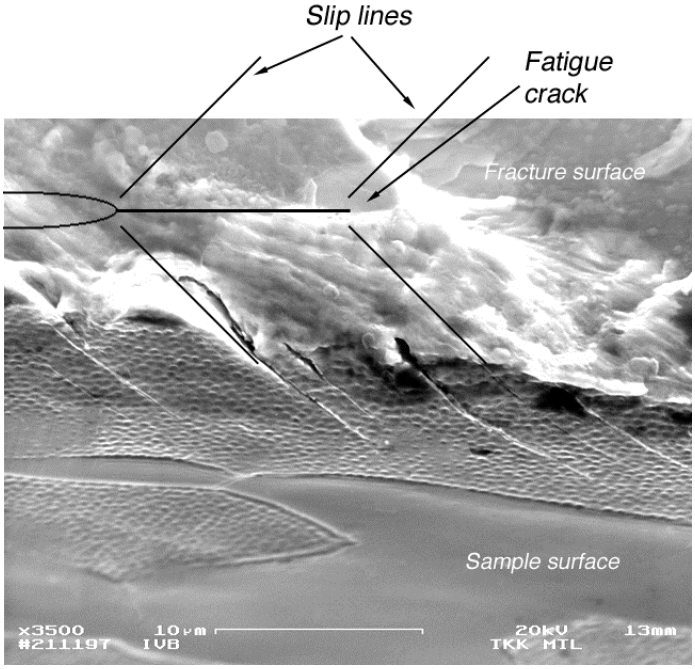

Figure 64. Secondary cracks along PSBs in stage II crack growth (material H) (schematic graphics after Suresh, 1992).

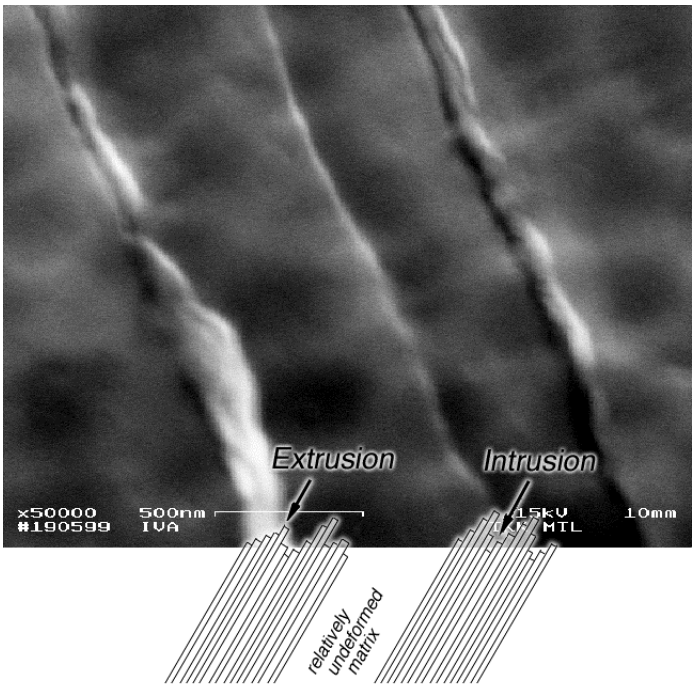

Figure 65. Extrusions and intrusions on sample surface of material I (schematic graphics after Suresh, 1992).

4.8 Dislocation structures

The TEM studies showed that dislocation density in all studied materials was lower than expected based on mechanical fatigue data. Dislocation

tangles and occasional cell tendency were observed. Typical dislocation structures observed are shown in Figures 66 – 67.

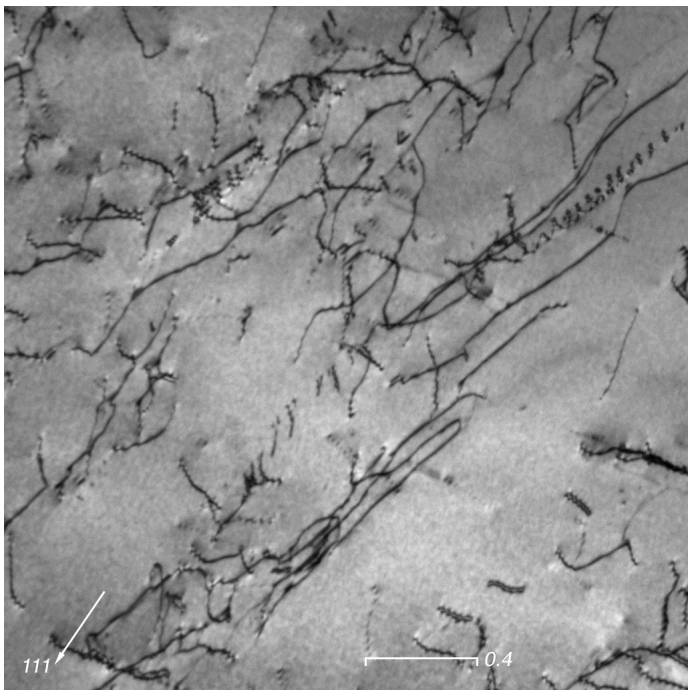

Figure 66. Dislocation structure of material B after 15625 cycles of 20 – 300°C. Dislocation tangles and low dislocation density was observed.

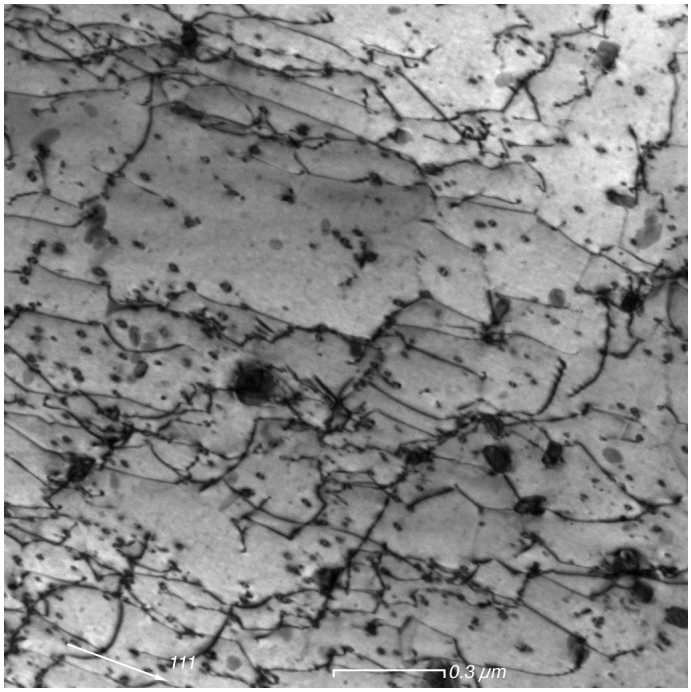

Figure 67. Dislocation structure of material F after 10000 cycles of 20 – 600°C. Dislocation tangles and low dislocation density was observed. Numerous Nb-rich precipitates are visible.

In the duplex stainless steels the dislocation density of the austenite phase was greater than that of the ferrite phase. This indicates that plastic deformation has been localized in the austenite phase. Typical dislocation structures are shown in Figures 68 – 69. More stacking faults are observed in the austenite phase of material H than of material I or in the studied austenitic materials (A – G). This indicates that the stacking fault energy (SFE) of the austenite phase of material H is lower than that of other studied materials. In material H, small amounts of χ-phase were observed in phase boundaries (Figure 70).

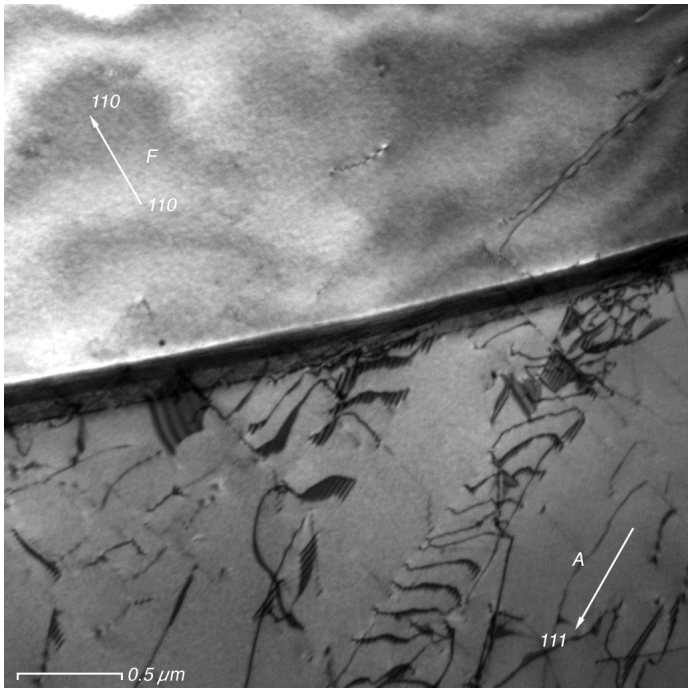

Figure 68. Dislocation structure of material H after 15625 cycles of 20 – 280°C. Planar slip bands are observed in the austenite phase. The dislocation density of austenite is higher than that of ferrite. Numerous stacking faults are observed in the austenite phase.

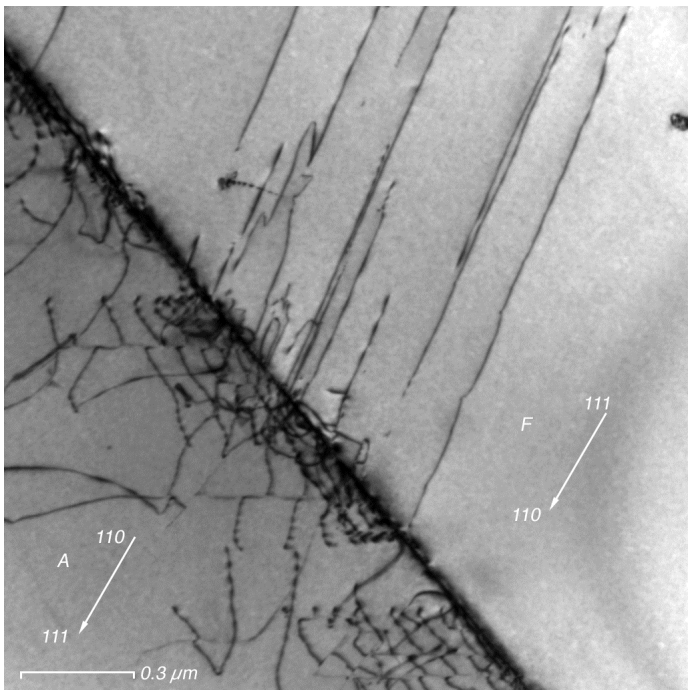

Figure 69. Dislocation structure of material I after 15625 cycles of 20 – 280°C. Dislocation tangles are observed in the austenite phase. The ferrite phase shows parallel dislocation alignments. The dislocation density of austenite is higher than that of ferrite.

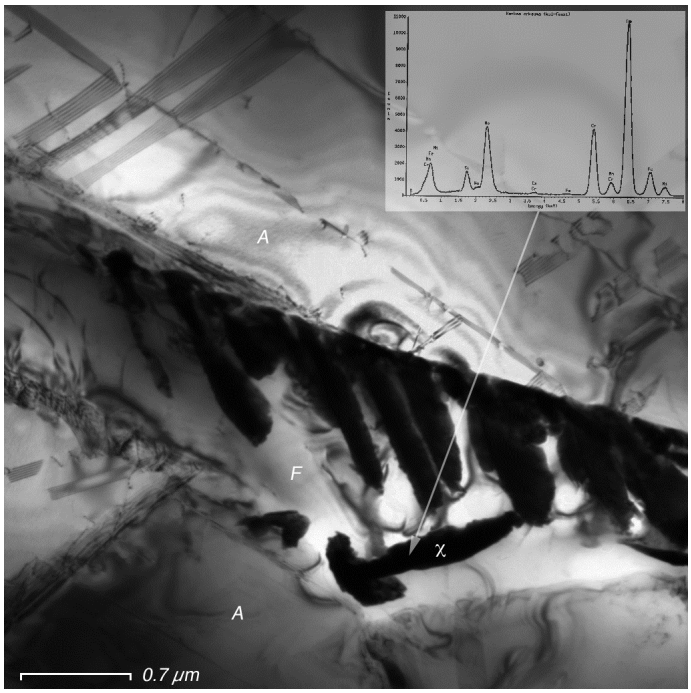

Figure 70. The secondary phase observed at the phase boundaries of material H was identified as χ -phase.

5 DISCUSSION

5.1 Cyclic thermal loads and residual stresses

The surface stresses during all of the used thermal cycles exceeded the monotonic yield limit of the material. Consequently, the thermal cycling altered the residual stresses of the samples. A schematic stress-strain curve of the load cycle on the sample surface of the austenitic stainless steel samples is presented in Figure 71 (see also Appendix 1).

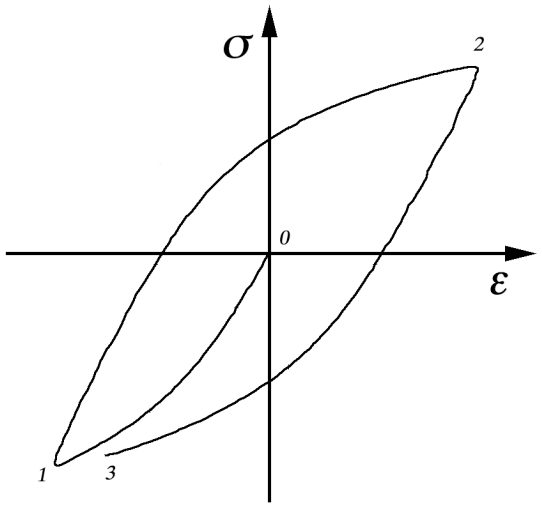

Figure 71. A schematic stress-strain curve for the surface of an austenitic sample during thermal cycling. In the beginning of the cycle heating causes compressive stress at the specimen surface (0 – 1). When the cooling phase begins, high tensile stresses and yielding are induced to the sample surface (1 – 2). When cooling is continued, the temperature distribution in the sample evens out (2 – 3). Because of uneven yielding during the cooling phase, a compressive residual stress is produced at the sample surface (3).

The surface residual stresses changed markedly during the first load cycles (Figures 41 – 47). After about 10 cycles the stresses stabilized. In cycles with a high strain amplitude, the stabilized value corresponded to the cyclic flow stress of the cyclic stress-strain curve (materials F and G). In these samples the residual stress state prior to thermal cycling had no effect on the final stress state. In samples where the thermal strains were lower, the prior residual stresses also had an influence on the stabilized residual stresses. After continued fatigue, thermal fatigue cracks started to alter the residual stresses and the residual stresses shifted towards tension.

The 20 – 600°C cycle (material F) was modeled with an elastic-plastic numerical model, which predicted the residual stress state. In Figure 53 the calculated residual stresses are compared with the stresses measured by the contour method and X-ray diffraction. The agreement of different

measurement techniques is good, while the agreement with the numerical simulation is poor. The FE-model predicts plastic strains only on the very surface, whereas the contour measurements show that plastic deformation is more evenly distributed in the sample. The difference is apparently because the yield strength in the stabilized stress-strain curve is larger than the yield strength observed in the monotonic tensile test or during the first fatigue cycle. The used material model and data describe heavily deformed material, such as that in the surface layer. Therefore, the surface residual stress is correctly predicted by the FE-model. TEM images show, however that this does not describe the whole sample (Figures 66 – 67). To correctly model the loading and to correctly predict the residual stresses, a history-dependent material model should be used, which would update the stress-strain curve on each load reversal based on prior deformation. Such a material model is not available, and hence the plastic strains in the thermal fatigue test could not be adequately modeled.

In duplex stainless steels, the plastic deformation in uniaxial mechanical loading was seen to concentrate in the austenite phase. The concentration was greater in the cast material I, where the phase morphology caused little interphase constraint. Uneven plastic deformation in tension resulted in compressive residual microstress in the austenite phase and tensile microstress in the ferrite phase, as already noted by several authors (Kamachi et al., 1982; Siegmund et al., 1993). The concentration of plastic deformation in the austenite phase was also seen from the TEM-studies of thermally fatigued samples.

5.2 Micromechanism of crack growth

In the studied austenitic materials, cracks initiated from PSBs. In materials with larger grain size, the PSBs were broader and the initiation occurred more easily. In duplex stainless steels the initiation was observed at PSBs in austenite grains (both materials H and I) and at MnS inclusions (material H, orientation 2). In material H, where the inclusions were bigger than the austenite grains, the dominating cracks initiated from these inclusions. In material I, where round inclusions were smaller than the austenite grain size, the inclusions had no notable effect on the fatigue behavior. The fatigue life of the specimens was seen to depend on the largest initiation site available. The biggest cracks were found from the orientation 2 of the material H, where elongated MnS inclusions were available as crack initiators. In the orientation 1 of material H the MnS inclusions were not available and the austenite phase size was very small. Consequently, the crack initiation occurred later than in other cases, and crack growth was considerably slower. In material I the crack growth was between these two extremes. The cracks initiated from PSBs in the austenite grains, but due to the bigger grain size of material I, crack growth was faster than in orientation 1 of material H.

The fracture surfaces of the austenitic test materials showed extensive striation formation (Figure 57). This is typical for austenitic stainless steels also in mechanical fatigue. Similar striations were seen in the cyclic stress-strain samples, which were isothermally fatigued at different temperatures. The fracture surfaces of the austenitic materials are therefore very similar to those of mechanical fatigue. The fracture surfaces showed no evidence of stress corrosion fatigue, and the possible environmental effects of the water quenching used are a result of true corrosion fatigue.

In the duplex stainless steels the two-phase microstructure allowed many different fracture mechanisms to be active. Ductile striations, similar to those in austenitic materials, were seen in the austenite phase of the duplex samples. In addition, fracture by altering fracture plane and brittle-like fracture, both transgranular and intergranular, were seen. These complex fracture surfaces are also typical in mechanical fatigue of duplex stainless steels. Apparently the interphase stresses and the different crack growth mechanims in the two phases cause high local fluctuations in the strains at the crack tip, and thus the complex fracture surfaces observed.

While the micrometer-scale fatigue mechanism of thermal fatigue seems to be similar to that of mechanical fatigue, the dislocation structures observed are quite different. In mechanical and thermomechanical fatigue with externally applied loads or constraints, tightly arranged dislocation structures, such as walls-and-channels, cells or corduroy, are typical (see paragraph 1.4). In the present study, dislocation tangles and low dislocation density were observed (Figures 66 – 67). However, similar dislocation structures have recently been found in AISI 304 cracked cladding of recovery boiler composite tubes (Keiser et al., 1996). At first this dislocation arrangement was considered as evidence of the absence of thermal fatigue. Further study (Keiser et al., 1997) with a thermally fatigued reference samples showed that the observed dislocation structure is typical for thermal fatigue. Other, more recent, studies on recovery boiler composite tubes confirmed those results (Saarinen et al., 2000).

The low dislocation densities observed in the present study can be attributed to the fact that the TEM sample was taken from a depth of about 2 mm. The strain amplitude seen by the material at this depth is much smaller than at the surface. The axial and tangential strain amplitudes are about 14% and 40% of the maximum amplitude, respectively.

It is generally found that cold work and fatigue tend to increase the width of X-ray diffraction peaks. From Figures 48 – 52 it is seen that this is not necessarily the case in thermal fatigue. The diffraction peaks of some samples do show a small increase, while for other samples a decrease in FWHM is observed. The increase of FWHM is observed predominantly in stabilized samples, where initial dislocation density can be assumed to be low. The decrease of FWHM is seen in materials, where initial dislocation

density is higher due to sample manufacturing. The FWHM values of different materials tend towards the value of about 2. This indicates that the low dislocation density observed in the TEM studies is characteristic to thermal fatigue loading.

5.3 Thermal fatigue prediction

Based on the replica studies and fractographic studies, the fatigue crack growth rate in the samples could be estimated. Following the interpretation of Chopra & Shack (1999), an S-N plot for the number of cycles required to grow a 3 mm deep "engineering crack" can be drawn (Figure 72). The load is plotted according to the calculated total surface strain range. The strain range decreased rapidly towards the inside of the specimen. Consequently the plot should be considered as a rough estimate only.

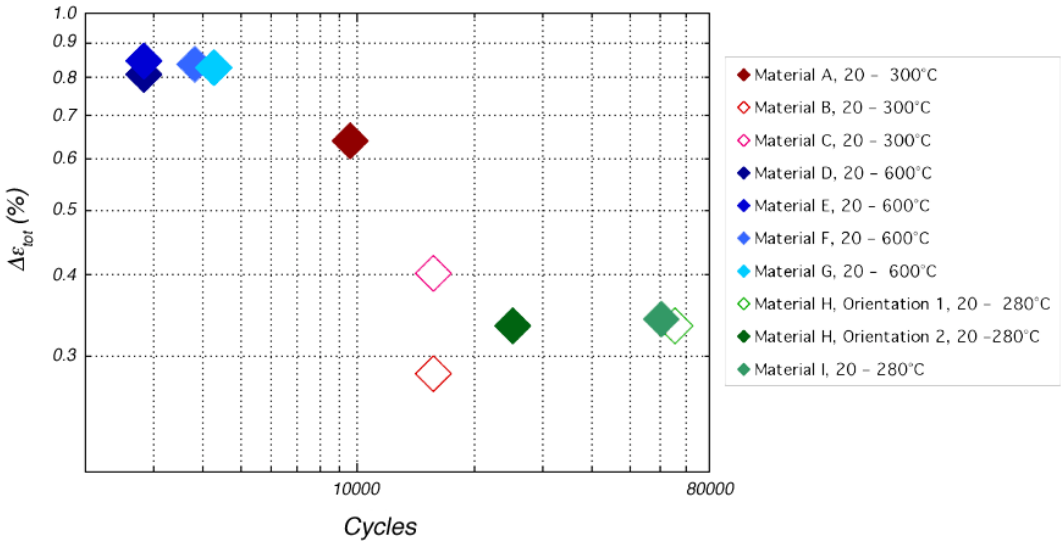

Figure 72. S-N plot for cycles required to grow a 3 mm deep surface crack. Total strain range is plotted according to calculated surface strain range. Open dots are run-outs. The strains were obtained from FEM-calculations (Figure 40) and the cycle numbers from striation spacing measurements (Figure 59) and replica studies (Figure 56).

Numerous crack growth models have been proposed in literature (see paragraph 1.8). The application of most of these models to the current thermal fatigue load case is, however, not trivial. The linear-elastic K-based models are not applicable to current thermal fatigue crack growth due to plasticity in the specimen surface layer. To numerically determine the J-values, the crack tip stresses and strains (elastic and plastic) must be known. The stresses and plastic strains of even an uncracked geometry could not be reliably solved using the current nonlinear material models (paragraph 5.1). In addition, the temperature gradients present make the numerical evaluation of J more difficult. Hence, the ΔJ-distribution of the

current thermal fatigue load case could not be determined numerically. Similarly, lack of a reliable cyclic, non-linear stress solution for the uncracked geometry prevents the direct use of some strain-based parameters, which require the plastic strain amplitude to be known. Equations 17 and 27 can be used with q set to 1, i.e. $\varepsilon_{eq}=\varepsilon_{tot}$, together with the Paris law (a similar approach was used earlier by Solomon, 1972) (equation 43):

$$\frac{da}{dN} = C_2\left[\Delta\varepsilon_{tot}\sqrt{\pi a}\right]^{m_2}. \tag{43}$$

The correlation with experimental data is, however, poor, as seen in Figure 73.

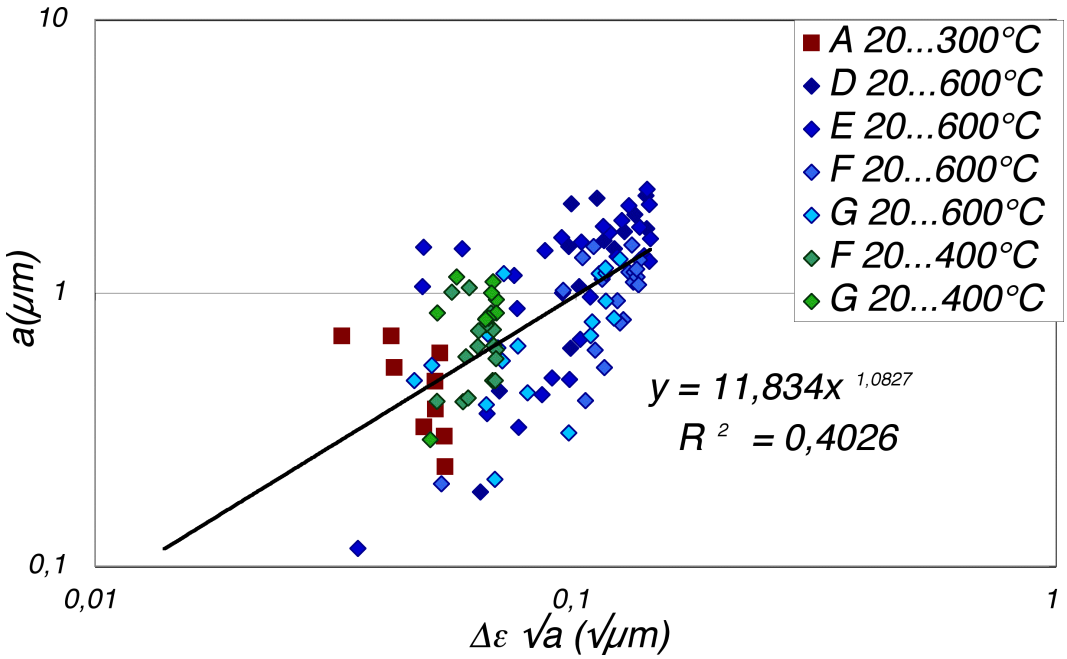

Figure 73. Crack growth rates calculated from equation 43 and measured striation spacings.

A much better correlation is achieved using equation 30 with total strain, i.e.:

$$\frac{da}{dN} = C_7\Delta\varepsilon_{tot}^{m_7} a. \tag{44}$$

A similar approach has been used by Solomon (1972), Skelton et al. (1996), Taira et al. (1976), Nisitani et al. (1992) and Kawagoishi et al. (2000). Crack growth rate curves based on equation 44 are presented in Figure 74. Because of the inherent scatter in the striation spacing measurements, correlation with experimental data points can be considered good. The thermal fatigue crack growth rates for several materials and temperature cycles can, thus, be predicted based on the linear-elastic total strain solution of an uncracked component together with equation 44, as long as the required parameters C_7 and m_7 are

experimentally determined. In Figure 75 experimental thermal fatigue data from Marsh (1981) and the present study is presented. The agreement with the present results is excellent.

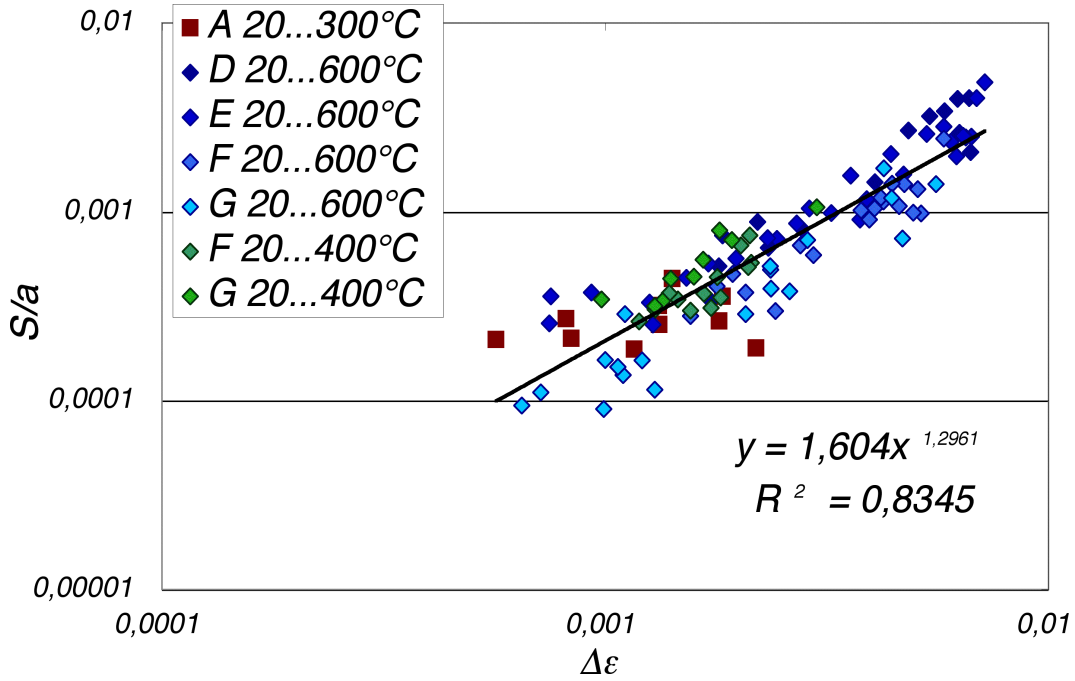

Figure 74. Crack growth rates calculated using equation 44 and measured striation spacings. The open symbols represent data points measured at very low crack growth rates. These points were not included in the curve fitting. Striation spacing divided by the crack length (S/a) is plotted against the strain range (Δε) on a log-log scale to give linear fit for equation 44.

The crack growth predicted by Figure 74 is presented in Figure 76. In order to calculate the crack growth from equation 44, an initial crack length a_0 is assumed. A value of a_0=50 µm was used based on the upper limit grain size of the materials. Due to fast crack initiation, the estimation is not sensitive to the chosen value of a_0. The assumed initial crack size adds conservativism to the prediction. In the case of the 20 – 600°C temperature cycle this effect can be estimated based on the replica studies (Figures 54 and 55) to be about 500 – 1500 cycles. With decreasing strain range the number of cycles required to form an initial crack of 50 µm increases.

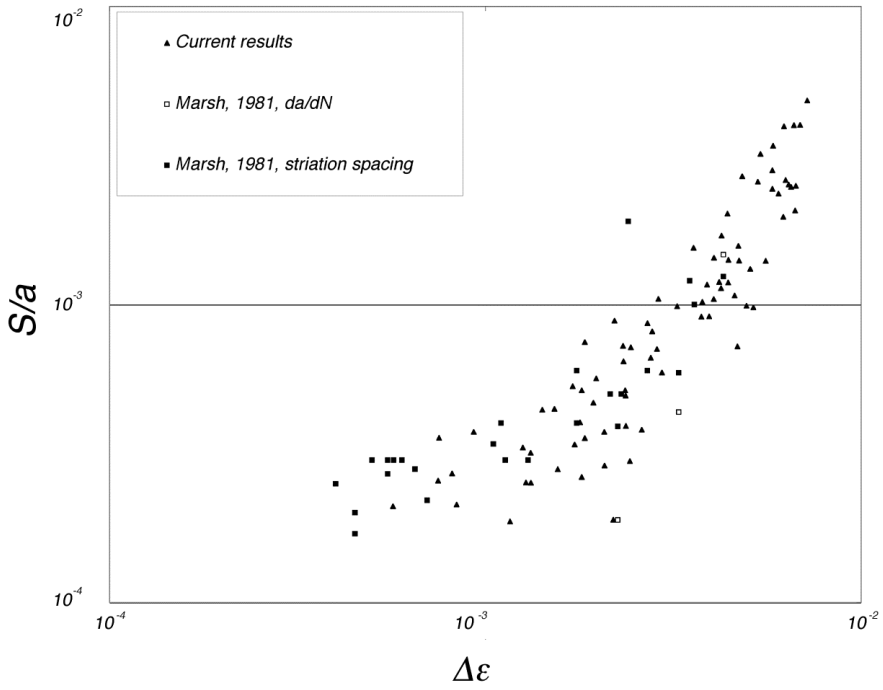

Figure 75. Data from Marsh (1981) and from the present study. Striation spacing divided by the crack length (S/a) is plotted against the strain range (Δε) on a log-log scale to give linear fit for equation 44.

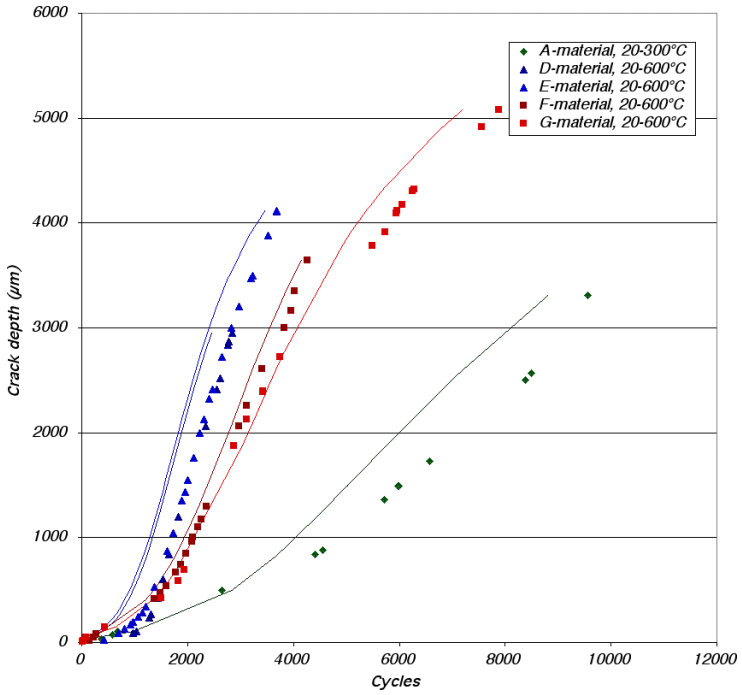

Figure 76. Crack growth measured from striation spacing (dots) and calculated from equation 44 (solid lines) with initial crack size of 50 µm.

The main difference between equations 43 and 44 is the exponent imposed on the crack depth a. In equation 43 the exponent is $m_2/2$, while in equation 44 it is 1. In the case of $m_2=m_7=2$, the two equations are equal.

The a-dependence has also been noticed for high strain mechanical fatigue for different steels (Solomon, 1972; Tomkins, 1981; Skelton, 1993; Skelton et al., 1996; Nisitani et al., 1992). There is some theoretical (Liu & Kobayashi, 1980) and experimental studies (Bates & Clark, 1969), which indicate that m_2=2 in many materials. In published literature (e.g., Boyer, 1986) m_2 values ranging from 2 to 4 are presented. Values quoted for the materials currently studied are typically about 3.

Crack growth in the duplex stainless steels was calculated based on the replica measurements shown in Figure 56. The calculated crack growth data are presented in Figure 77. No correlation with equation 44 can be observed. This is apparently due to the large effect of the phase boundaries on the crack growth rate, which causes the crack growth rate to vary greatly.

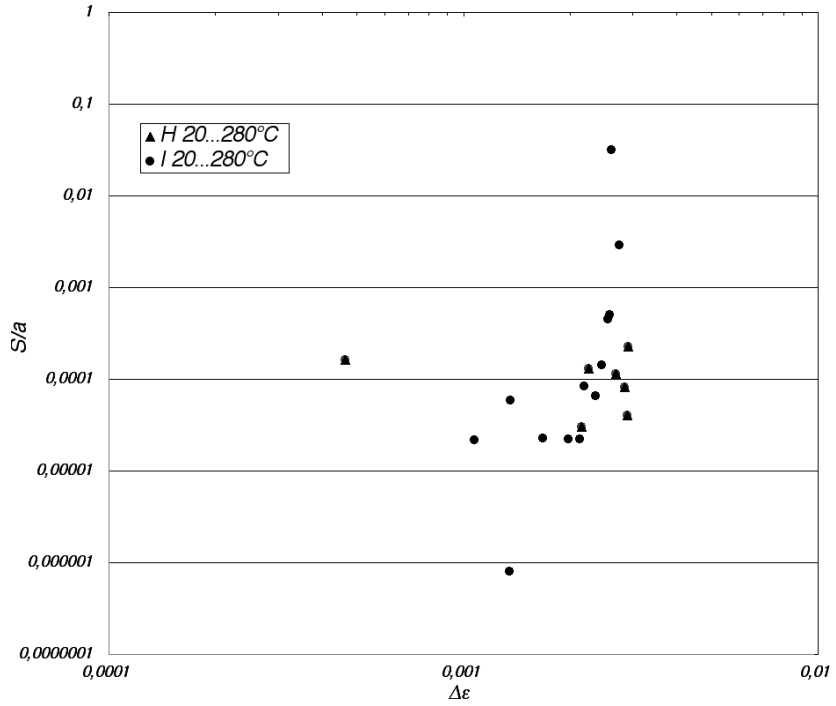

Figure 77. Crack growth rates measured at the sample surface (materials H and I). The crack growth rate estimated from the replica studies divided by the crack length (S/a) is plotted against strain range (Δε) on a log-log scale to give linear fit for equation 44.

5.4 Comparison of thermal and mechanical fatigue

The observed fatigue lives shown in Figure 72 are shorter than those observed for mechanical fatigue (see Figure 17), even when the strains are presented according to the maximum value at the surface. This difference can be attributed to the biaxial stress state and environmental effects, which promote crack initiation and small crack growth at the surface. To compare the present result with S-N plots for mechanical fatigue, the data points shown in Figure 72 were converted to equivalent uniaxial strains

with equations 36 and 37, following the analysis by Marsh (1981) (elastic and plastic strains were calculated according to monotonic yield stress). In Figure 78 the converted points are superimposed on Figure 17. The points from the present study agree with the isothermal 527 – 600°C fatigue and thermal fatigue data for AISI 316L steel.

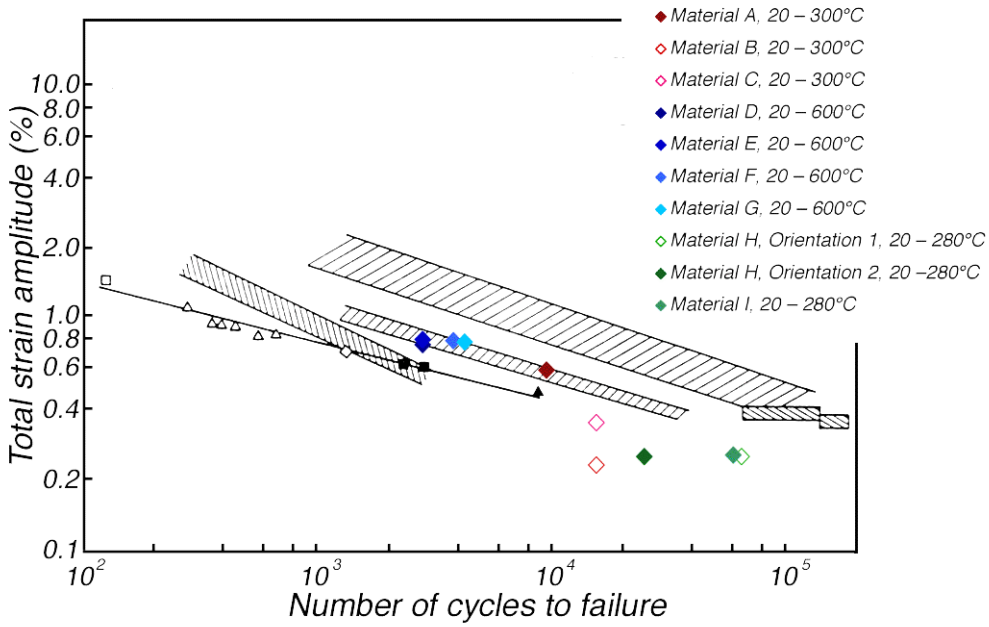

Figure 78. Data points from Figure 72 converted to equivalent uniaxial strains with equations 36 and 37 and superimposed on S-N plot from Petersen & Rubiolo (1991) (Figure 17). Open dots are run-outs.

In the ASME pressure vessel code (1995) the effects of biaxial loading and environment are not explicitly taken into account. To allow for these effects, the ASME design curves include a safety factor of about 2 on strain and 20 on cycles. To assess the sufficiency of these margins in the studied load case, the data is also presented in the ASME curve (Figure 79). It is seen that the data points are correctly predicted failures and that the ASME design curve gives a safe design life, although the remaining safety factor is decreased to about 1.5 on strain.

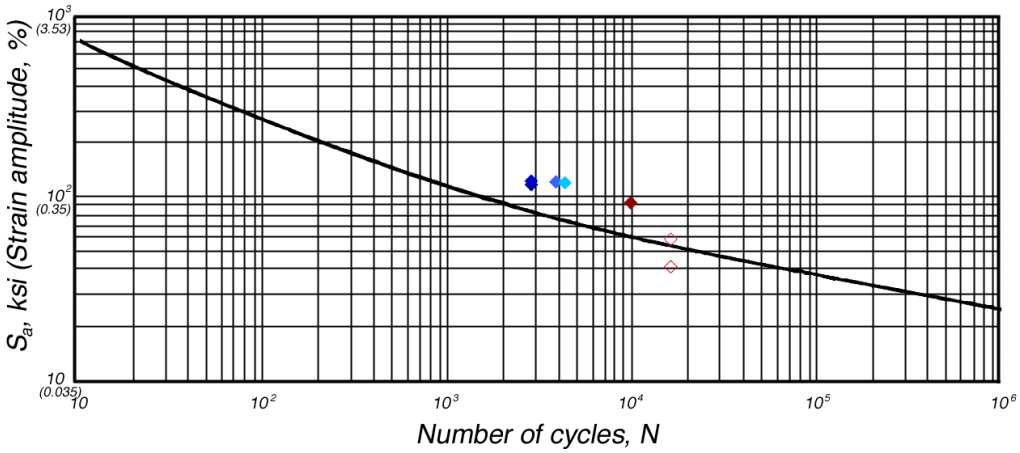

Figure 79. Data points converted from Figure 72 and plotted on the ASME design curve for austenitic stainless steels (the results on duplex stainless steels are not plotted). Material color codes as in figure 78. Open dots are run-outs.

In paragraph 5.3, it was shown that thermal fatigue crack growth can be predicted from the total strain solution of an uncracked specimen and the crack depth using equation 44. In open literature similar models have been shown to be successful in predicting crack growth for mechanical fatigue (Solomon, 1972), high strain fatigue (Skelton et al., 1996), high temperature isothermal fatigue (Taira et al., 1976), and small crack growth (Nisitani et al., 1992; Kawagoishi et al., 2000). As suggested by Nisitani et al. (1992), an equation similar to 44 describes crack growth when the small scale yielding condition of LEFM is violated by high stresses. The similarity in the crack growth models for mechanical and thermal fatigue crack growth indicates that the thermal fatigue crack growth mechanism in the studied regime is similar to the mechanical fatigue crack growth mechanism. If the complex thermal loading is modeled as suggested in paragraph 5.3, the same equation, i.e. equation 44, can be used to predict both thermal and mechanical fatigue crack growth. The similarity seen in crack growth laws for mechanical and thermal fatigue also indicates that the strain-based crack growth model (equation 44) is valid for mechanical fatigue cracks growing in a varying strain and temperature field. Hence, the present results extend the verified range of validity of equation 44.

6 CONCLUSIONS

The following conclusions can be drawn from the studies:

1. The fracture surfaces of thermal fatigue cracks are similar to those of mechanical fatigue.

2. The dislocation structures caused by thermal fatigue differ considerably from those of mechanical fatigue. The width of the X-ray diffraction peaks do not necessarily increase in thermal fatigue loading.

3. The load sharing between the phases in duplex stainless steels is more even in the wrought material than in the cast material due to the different phase morphology.

4. The total strains caused by thermal loading can be approximated with a simple linear-elastic FE-analysis for many geometries and load cases.

5. The ASME (1995) pressure vessel code gives a safe design life for thermal fatigue loading; the remaining safety factor is about 1.5 on strain.

6. The total strain solution for an uncracked geometry can be used to predict the crack growth rate. The crack growth is observed to follow the strain-based crack growth equation:

$$\frac{da}{dN} = C_7 \Delta \varepsilon_{tot}^{m_7} a,$$

where C_7=1.6 and
m_7=1.3 for the studied austenitic materials.

7. Similar crack growth models have been shown to be successful in predicting mechanical fatigue crack growth under various load cases and temperatures. In the present work the model is shown to be successful also for small cracks growing in varying temperature and strain fields.

8. The similitude in the crack growth models for thermal and mechanical fatigue indicates that the crack growth mechanism is similar.

7 REFERENCES

Ahmad, H. Y. & Yates, J. R. 1994. An elastic-plastic model for fatigue crack growth at notches. Fatigue and Fracture of Engineering Materials and Structures, 17 (6), pp. 651 – 660.

Almer, J. D., Cohen, J. B. & Moran, B. 2000. The effects of residual macrostresses and microstresses on fatigue crack initiation. Materials Science and Engineering, A284, pp. 268 – 279.

ANSYS Release 5.5.1.1998.UP19981001.SAP IP Inc.

Armas, A. F., Alvarez-Armas, I. & Petersen, C. 1992. Thermal fatigue behavior and dislocation substructures of 316-type austenitic stainless steels. Jounal of Nuclear Materials, 191 – 194, pp. 672 – 675.

ASME Boiler and Pressure Vessel Code. 1995. Section III, Division 1, Appendix 1. Design stress intensity values, allowable stresses, material properties, and design fatigue curves

Bates, R. C., & Clark, W., G., Jr. 1969. Fractography and fracture mechanics. Transactions of the Americal Society for Metals, 69, pp. 380 – 388.

Behnken, H. & Hauk, V. 1992a. On the influence of microresidual stresses during cyclic loading. Proc. 3rd European Conference on Residual Stresses. Frankfurt-am-Main. Germany. 4 – 6 Nov. DGM Informationsgesellschaft mbH. pp. 733 – 742.

Behnken, H. & Hauk, V. 1992b. X-ray studies on a friction welded duplex steel. Proc. 3rd European Conference on Residual Stresses. Frankfurt-am-Main. Germany. 4 – 6 Nov. DGM Informationsgesellschaft mbH. pp. 165 – 170.

Bichler, Ch. & Pippan, R. 1999. Direct observation of fatigue crack tip deformation in the midsection of a specimen. The seventh international fatigue congress, Fatigue '99, Beijing, P. R. China, June 8 – 12. Beijing institute of aeronautical materials, Institute of metal research, Fatigue society, pp. 2789 – 2794.

Boley, B. & Weiner, J. 1960. Theory of thermal stresses. John Wiley & Sons. 586 p. ISBN 0-486-69579-4

Boyer, H. E. (ed.) 1986. Atlas of Fatigue Curves. American Society for Metals. Metals Park. Ohio, p. 214

Bressers, J., Hurst, R. C., Kerr, D. C., Lamain, L., Sordon, G. & Tartaglia, G.P. 1994. Thermal fatigue crack growth: modelling and experimental verification. Journal of Nuclear Materials, 212 – 215, pp. 448 – 452.

Brown, M. W. & Miller, K. J. 1982. Two decades of progress in the assessment of multiaxial low-cycle fatigue life. In: Low-Cycle Fatigue and Life Prediction, Amzallag, C., Leis, B. N. & Rabbe, P., Eds., ASTM-STP 770, Americal Society for Testing and Materials, pp. 482 – 499.

Chen, J., Takezono, S., Tao, K. & Hazawa, T. 1997. Application of fracture mechanics to the surface crack propagation in strainless steel at elevated temperatures. Acta Materialia, 45 (6), pp. 2495 – 2500.

Cheng, A. S. & Laird, C. 1983. The transition from stage I to stage II fatigue crack propagation in copper single crystals cycled at constant strain amplitudes. Materials Science and Engineering, 60, pp. 177 – 183.

Chopra, O. K. & Gavenda, D. J. 1998. Effects of LWR coolant environments on fatigue lives of austenitic stainless steels. Transactions of the ASME, 120, pp. 116 – 121.

Chopra, O. K. & Muscara, J. 2000. Effects of light water reactor coolant environments on fatigue crack initiation in piping and pressure vessel steels. Proceedings of ICONE8 - 8th International Conference on Nuclear Engineering, April 2-6, Baltimore. ASME. pp. 1 – 12.

Chopra, O. K. & Shack, W. J. 1999. Overview of fatigue crack initiation in carbon and low-alloy steels in light water reactor environments. Journal of Pressure Vessel Technology, American Society for Testing and Materials. 121, pp. 49 – 60.

Coffin, L. F., Wesley, R. P. & Schenectady, N. Y. 1954. Apparatus for study of effects of cyclic thermal stresses on ductile metals. Transactions of the ASME, 76, pp. 923 – 930.

Coffin, L. F. & Schenectady, N. Y. 1954. A study of the effects of cyclic thermal stresses on a ductile metal. Transactions of the ASME, 76, pp. 931 – 950.

Cullity, B. D. 1978. Elements of X-ray Diffraction. 2nd ed. Addison Wesley Publishing Company. 555 p. ISBN 0-201-01174-3.

Davidson, D. L. & Lankford, J. Jr. 1976. Plastic strain distribution at the tips of propagating fatigue cracks. Transactions of the ASME, 98(1), pp. 24 – 29.

Davidson, D. L. & Lankford, J. 1992. Fatigue crack growth in metals and alloys: mechanisms and micromechanics. International Materials Reviews, 37 (2), pp. 45 – 76.

Dean, S. 2000. Chloride SCC of stainless steel? No – cyclic strain cracking. Materials Performance, Sept., pp. 78 – 82.

dell'Erba, D. N., Aliabadi, M. H. 2000. Three-dimensional thermo-mechanical fatigue crack growth using BEM. International Journal of Fatigue, 22, p. 261 – 273.

Degallaix, S., Seddouki, A., Degallaix, G., Kruml, T., Polák, J. 1995. Fatigue damage in austenitic-ferritic duplex stainless steels. Fatigue and Fracture of Engineering Materials and Structures, 18 (1), pp. 65 – 77.

Dowling, N. E. 1976. Geometry effects and the J-integral approach to elastic-plastic fatigue crack growth. In: Cracks and Fracture, ASTM-STP 601, American Society for Testing and Materials, pp. 19 – 32.

Dowling, N. E. 1977. Crack growth during low-cycle fatigue of smooth axial specimens. In: Cyclic Stress-Strain and Plastic Deformation Aspects of Fatigue Crack Growth, ASTM-STP 637, American Society for Testing and Materials, pp. 97 – 121.

Dowling, N. E. & Begley, J. A. 1976. Fatigue crack growth during gross plasticity and the J-integral. In: Mechanics of crack growth, ASTM STP 590, American Society for Testing and Materials, pp. 82 – 103.

Endo, K, Komai, K, Murayama, S. 1983. Influence of Cl^- concentration on corrosion fatigue crack growth of an austenitic stainless steel. Bulletin of the JSME, 26(218), pp. 1281 – 1287.

El Haddad, M. H., Dowling, N. E., Topper, T. H. & Smith, K. N. 1980. J integral applications for short fatigue cracks at notches. International Journal of Fracture, 16 (1), p. 15 – 30.

Elber, W. 1970. The significance of fatigue crack closure. In: Damage Tolerance in Aircraft Structures, ASTM-STP 486, American Society for Testing and Materials, pp. 230 – 242.

Fissolo, A., Marini, B., Nais, G. & Wident, P. 1996. Thermal fatigue behaviour for a 316L type steel. Journal of Nuclear Materials, 233 – 237, pp. 156 – 161.

Fischer, F. D., Rammerstorfer, F. G. & Bauer, F. J. 1990. Fatigue and fracture of high-alloyed steel specimens subjected to purely thermal cycling. Metallurgical Transactions, 21A (4), pp. 935 – 948.

Fischer, F. D., Mayrhofer, K. & Parteder, E. 1996. Elliptical subsurface cracks under a normal stress and a residual stress field. Fatigue and Fracture of Engineering Materials & Structures, 19 (1), pp. 129 – 139.

Ford, F. Prediction of corrosion-fatigue initiation in low-alloy steel and carbon-steel/water systems at 288°C. In: Proceedinngs of the Sixth International Symposium on Environmental Degradation of Materials in Nuclear Power Systems-Water Reactors. Gold, R. E., Simonen, E. P. (Eds.). August 1-5, San Diego, California. The Minerals, Metalss & Materials Society. pp. 9 – 18.

Fritz, R. J. & Schenectady, N. Y. 1954. Evaluation of transient temperatures and stresses. Transactions of the ASME, 76, pp. 913 – 920.

Gabetta, G., Rinaldi, C. & Pozzi, D. 1990. A model for environmetally assisted crack growth rate. In: Environmentally Assisted Cracking: Science and Engineering, Lisagor, W. B., Crooker, T. W. & Leis, B. N. (Eds.), ASTM-STP 1049, American Society for Testing and Materials, pp. 266 – 282.

Gandossi, L. 2000. Crack growth behaviour in austenitic stailess steel components under combined thermal fatigue and creep loading. Doctor of Philosophy thesis. University of Wales, Swansea, 419 p.

Gerland, M, Mendez, J., Violan, P. & Ait Saadi, B. 1989. Evolution of dislocation structures and cyclic behaviour of a 316L-type austenitic stainless steel cycled in vacuo at room temperature. Materials Science and Engineering, A 118, pp. 83 – 95.

Gerland, M., Alain, R., Ait Saadi, B. & Mendez, J. 1997. Low cycle fatigue behaviour in vacuum of a 316L-type austenitic stainless steel between 20 and 600°C – Part II: dislocation structure evolution and correlation with cyclic behaviour. Materials Science and Engineering, A229, pp. 68 – 86.

Goswami, T. 1999. High temperature fatigue – dwell sensitivity and life prediction. Doctor of Technology thesis. Helsinki University of Technology. Laboratory of Engineering Materials. TKK-MTR-5/99. ISBN 951-22-4794-1.

Green, D., Parker, R. & Marsh, D. 1987. Comparison of theoretical estimates and experimental measurements of fatigue crack growth under severe thermal shock conditions – Part II: theoretical assessment and comparison with experiment. Journal of Pressure Vessel Technology, 109, pp. 421 – 427.

Green, D. & Munz, D. 1996. Thermal fatigue crack growth experiments on austenitic steel plates. International Journals of Pressure Vessels & Piping, 65, p. 369 – 378.

Griffith, A. A. 1920. The phenomena of rupture and flow in solids. Philosophical Transactions of the Royal Society of London, 221, pp. 163 – 198.

Haigh, J. R. & Skelton, P. 1978. A strain intensity approach to high temperature fatigue crack growth and failure. Materials Science and Engineering, 36, pp. 133 – 137.

Hatanaka, K., Fujimitsu, T. & Shiraishi, S. 1989. An analysis of surface crack growth in circumferentially grooved components under low-cycle fatigue. JSME International Journal, 32(2), pp. 245 – 255.

Hatanaka, K. 1990. Cyclic stress-strain response and low-cycle fatigue life in metallic materials. JSME International Journal, 33 (1), pp. 13 – 25.

Hayashi, M. 1994. High cycle thermal fatigue crack initiation and growth behavior in the semi-infinite plate model. ASME, PVP, Vol. 287, pp. 49 – 54.

Hayashi, M. 1998a. Thermal fatigue strength of type 304 stainless steel in simulated BWR environment. Nuclear Engineering and Design, 184, pp. 135 – 144.

Hayashi, M. 1998b. Thermal fatigue behavior of thin walled cylindrical carbon steel specimens in simulted BWR environment. Nuclear Engineering and Design, 184, pp. 123 – 133.

Hayashi, M., Enomoto, K., Saito, T. & Miyagawa, T. 1998. Development of thermal fatigue testing apparatus with BWR water environment and thermal fatigue strength of austenitic stainless steels. Nuclear Engineering and Design, 184, pp. 113 – 122.

Higuchi, M. & Iida, K. 1991. Fatigue strength correction factors for carbon and low-alloy steels in oxygen-containing high-temperature water. Nuclear Engineering and Design, 129, pp. 293 – 306.

Hirano, A., Hayashi, M., Sagawa, W., Takehara, H., Tanaka, M. & Iikura, T. 1994. High cycle thermal fatigue crack initiation behavior of type 304 stainless steel in pure water. ASME, PVP, Vol. 287, pp. 19 – 25.

Hirano, K., Kobayashi, H. & Nakazawa, H. 1979. Elastic-plastic fracture mechanics study of thermal shock cracking. ICM 3 – Mechanical Behavior of Materials, Vol. 3, Cambridge, England, 20 – 24 Aug., Pergamon Press Ltd., pp. 457 – 466.

Hishida, M., Saito, M., Hasegawa, K., Enomoto, K., Matsuo, Y. 1986. Experimental study on crack growth behavior for austenitic stainless steel in high temperature pure water. Transactions of the ASME, 108, pp. 226 – 233.

Hoshide, T., Yamada, T., Fujimura, S. & Hayashi, T. 1985. Short crack growth and life prediction in low-cycle fatigue of smooth specimens. Engineering Fracture Mechanics, 21 (1), pp. 85 – 101.

Hussain, K. 1997. Short fatigue crack behaviour and analytical models: a review. Engineering Fracture Mechanics, 58 (4), pp. 327 – 354.

Hutchinson, J. W. 1968. Singular behavior at the end of a tensile crack in a hardening material. Journal of the Mechanics and Physics of Solids, 16, pp. 13 – 31.

Hänninen, H. & Hakala, J. 1981. Pipe failure caused by thermal loading in BWR water conditions. International Journal of Pressure Vessels & Piping, 9, pp. 445 – 455.

Hänninen, H., Törrönen, K. & Cullen, W. H. 1986. Comparison of proposed cyclic crack growth mechanisms of low alloy steels in LWR environments. Poceedings of the 2nd International Atomic Energy Agency Specialists' Meeting on Subcritical Crack Growth, NUREG/CP-0067, MEA-2090, 2, pp. 73 – 97.

Igari, T., Wada, H. & Ueta, M. 2000. Mechanism-based evaluation of thermal ratchetting due to traveling temperature distribution. Transactions of the ASME, 122, pp. 130 – 138.

Ilola, R. 1999. Effect of temperature on mechanical properties of austenitic high nitrogen steels. Doctor of Technology thesis. Acta Polytechnica Scandinavica, Mechanical Engineering Series, 136. 100 p.

Inal, K. Gergaud, P., François, M. & Lebrun, J. L. 1999. Stress analysis in a duplex steel. Scandinavian Journal of Metallurgy, 28, pp. 139 – 150.

Irwin, G. R. 1947. Fracture dynamics. In: Fracturing of Metals. A Seminar on the Fracturing of Metals. American Society for Metals, Ohio. pp. 147 – 166.

Irwin, G. R. 1957. Analysis of stresses and strains near the end of a crack traversing a plate. Journal of Applied Mechanics, 24, pp. 361 – 364.

Itoh, T., Chen, X., Nakagawa, T. & Sakane, M. 2000. A simple model for stable cyclic stress-strain relationship of type 304 stainless steel under nonproportional loading. Journal of Engineering Materials and Technology, 122, pp. 1 – 9.

Itoh, T., Sakane, M., Ohnami, M. & Socie, D. 1995. Nonproportional low cycle fatigue criterion for type 304 stainless steel. Journal of Engineering Materials and Technology, 117, pp. 285 – 292.

Jenkins, C. F. & Smith, G. V. 1969. Serrated plastic flow in austenitic stainless steel. Transactions of the Metallurgical Society of AIME, 245, 2149 – 2156.

Jin, Z.-H. & Noda, N. 1994. Transient thermal stress intensity factors for a crack in a semi-infinite plate of a functionally gradient material. International Journal of Solids & Structures, 3(2), pp. 203 – 218.

Johansson, J., Odén, M. & Zeng, X.-H. 1999. Evolution of the residual stress state in a duplex stainless steel during loading. Acta Materialia, 47(9), pp. 2669 – 2684.

Johansson, J. & Odén, M. 2000a. Load sharing between austenite and ferrite in duplex stainless steel during cyclic loading. Metallurgical and Materials Transactions, 31A (6), pp. 1557 – 1570.

Johansson, J, & Oden, M. 2000b. Influence of texture and anisotropy on microstresses and flow behavior in a duplex stainless steel during loading. The 49th annual Denver X-ray Conference, 31 July- 4 August 2000, Denver, Colorado, USA.

John, R., Hartman, G. A. & Gallagher, J. P. 1992. Crack growth induced by thermal-mechanical loading. Experimental Mechanics, June, pp. 102 – 108.

Kamachi, K., Okada, T., Kawano, M., Namba, S. Ishida, T., Tani, N. & Kubohori, T. 1982. Thermal fatigue by impact heating and stresses of two phase stainless steel at elevated temperature. Proc. 4th Int. Conf. on Composite Materials: Progress in Science and Engineering of Composites, Tokyo, pp. 1383 – 1389.

Kawagoishi, N., Chen, Q. & Nisitani, H. 2000. Significance of small crack growth law and its practical application. Metallurgical and Materials Transactions, 31A, pp. 2005 – 2013.

Kawakubo, T., Hishid, M., Amano, K., Katsuta, M. 1980, Crack growth behavior of type 304 stainless steel in oxygenated 290°C pure water under low frequency cyclic loading. Corrosion-NACE, 36(11), pp. 638 – 647.

Keiser, J., Taljat, B., Wang, X.-L., Maziasz, P., Hubbard, C. & Swindeman, R. 1996. Analysis of composite tube cracking in recovery boiler floors. 1996 Engineering Conference, TAPPI Proceedings, pp. 693 – 705.

Keiser, J., Taljat, B., Wang, X.-L., Swindeman, R., Maziasz, P., Thomas, R. & Payzant, E. 1997. Analysis of cracking of co-extruded recovery boiler floor tubes. 1997 Engineering & Papermakers conference. TAPPI Proceedings, pp. 1025 – 1041.

Kemppainen, M. 1997. Termisen väsymisen testausjärjestelmän suunnittelu ja toteutus. Diplomityö. Espoo, Teknillinen korkeakoulu, Konetekniikan osasto, Materiaalitekniikan laboratorio. 110 p. In Finnish.

Kerezsi, B. B., Kotousov, A. G. & Price, J. W. H. 2000. Experimental apparatus for thermal shock fatigue investigations. International Journal of Pressure Vessels and Piping, 77, pp. 425 – 434.

Kliman, V. 1983. Fatigue life prediction for a material under programmable loading using the cyclic stress-strain properties. Materials Science and Engineering, 68, pp. 1 – 10.

Kruml, T., Polák, J., Obrtlík, K. & Degallaix, S. 1997. Dislocation structures in the bands of localised cyclic plastic strain in austenitic 316L and austenitic-ferritic duplex stainless steels. Acta Materialia, 45 (12), pp. 5145 – 5151.

Kuo, A.-Y. & John, R. 1992. Analytical and experimental treatment of a single-edge-crack plate subjected to arbitrary point heat sources. In: Fracture Mechanics: Twenty Second Symposium. Eds.: Ernst, H. A., Saxena, A. & McDowell, D. L. ASTM-STP 1131. American Society for Testing and Materials. Philadelphia, pp. 342 – 366.

Laird, C. & de la Veaux, R. 1977. Additional evidence for the plastic blunting process of fatigue crack propagation. Metallurgical Transactions, 8A (4), pp. 657 – 664.

Laird, C. & Smith, G. C. 1962. Crack propagation in high stress fatigue. Philosophical Magazine, 7(77), pp. 847 – 857.

Lal, D. 1994. A new mechanistic approach to analyzing LEFM fatigue crack growth behaviour of metals and alloys. Engineering Fracture Mechanics, 47 (3), pp. 379 – 401.

Lankford, J., Davidson, D. L. & Chan, K. S. 1984. The influence of crack tip plasticity in the growth of small fatigue cracks. Metallurgical Transactions, 15A (8), pp. 1579 – 1588.

Lanteigne, J. & Baïlon, J-P. 1981. Theoretical model for FCGR near the threshold. Metallurgical Transactions, 12A (3), pp. 459 – 466.

Leis, B. N. 1985. Displacement controlled fatigue crack growth in inelastic notch fields: implications for short cracks. Engineering Fracture Mechanics, 22 (2), pp. 279 – 293.

Li, Y. & Laird, C. 1994. Cyclic response and dislocation structures of AISI 316L stainless steel. Part 2: polycrystals fatigued at intermediate strain amplitude. Materials Science and Engineering, A186, pp. 87 – 103.

Lindgren, M. & Lepistö, T. 2000a. Effect of prior plastic deformation on the relation between residual stresses and Barkhausen noise. The sixth international conference on residual stresses ICRS-6, Oxford, UK, July 10 – 12 2000. pp. 853 – 860. ISBN-I-86125-123-8

Lindgren, M. & Lepistö, T. 2000b. Application of a novel type Barkhausen noise sensor to continuous fatigue monitoring. NDT&E International, 33, pp. 423 – 428.

Liu, H. W. & Kobayashi, H. 1980. Stretch zone width and striation spacings – the comparison of theories and experiments. Scripta Metallurgica, 14, pp. 525 – 530.

Lukáš, P. & Kunz, L. 1984. Threshold stress intensity and dislocation structures surrounding fatigue cracks in polycrystalline copper. Materials Science and Engineering, 62, pp. 149 – 157.

Lukáš, P., Kunz, L. & Knésl, Z. 1985. Fatigue crack propagation rate and the crack tip plastic strain amplitude in polycrystalline copper. Materials Science and Engineering, 70, pp. 91 – 100.

Maier, H. J. & Christ, H.-J. 1996. Modelling of cyclic stress-strain behavior under thermomechanical fatigue conditions – a new approach based upon a multi-component model. Scripta Materialia, 34 (4), pp. 609 – 615.

Maier, H. J. & Christ, H.-J. 1997. Modelling of cyclic stress-strain behavior and damage mechanisms under thermomechanical fatigue conditions. International Journal of Fatigue. 19 (1), pp. S267 – S274.

Mallet, O., Engler-Pinto, C. C.Jr, Rézaï-Aria, F., Skelton, R. P., Nikbin, K. & Webster, G. A. 1995. Influence of material stress-strain characteristics on thermomechanical fatigue analysis of IN100 superalloy. Materials at High Temperatures, 13 (1), pp. 47 – 54.

Marsh, D. J. 1981. A thermal shock fatigue study of type 304 and 316 stainless steels. Fatigue of Engineering Materials and Structures, 4 (2), pp. 179 – 195.

Marsh, D., Green, D. & Parker, R. 1986. Comparison of theoretical estimates and experimental measurements of fatigue crack growth under severe thermal shock conditions – Part I: experimental observations. Journal of Pressure Vessel Technology, 108, pp. 501 – 506.

McCormick, P. G. 1972. A model for the Portevin – Le Chatelier effect in substitutional alloys. Acta Metallurgica, 20, pp. 351 – 354.

McDowell, D. 1987. Simple experimentally motivated cyclic plasticity model. Journal of Engineering Mechanics, 113 (3).

McEvily, A. J. & Wei, R. P. 1971. Fracture mechanics and corrosion fatigue. NACE-2, Corrosion Fatigue: Chemistry, Mechanics and Microstructure, Devereux, O., McEvily, A. J. & Staehle, R. W. (Eds.) University of Connecticut, June 14 – 18, pp. 381 – 395. ISBN 915567-58-X

Merola, M. 1995. Normative issue in thermal fatigue design of nuclear components. Nuclear Engineering and Design, 158, pp. 351 – 361.

Miller, K. J. 1999. A historical perspective of the important parameters of metal fatigue; and problems for the next century. Proceedings of the seventh international fatigue congress, Fatigue '99, Beijing, P. R. China, June 8 – 12 1999. Beijing Institute of Aeronautical Materials, Institute of Metal Research, Fatigue Society, pp. 15 – 39.

Moverare, J. J. 2001. Microstresses and anisotropic mechanical behaviour of duplex stainless steels. Linköpings Universitet, Institute of Technology, Department of Mechanical Engineering, Division of Engineering Materials. Dissertations No. 699. 135 p. ISBN 91-7373-043-2.

Mughrabi, H. 1993. Cyclic plasticity and fatigue of metals. Journal de Physique IV, 3, pp. 659 – 668.

Mughrabi, H. 1996. Cyclic stress-strain behaviour, microstructure and fatigue life. Fatigue '96: Proceedings of the sixth international fatigue congress, 6 – 10 May, Berlin, Germany. pp. 57 – 68.

Mughrabi, H. & Christ, H.-J. 1997. Cyclic deformation and fatigue of selected ferritic and austenitic steels: specific aspects. ISIJ International, 37 (129), pp. 1154 – 1169.

Murakami, Y. (ed.). 1987. Stress intensity factors handbook. Pergamon Press. ISBN 0-08-034809-2.

Murakami, Y., Endo, M. 1993. Effects of defects, inclusions and inhomogeneities on fatigue strength. International Journal of Fatigue, 16 (4), pp. 163 – 182.

Murakami, Y., Toriyama, T & Coudert, E. M. 1994. Instructions for a new method of inclusion rating and correlations with the fatigue limit. Journal of Testing and Evaluation, 22 (4), pp. 318 – 326.

Muralidharan, U. & Manson, S. S. 1988. A modified universal slopes equation for estimation of fatigue characteristics of metals. Journal of Engineering Materials and Technology, 110, pp. 55 – 62.

Navarro, A. & de los Rios, E. R. 1988. Short and long fatigue crack growth: a unified model. Philosophical Magazine A, 57 (1), pp. 15 – 36.

Neumann, P. 1969. Coarse slip model of fatigue. Acta Metallurgica, 17, pp. 1219 – 1225.

Nilsson, J.-O. & Thorvaldsson, T. 1985. The influence of nitrogen on microstructure and strength of a high-alloy austenitic stainless steel. Scandinavian Journal of Metallurgy, 15, pp. 83 – 89.

Nisitani, H., Goto, M. & Kawagoishi, N. 1992. A small-crack growth law and its related phenomena. Engineering Fracture Mechanics, 41 (4), pp. 499 – 513.

Ohno, N. & Kachi, Y. 1986. A constutive model of cyclic plasticity for nonlinear hardening materials. Journal of Applied Mechanics, 53, pp. 395 – 402.

Ogava, K. Ueta, M. Kanaoka, T. Kitade, S, Ueno, T. & Takashi, S. 1991 Applicability of simplified estimation method to thermal ratchetting of FBR component. Transaction of the 11th international conference on structural mechanics in reactor technology. H Shibata (ed.) Atomic Energy Society of Japan, Tokyo. Vol. E, pp. 209 – 214.

Orbtlík, K., Kruml, T. & Polák, J. 1994. Dislocation structures in 316L stainless steel cycled with plastic strain amplitudes over a wide interval. Materials Science and Engineering, A187, pp. 1 – 9.

Paris, P., Gomez, M. & Anderson, W. 1961. A rational analytic theory of fatigue. The Trend in Engineering, 13 (1), pp. 9 – 14.

Paris, P. & Erdogan, F. 1963. A critical analysis of crack propagation laws. Transacions of the ASME. Journal of Basic Engineering, 85(4), pp. 528 – 534.

Pelloux, R. M. N. 1969. Mechanisms of formation of ductile fatigue striations. Transactions of American Society for Metals, 62, pp. 281 – 285.

Petersen, C. & Rubiolo, G. H. 1991. High-temperature thermal fatigue of AISI 316L steel. Journal of Nuclear Materials, 179 – 181, pp. 488 – 491.

Pippan, R., Berger, M. & Stüwe, H. P. 1986. The influence of crack length on fatigue crack growth in deep sharp notches. Metallurgical Transactions, 18A (3), pp. 429 – 435.

Pohl, M. & Bracke, A. 1997. The influence of changing the microstructure on the plastic deformation of duplex stainless steels after thermal cycling. Duplex Stainless Steels 97 – 5th World Conference. The Netherlands, 21 –

23 October. Stainless Steel World. KCI Publishing, pp. 891 – 896. ISBN 90-73168-02-3.

Pohl, M. & Bracke, A. 1999. Thermisch induzierte Veränderungen der Mikrostruktur ferritisch-austenitischer Duplex-Stähle und deren Einfluß auf den Eigenspannungszustand. Z. Metallkd., 90 (8), pp. 551 – 556

Polák, J., Kruml, T., Degallaix, S., Nilsson, J.-O. 1999. Fatigue damage in austenitic-ferritic duplex stainless steel. ICM8 – Eigth International Conference on the Mechanical Behaviour of Materials, Victoria, British Columbia, Canada, 16 – 21 May, Vol. I.2, pp. 47 – 52. ISBN 1-55058-163-5

Prime, M. 2001. Cross-sectional mapping of residual stresses by measuring the surface contour after a cut. Submitted for publication in Journal of Engineering Materials and Technology.

Prime, M. B. & Gonzales, R. 2000. The contour method: simple 2-D mapping of residual stresses. The sixth international conference on residual stresses ICRS-6, Oxford, UK, July 10 – 12, 2000. pp. 617 – 624. ISBN-I-86125-123-8.

Rajanna, K., Pathiraj, B. & Kolster, B.H. 1997. Duplex stainless steel fracture surface analysis using X-ray fractography. Journal of Materials Engineering and Performance, 6 (1), pp. 35 – 40.

Revel, P., Kircher, D. & Bogard, V. 2000. Experimental and numerical simulation of a stainless steel coating subjected to thermal fatigue. Materials Science and Engineering, A290, pp. 25 – 32.

Rice, J. R. 1967. Mechanics of crack tip deformation and extension by fatigue. In: Fatigue Crack Propagation, ASTM-STP 415, American Society for Testing and Materials, pp. 247 – 311.

Rice, J. R. 1968. A path independent integral and the approximate analysis of strain concentration by notches and cracks. Journal of Applied Mechanics, 35, pp. 379 – 386.

Rice, J. R. & Rosengren, G. F. 1968. Plane strain deformation near a crack tip in a power-law hardening material. Journal of the Mechanics and Physics of Solids, 16, pp. 1 – 12.

Saarinen, P., Nenonen, P. & Hänninen, H. 2000. Thermal fatigue of new composite tube materials. Proceedings of TAPPI 2000 Engineering Conference, Atlanta Hilton & Towers, Atlanta, Sept. 17 – 21.(CD-ROM)

Sadananda, K. & Vasudevan, A. K. 1995. Analysis of fatigue crack closure and thresholds. In: Fracture Mechanics: 25th Volume, ASTM-STP 1220.

Ed.: Erdogan, F. American Society for Testing and Materials, pp. 484 – 501.

Sadananda, K. & Vasudevan, A. K. 1997a. Analysis of high temperature fatigue crack growth behavior. International Journal of Fatigue, 19 (1), pp. S183 – S189.

Sadananda, K. & Vasudevan, A. K. 1997b. Short crack growth behavior. In: Fatigue and Fracture Mechanics: 27th volume. Eds.: Piascik, R. S., Newman, J. C. & Dowling, N. E. ASTM-STP 1296. American Society for Testing and Materials, pp. 301 – 316.

Shi, H. J. & Pluvinge, G. 1994. Cyclic stress-strain response during isothermal and thermomechanical fatigue. Fatigue, 16, pp. 549 – 557.

Shi, H. J., Wang, Z., G. & Su, H. H. 1996. Thermomechanical fatigue of a 316L austenitic steel at two different temperature intervals. Scripta Materialia, 35 (9), pp. 1107 – 1113.

Siegmund, T., Werner, E. & Fischer, F. D. 1993. The irreversible deformation of a duplex stainless steel under thermal cycling. Materials Science and Engineering, A169, pp. 125 – 134.

Siegmund, T., Werner, E. & Fischer, F. D. 1995. On the thermomechanical deformation behavior of duplex-type materials. Journal of the Mechanics and Physics of Solids, 43 (4), pp. 495 – 532.

Silberschmidt, V. V., Werner, E. 1999. Analysis of thermal residual stresses in duplex-type materials. Computational Materials Science, 16, pp. 39 – 52.

Skelton, R. P. 1982. Growth of short cracks during high strain fatigue and thermal cycling. In: Low Cycle Fatigue and Life Prediction. ASTM-STP 770. Philadelphia, pp. 337 – 381.

Skelton, R. P. 1993. Cyclic hardening, softening, and crack growth during high temperature fatigue. Materials Science and Technology, 9, pp. 1001 – 1008.

Skelton, R. P., Vilhelmsen, T. & Webster, G. A. 1998. Energy criteria and cumulative damage during fatigue crack growth. International Journal of Fatigue, 20 (9), p. 641.

Skelton, R. P., Webster, G. A. 1996. History effects on the cyclic stress-strain response of a polycrystalline and single crystal nickel-base superalloy. Materials Science and Engineering, A216, pp. 139 – 154.

Skelton, R. P., Rees, C. J. & Webster, G. A. 1996. Energy damage summation methods for crack initiation and growth during block loading

in high temperature low-cycle fatigue. Fatigue and Fracture of Engineering Materials and Structures, 19 (23), pp. 287 – 297.

Socie, D. 1987. Multiaxial fatigue damage models. Journal of Engineering Materials and Technology, 109, pp. 293 – 298.

Socie, D. & Bannantine, J. 1988. Bulk deformation fatigue damage models. Materials Science and Engineering, A103, pp. 3 – 13.

Socie, D. F. & Marquis, G. B. 2000. Multiaxial fatigue. Society of Automotive Engineers. Warrendale, U.S.A. 484 p. ISBN 0-7680-0453-5

Solomon, H. D. 1972. Low cycle fatigue crack propagation in 1081 steel. Journal of Materials, JMLSA, 7 (3), pp. 299 – 306

Spindler, M. W. 1998. Thermal mechanical cyclic stress-strain testing of a type 316 steel. In: Allison, A. (ed.). Experimental Mechanics: Advances in Design, Testing and Analysis. Balkema. Rotterdam. ISBN:90-5809-016-7, pp. 1127 – 1132.

Srinivasan, V. S., Sandhya, R., Valsan, M., Bhanu Sankara Rao, K., Mannan, S. L. & Sastry, D. H. 1997. The influence of dynamic strain ageing on stress response and strain-life relationship in low cycle fatigue of 316L(N) stainless steel. Scripta Materialia, 37 (10), pp. 1593 – 1598.

Starkey, M. S. & Skelton, R. P. 1982. Strain intensity and cyclic J approaches to crack growth. Fatigue of Engineering Materials and Structures, 5 (4), pp. 329 – 341.

Stefanita, C.-G., Atherton, D. L. & Clapham, L. 2000. Plastic versus elastic deformation effects on magnetic Barkhausen noise in steel. Acta Materialia, 48, pp. 3545 – 3551.

Stevens, K. J. 1999. Fatigue performance and microanalysis of heat treated 2205 duplex stainless steel. Materials Science and Technology, 15, pp. 903 – 908.

Suresh, S. 1992. Fatigue of materials. Cambridge Solid State Science Series. Cambridge University Press. 617 p. ISBN 0-521-437-63-6.

Taira, S. 1973. Relationship between thermal fatigue and low-cycle fatigue at elevated temperature. In: Fatigue at Elevated Temperatures, ASTM-STP 520, American Society for Testing and Materials. pp. 80-101.

Taira, S. & Fujino, M. 1979. A damage analysis in high temperature thermal fatigue. Transactions of the Iron and Steel Institute of Japan, 19 (3), pp. 185 – 190

Taira, S., Maruyama, S. & Fujino, M. 1976. Effect of temperature on the rate of fatigue crack propagation in steels during low cycle fatigue. Transactions of the Iron and Steel Institute of Japan, 16 (3), pp. 146 – 152

Tanaka, K., Masuda, C. & Nishijima, S. 1981. The generalized relationship between the parameters C and m of Paris' law for fatigue crack growth. Scripta Metallurgica, 15, pp. 259 – 264.

Tanaka, K. 1989. Mechanics and micromechanics of fatigue crack propagation. In: Fracture Mechanics: Perspectives and Directions, Twentieth Symposium. Eds.: Wei, R. P. & Gangloff, R. P. ASTM-STP 1020. American Society for Testing and Mateirals. Philadelphia, pp. 151 – 183.

Tanigawa, Y. & Komatsubara, Y. 1997. Thermal stress analysis of a rectangular plate and its thermal stress intensity factor for compressive stress field. Journal of Thermal Stresses, 20, pp. 517 – 542.

Tidball, R. A. & Shrut, M. M. 1954. Thermal-shocking austenitic stainless steel with molten metals. Transactions of the ASME, 76, pp. 639 – 643.

Tomkins, B. 1968. Fatigue crack propagation – an analysis. Philosophical Magazine, 18, pp. 1041 – 1066.

Tomkins, B. 1980. Micromechanisms of fatigue crack growth at high stress. Metal Science, 14 (8-9), pp. 408 – 417.

Tomkins, B. 1981. High strain fatigue. In: Subcritical Crack Growth due to Fatigue, Corrosion and Creep, Ispra, Italy, 19 – 23 Oct., Elsevier Science Publishing Co., Inc., pp. 239 – 266.

Tomkins, B, 1983a. Fatigue: mechanisms. In: Creep and Fatigue in High-Temperature Alloys, Applied Science Publishers, Ltd., pp. 111 – 143.

Tomkins, B. 1983b. Life prediction at elevated temperature. Journal of Pressure Vessel Technology, 105, pp. 269 – 272.

Tomkins, B. 1984. Crack growth – present status, future direction. Fatigue Crack Growth: 30 Years of Progress, Cambridge, UK, 20 Sept, pp. 133 – 146.

Uchida, Y., Shimojo, M. & Higo, Y. 1999. Relationship between fatigue striation height and stress ratio. Journal of Materials Science, 24, pp. 2411 – 2419.

Vasudevan, A. K., Sadananda, K. & Louat, N. 1992. Reconsideration of fatigue crack closure. Scripta Metallurgica et Materialia, 27, pp. 1673 – 1678.

Vasudevan, A. K., Sadananda, K. & Louat, N. 1993. Two critical stress intensities for threshold fatigue crack propagation. Scripta Metallurgica et Materialia, 28, pp. 65 – 70.

Vasudevan, A. K. & Sadananda, K. 1993. Fatigue crack growth in metal matrix composites. Scripta Metallurgica et Materialia, 28, pp. 837 – 842.

Vasudevan, A. K. & Sadananda, K. 1995a Classification of fatigue crack growth behavior. Metallurgical and Materials Transactions, 26A (5), pp. 1221 – 1234.

Vasudevan, A. K. & Sadananda, K. 1995b Fatigue crack growth behavior of composites. Metallurgical and Materials Transactions, 26A (12), pp. 3199 – 3210.

Vehoff, H. & Neumann, P. 1978. In situ SEM experiments concerning the mechanism of ductile crack growth. Acta Metallurgica, 27, pp. 915 – 920.

Wadsworth, N. J., Hutchings, J. 1958. The effect of atmospheric corrosion on metal fatigue. Philosophical Magazine, 3, pp. 1154 – 1166.

Wang, X.-L., Hoffman, C. M., Hsueh, C. H., Sarma, G. & Hubbard, C. R. 1999. Influence of residual stress on thermal expansion behavior. Applied Physics Letters, 75(21), pp. 3294 – 3296.

Wareing, J., Tomkins, B. & Sumner, G. 1973. Extent to which material properties control fatigue failure at elevated temperatures. In: Fatigue at Elevated Temperatures, ASTM-STP 520, American Society for Testing and Materials, pp. 123 – 137

Wegst, C. W. 1995. Stahlschlüssel. Verlag Stahlschlüssel Wegst GmbH. Germany.

Westergaard, H. M. 1939. Bearing pressure and cracks. Journal of Applied Mechanics, 6, pp. 49 – 53.

Williams, D. R., Davidson, D. L. & Lankford, J. 1980. Fatigue-crack-tip plastic strains by the stereoimaging technique. Experimental Mechanics, 22, pp. 134 – 139.

Wilson, W. K. & Yu, I.-W. 1979. The use of the J-integral in thermal stress crack problems. International Journal of Fracture, 15 (4), pp. 377 – 387.

Xia, Y. & Wang, Z. 1992. Low cycle fatigue behaviour of a new type of stainless steel. Materials Science and Engineering, A151, pp. 29 – 35.

Yoshimoto, T., Ishihara, S., Goshima, T., McEvily, A. J. & Ishizaki, T. 1999. An improved method for the determination of the maximum

thermal stress induced during a quench test. Scripta Materialia, 41 (5), pp. 553 – 559.

You, B.-R. & Lee, S.-B. 1996. A critical review on multiaxial fatigue assessment of metals. International Journal of Fatigue, 18(4), pp. 235 – 244.

Zamrik, S. Y. 1990. An interpretation of axial creep-fatigue damage interaction in type 316 stainless steel. Transactions of the ASME, 2, pp. 4 – 19.

Zauter, R., Christ, H. J., Mughrabi, H. & Petry, F. 1993. Thermomechanical fatigue of the austenitic stainless steel AISI 304L. Thermomechanical Fatigue Behavior of Materials, San Diego, USA, 14-16 Oct. American Society for Testing and Materials. ASTM-STP 1186. pp. 70-90.

Zauter, R., Christ, H. J. & Mughrabi, H. 1994. Some aspects of thermomechanical fatigue of AISI 304 L stainless steel: Part II. Dislocation arrangements. Metallurgical and Materials Transactions, 25A (2), pp. 401 – 406.

Zhang, P. & Burger, C. P. 1986. Transient thermal stress-intensity factors for short edge cracks with equal depth of crack tips. Engineering Fracture Mechanics, 24 (4), pp. 589 – 599.

APPENDIX 1. TWO-BAR MODEL FOR THERMAL STRESSES

The thermal strains and stresses caused by rapid temperature changes and internal constraint can be very complicated. A simple two-bar model can be used to illustrate qualitatively the effect of a thermal cycle.

Consider a situation where two bars are constrained so, that their strains are forced equal (Figure A1.1). The thinner Bar 1 simulates the sample surface, whereas the thicker Bar 2 simulates the bulk of the material. Both bars are from the same linear elastic – ideally plastic material.

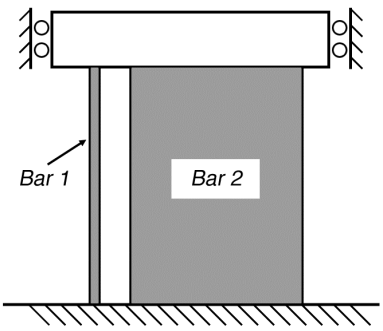

Figure A1.1 Two bars are forced to equal strain.

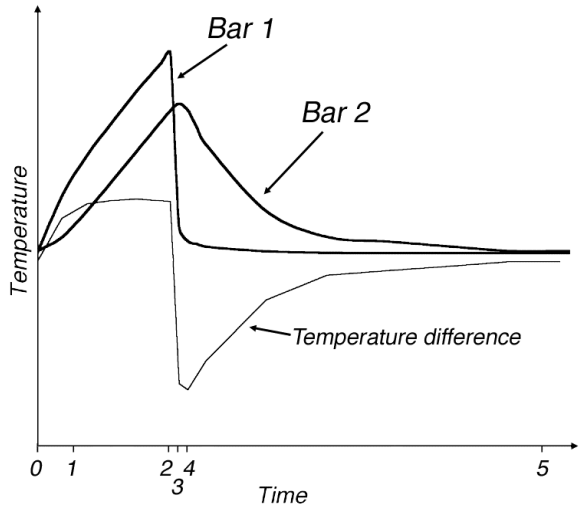

Figure A1.2 The temperature in Bar 1 simulates the quick transient of the specimen surface, whereas the temperature curve of Bar 2 simulates the temperature deeper in the specimen.

Consider now the system going through a thermal cycle each bar following the corresponding temperature curve in Figure A1.2. The temperature curve of Bar 1 simulates the rapid transients experienced by the surface, whereas the curve of Bar 2 simulates the slower heating and cooling, that takes place deeper in the material. A qualitative stress-strain plot can now be drawn for the two bars (Figure A1.3).

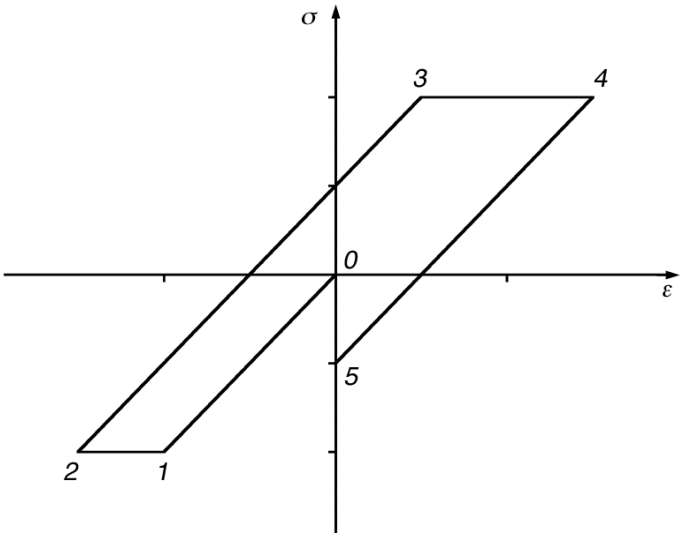

Figure A1.3. Schematic stress-strain plot for Bar 1 during thermal cycle of the system. See text for details.

The development of the stress-strain plot can be divided into 6 distinct phases, as follows:

0) The heating starts. The temperature of Bar 1 increases faster than temperature of Bar 2. Consequently the thermal expansion causes compressive stress to develop into Bar 1 and a balancing tensile stress into Bar 2. Because of the greater thickness of Bar 2 the stresses in Bar 2 are much smaller than those in Bar 1

1) The yield point is exceeded in Bar 1. Bar 1 starts to deform plastically, whereas Bar 2 continues to deform elastically. The uneven plastic deformation induces a mismatch between the two bars.

2) The cooling starts. Rapid cooling changes the stress in Bar 1 from compressive to highly tensile.

3) Yielding starts in tension in Bar 2. Again the uneven plastic deformation induces a mismatch between the two bars.

4) The temperature difference between the bars begins to decrease again as Bar 2 slowly cools down.

5) Finally, the temperature in Bar 1 and 2 is equal again. Due to the yielding in tension in phase 3 in Bar 1 there is a compressive residual stress present in Bar 1 and a balancing tensile residual stress in Bar 2.

APPENDIX 2. DERIVATION OF EQUATION 41

Equation 41 was used to calculate the applied strains from the measured temperature and measured axial strain data (paragraph 3.3). The equation can be derived as follows: in an unconstrained case an increase in temperature gives rise to thermal expansion proportional to the temperature change:

$$\varepsilon_T = \alpha \cdot \Delta T, \tag{A2.1}$$

where ε_T is free, uniaxial thermal expansion,
α is the linear coefficient of thermal expansion and
ΔT is the temperature change.

In the test sample the thermal expansion is partially constrained by the uneven temperature distribution. The uniaxial constrained thermal expansion is given by the difference between measured and calculated (from Equation A2.1) thermal expansion:

$$\varepsilon_\sigma = \varepsilon_m - \varepsilon_T, \tag{A2.2}$$

where ε_T is calculated thermal expansion,
ε_m is measured expansion and
ε_σ is the constrained thermal expansion.

Due to the Poisson effect an applied strain causes a corresponding strain in perpendicular direction:

$$\varepsilon_y = -\nu\varepsilon_x \tag{A2.3}$$

where ε_y and ε_x are strains in perpendicular directions and
ν is the Poisson's ratio.

Because the thermal expansion in the test specimen is constrained in the axial and tangential directions, Equation A2.2 must be corrected to take into account the Poisson effect:

$$\varepsilon_{\sigma a} - \nu\varepsilon_{\sigma t} = \varepsilon_m - \varepsilon_T \tag{A2.4}$$

where $\varepsilon_{\sigma a}$ is the constrained thermal expansion in axial direction and
$\varepsilon_{\sigma t}$ is the constrained thermal expansion in tangential direction.

On the surface, the radial stresses are zero and axial and tangential strains are equal. Hence we get Equation 41:

$$\varepsilon_\sigma = \frac{\varepsilon_m - \varepsilon_T}{(1-\nu)} \tag{A2.5}$$

APPENDIX 3. USED FE-MODELS

The test sample was modeled with an axisymmetric, infinite height model (Figure A3.1). The specimen radius was divided to 100 elements. The model height was adjusted to give rectangular elements for best accuracy.

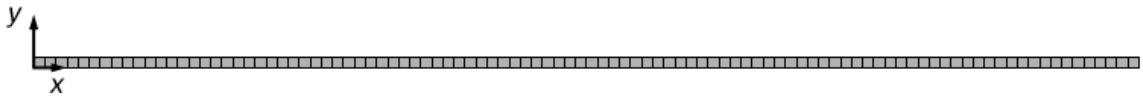

Figure A3.1. The axisymmetric element mesh used to model the test sample. The symmetry axis equals the y-axis in figure. The bottom nodes are fixed and the top nodes are forced to have an equal displacement, i.e. the model represents an object of infinite height.

In elastic-plastic modeling a multilinear isotropic-kinematic material model was used. The measured cyclic stress-stain curves (Paragraph 4.1) were inserted to the model as a temperature-dependent multilinear approximations. The material model then applied kinematic hardening rule to the material, while limiting the kinematic hardening based on the given multilinear curves to produce more stable behavior of the numerical model (Ansys Release 5.5.1, 1998).

In the contour method, the residual stresses are solved using a linear-elastic, axisymmetric FE-model describing the cut half of the specimen. The used element mesh is presented in Figure A3.2. An example of the deformed shape and the stress solution is presented in Figure A3.3.

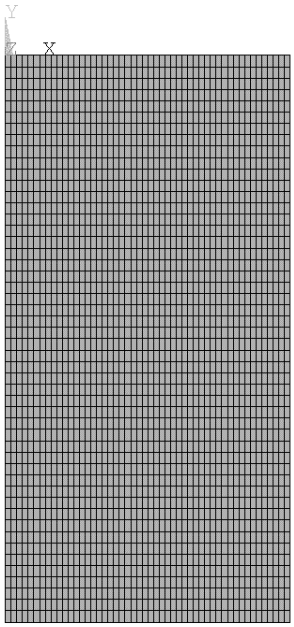

Figure A3.2. The axisymmetric element mesh used in the contour method. The symmetry axis equals the y-axis in the figure.

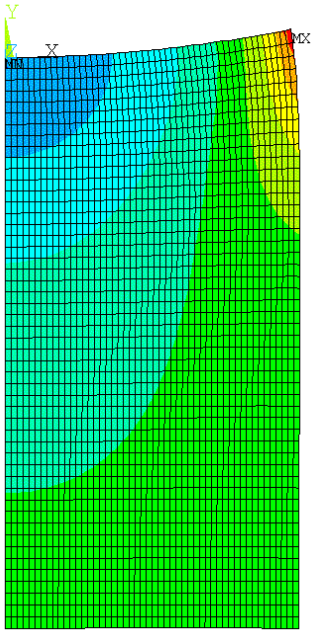

Figure A3.3. An example of the deformed shape and the stress solution for the contour method. Deformed shape is exaggerated for better illustration.

APPENDIX 4. STRESS SOLUTIONS

Δε distributions for all the used cycles were calculated with linear-elastic FE-method. The results for each material are presented in Figures A4.1 – A4.9.

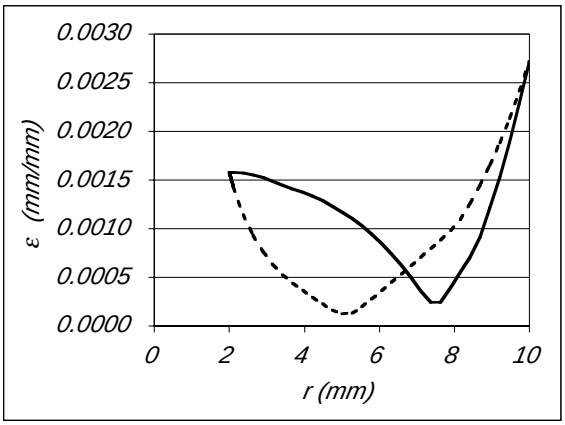

Figure A4.1. Axial (solid line) and tangential (dotted line) Δε solutions for material A (20 – 300 °C).

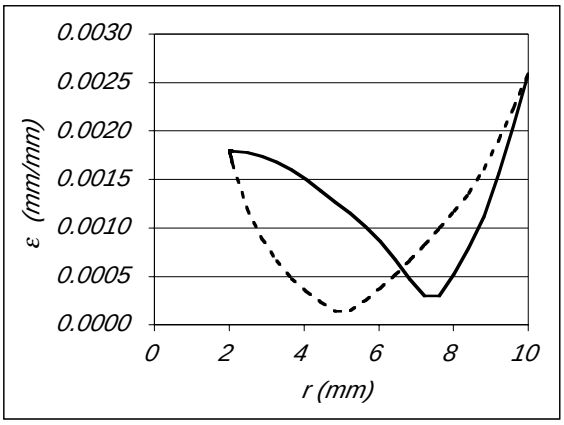

Figure A4.2. Axial (solid line) and tangential (dotted line) Δε solutions for material B (20 – 300 °C).

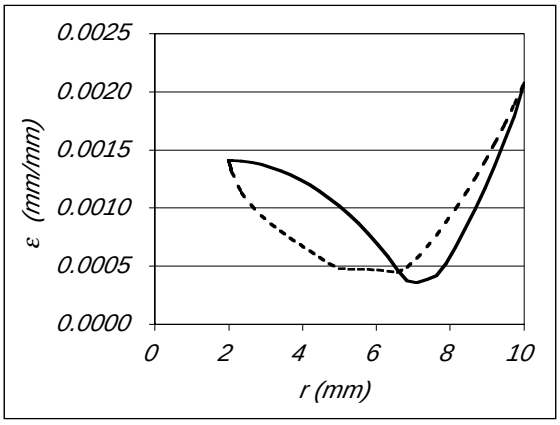

Figure A4.3. Axial (solid line) and tangential (dotted line) Δε solutions for material C (20 – 300 °C).

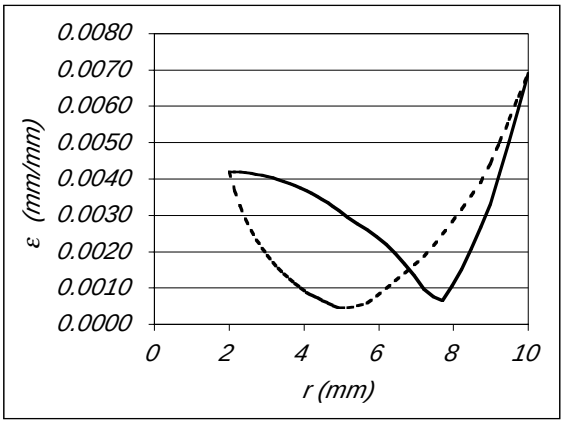

Figure A4.4. Axial (solid line) and tangential (dotted line) Δε solutions for material D (20 – 600 °C).

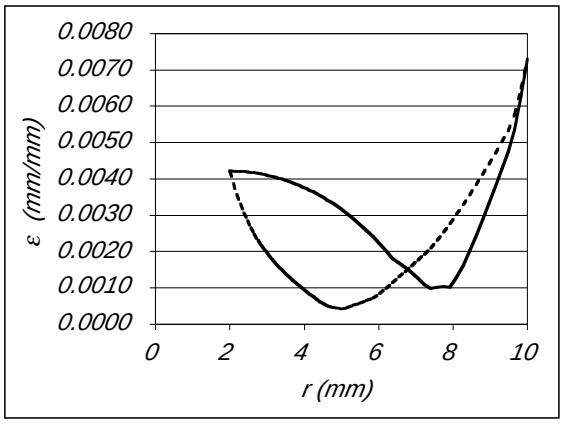

Figure A4.5. Axial (solid line) and tangential (dotted line) Δε solutions for material E (20 – 600 °C).

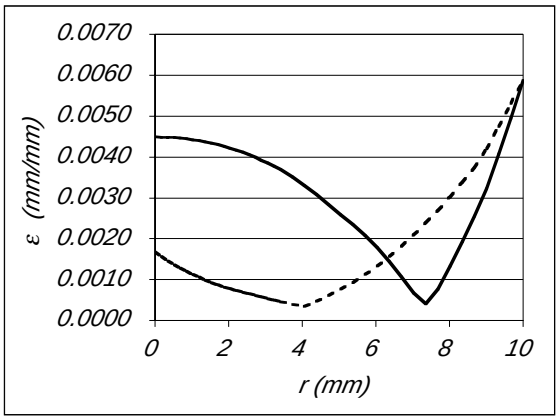

Figure A4.6. Axial (solid line) and tangential (dotted line) Δε solutions for material F (20 – 600 °C).

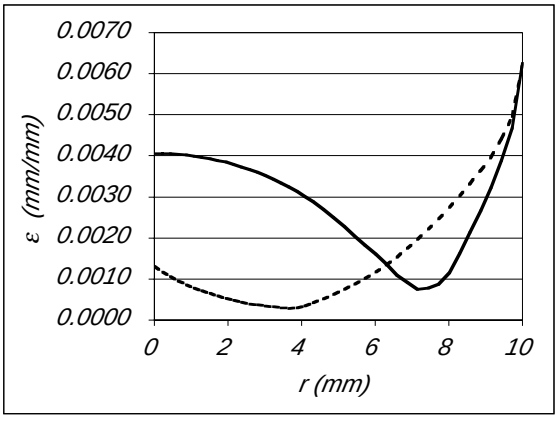

Figure A4.7. Axial (solid line) and tangential (dotted line) Δε solutions for material G (20 – 600 °C).

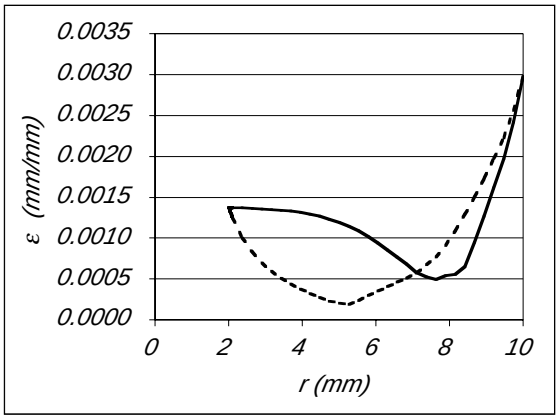

Figure A4.8. Axial (solid line) and tangential (dotted line) Δε solutions for material H (20 – 280 °C).

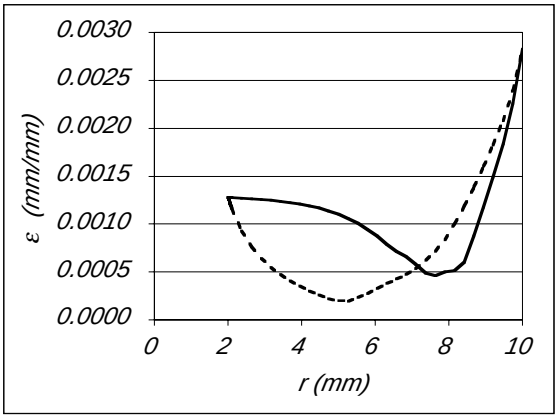

Figure A4.9. Axial (solid line) and tangential (dotted line) Δε solutions for material I (20 – 280 °C).